2020

Enabling tall towers in wind energy production

Bin Cai
Iowa State University

Enabling tall towers in wind energy production

by

Bin Cai

A dissertation submitted to the graduate faculty

in partial fulfillment of the requirements for the degree of

DOCTOR OF PHILOSOPHY

Co-Majors: Civil Engineering;
Wind Energy Science, Engineering, and Policy
(Structural Engineering)

Program of Study Committee:
Sri Sritharan, Major Professor
H. David Jeong
William Q. Meeker
J. Jay Shen
Eugene S. Takle

The student author, whose presentation of the scholarship herein was approved by the program of study committee, is solely responsible for the content of this dissertation. The Graduate College will ensure this dissertation is globally accessible and will not permit alterations after a degree is conferred.

Iowa State University

Ames, Iowa

2020

TABLE OF CONTENTS

LIST OF FIGURES

Page

LIST OF TABLES

ACKNOWLEDGMENTS

I would like to thank my major professor, Dr. Sritharan, for the opportunity to work on this research project and for the valuable guidance and advice throughout the course of this research. I am also thankful for the opportunity to work with the Siemen R&D group on wind tower simulations and want to express my gratitude to my colleagues over there for getting the chance to collaborate with them.

I am sincerely thankful to my committee members for their interests and valuable comments related to my work, especially Dr. Takle and Dr. Jeong. They both enlightened me about a variety of fascinating research in the area of wind energy.

This research would not have been possible without the financial support of the Chinese Student Council. I would also like to thank my friends and colleagues, Robert Peggar, Shibin Lin, Phil Barutha, Ali Nahvi, Doug Wood, Owen Steffens, Hartanto Wibowo, Sameer-Kumar Pachalla, Liang Zhong, Chris Levandowski, and Mengqi Wu for their support throughout my stay here and making my time at Iowa State University a wonderful experience. I am grateful to my industry partners who provided positive feedback for all the work that I carried out as part of my research at Iowa State University.

I am immensely grateful to my family, especially my grandparents, my cousins and most of all my parents who always believed in me. They were always there when I needed them and supported me throughout this journey of studying at Iowa State University.

ABSTRACT

Wind energy has already become the second highest renewable energy source that is used to supply electricity in the United States, providing 6.5% of the nation's electricity demand in 2018. With continued technology development, wind turbine towers are designed to be taller with greater wind energy resource, larger turbine blade and bigger turbine size. These efforts help increase wind energy production and reduce the cost of wind energy in the last four decades to an average Levelized Cost of Energy (LCOE) of $ 0.1-0.2 per kWh. Moreover, by increasing the tower height, wind energy production will be increased substantially which enables wind power to be more reliable and cost effective in the wind-rich areas, but also to be accessible for areas where wind resource was previously underestimated at 80 m (262 ft) and wind power was not economically developed, such as the Southeast. However, most current wind turbines built in the U.S. are at the height of 80 m (262 ft) or below, which is constrained by the transportation limits and logistic challenges. To realize the tall tower benefits for both wind-rich and lower wind-speed regions, wind observations from tall meteorological towers and measuring sensors up to 200 m were obtained and used to quantify the potential wind energy production at different sites in terms of annual energy production (AEP), a critical component in LCOE estimation. The calculation model for estimating AEP was validated with a public database and measured power production. Simulated wind data from National Renewable Energy Laboratory (NREL) were also considered in the AEP prediction for areas with limited actual measurements and evaluate the performance of the simulated dataset in wind energy assessment. With the more realistic AEP estimate, cost benefits were estimated for stakeholders if installing tall towers.

To increase the hub height of wind towers that are cost competitive over conventional tubular steel towers, Hexcrete Tower was developed to use segmental precast concrete components to assemble wind towers up to 140 m by prestressing strands. Fatigue performance of key tower components and their connections were experimentally evaluated using simulated loads to ensure the corresponding damage would be insignificant. Numerical models were created to support the design process and verified with the test results. Based on the test and finite element analyses, tower system can provide sufficient fatigue strength under the desired number of load cycles and enabling the Hexcrete tower technology to be a cost-effective alternative for tall wind power development.

CHAPTER 1. INTRODUCTION

1.1. Background

Wind energy has become an important contributor to renewable energy alternatives in supplying electricity in the United States and the world. Since 1980s, the cost of wind energy has steadily declined six fold while the capacity of typical utility-scale turbines has increased from 200 kilowatts (KW) to 2 megawatts (MW) and the corresponding average hub height has been elevated from 65 m to 88 m. With continued development in wind energy technology, the total installation of the world has expanded nearly six times to 591 gigawatts (GW) during the last decade, with the European Union consisting of 28 member countries, China, and United States leading the wind power production worldwide (Figure 1-1) (Global Wind Energy Council (GWEC), 2019). The large amount of wind generation provides electricity supply for thousands of houses in the world. In the European Union, wind energy generates nearly 362 terawatts hour (TWh), producing approximately 14% of the 2018 total electricity, while the corresponding wind power contributions are 5% and 6.5% of total power generation in China and United States, respectively (GWEC, 2019; American Wind Energy Association (AWEA), 2019). For the future wind energy outlook, the European Wind Energy Association (EWEA) predicts that meeting 24.4% of the electricity demand by wind by 2030 is the most-likely scenario (EWEA, 2015). Similar to the European wind energy perspective, the latest wind vision report released by the U.S. Department of Energy (DOE) has analyzed the potential of wind expansion nationwide and forecast that the U.S. wind energy deployment could reach 20% wind electricity by 2030 and 35% by 2050 (DOE, 2015).

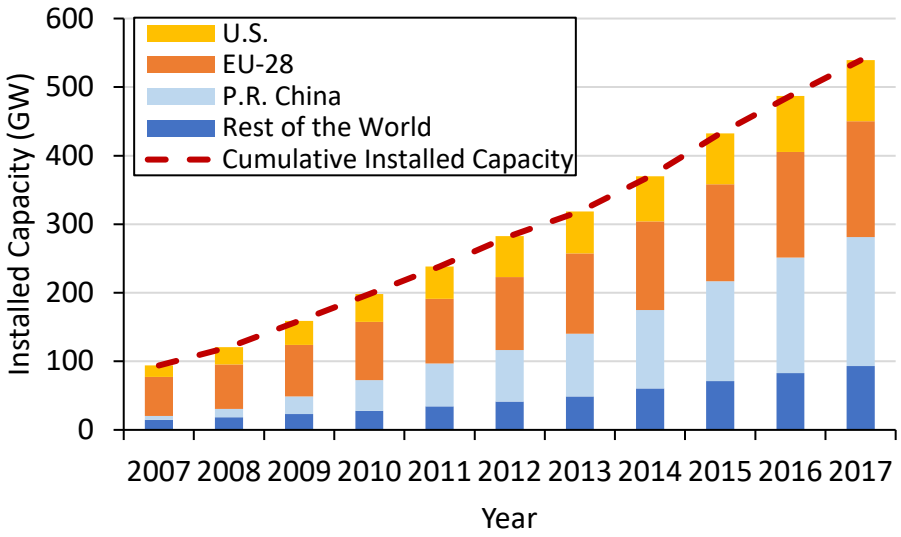

Figure 1-1. Top cumulative installed capacities across the world

As the technologies being advanced, the turbine capacity, rotor diameter, and hub height have been increased over time. According to the latest U.S. wind technology market report, the average capacity of the newly installed turbines reached 2.32 MW in 2017, exceeding more than 42% since 2007 (Wiser & Mark, 2018). Turbine sizes between 2.0 and 2.5 MW make up 75% of the total operating turbines in the U.S. market. The positive trend of average rotor diameters was also observed in the U.S., and its average value for wind turbines installed in 2017 was 113 m, a 41% growth since 2007 (Wiser & Mark, 2018). Benefitting from the larger rotor diameter, wind turbines are designed with greater swept area, which helps extract more wind power as the energy production increases by a factor of four if the blade length is doubled in size. Although most turbine manufacturers will provide a range of hub height for a given turbine model to suit for different site conditions, the average hub height increases proportionally to the rotor diameter. The average hub height of the nation's newly installed turbines in 2017 was 86 m, and approximately 76 percent of all turbines in the U.S. was installed at hub heights at least 80 m (≈ 262 ft). As seen in Figure

1-2, the central belt of the nation experiences an annual average wind speed of over 7 m/s at the height of 80 m. The emergence of 100-plus m towers was seen in 2007, and tall towers have been growing in the market since 2011. Towers of 90 m and taller represented over 37% of the total wind tower installations in 2017 (Wiser & Mark, 2018). Increases in turbine capacity, rotor diameter, and hub height are the important factors to access higher and steadier wind speed, thus enhancing the wind energy production and increasing the capacity factor for a wind farm, which measures how much energy is produced by turbines annually compared with its maximum output as a percentage.

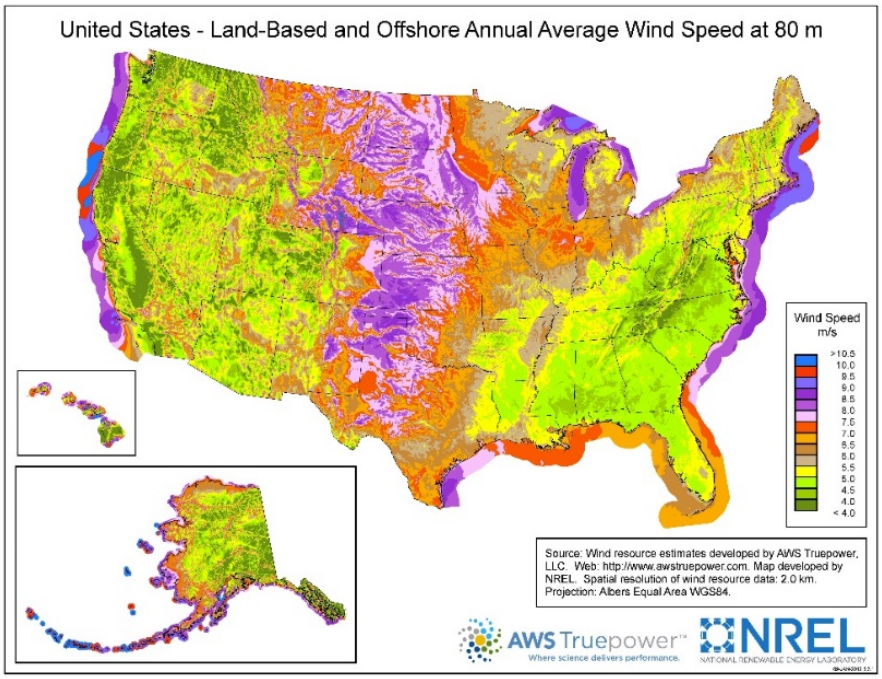

Figure 1-2. Annual average wind speed at 80 m above the surface in the U.S.

1.1.1. Current Wind Tower Technology

A majority of the utility-scale turbines built in the current US wind industry have used tubular steel towers, reaching a hub height of 80 m as shown in Figure 1-3. This tubular steel tower consists of three tower cells connected with transverse either welding or bolting

that is done in the field. Each tower cell is 20 – 30 m long and assembled from several shorter tubular steel segments. These tower segments are rolled from flat steel plates in the factory, stacked together by either welding or bolting, and transported as one of the tower cells with a maximum base diameter of 4.1 m, which is the vertical clearance limit permitted for most highway roads in the United States. Since each tower cell is manufactured by rolling steel plates and machine-welded into a tapered circular shape at the factory, quality of the welded connections is of importance to maintain the tower's long-term capacity. Longitudinal and transverse steel welds are expensive and require special attention to meet quality control requirements. Recent survey and site inspection for wind towers reported that local buckling failures due to insufficient shell design, fatigue cracks on welds and fracture of bolts connecting the tower base to the foundation, are the main causes of tower structure failure (Engström et al., 2010). Fatigue check of a steel tower shows that shell thickness of the tower section determines the fatigue life of a steel wind tower. Since welded connections are vulnerable to fatigue cracking, special attention needs to be drawn for the design and construction of the towers joints. A tubular steel tower is often designed for 20 years and assumed to be replaced at 25 years, a careful fatigue analysis on the tower connections is required to prolong its design life span (DOE, 2015).

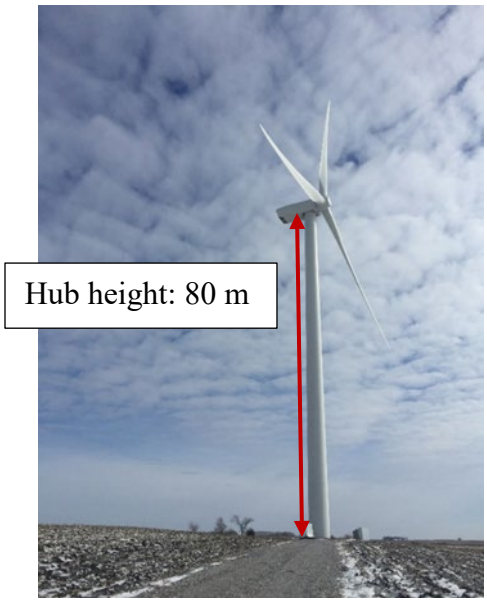

Figure 1-3. Conventional wind turbine towers with an 80 m (263 ft) hub height for turbines rated at 1~3 MW

Beside the design process, special transportation requirements and the resulting excessive construction expense increase the cost of the tubular steeltowers. Mobile cranes are commonly used for assembling wind turbines, which may be crawler cranes or the type of truck-mounted. Construction of wind farms demands large-capacity cranes, such as crawler cranes, to provide high lifting operation and small installation time. One challenge of using crawler cranes is that the transportation of these cranes may require wide access roads between turbine sites. For example, the Liebherr LR 1400 that is often used for erecting 80 m towers, which needs a 9-m (29.5 ft) wide road—this may need to be even wider for larger cranes (Engstrὂm et al., 2010). Wind speed creates restrictions on the use of this type of cranes. For examples, the maximum wind speed for lifting operation for larger crawler cranes is limited to 5 – 8 m/s, which is comparable to the annual average wind speed in the Midwest (Kelley et al., 2004; Engstrὂm et al., 2010). Furthermore, bigger cranes that are utilized to install tall towers are expensive to transport because of their oversized and large number of components. These components may require specialized trailers and special traffic permits to

pass highway routes in some states, but can also cause permit problems if the project field is in a rural area with small access roads. In this case, renting large installation equipment such as crawler cranes needs well-designed transportation logistics to minimize the construction costs, since the rental costs for cranes are typically high and large crawler cranes may not be readily available. However, excessive cost of setting up and dismantling heavy lifting cranes as well as their heavy weight narrow down steel towers for wide usage.

A conventional steel tower at 80 m can weigh more than 225 tons, which requires a large amount of rolled steel for fabrication (DOE, 2002). However, steel material for constructing wind towers is largely dependent on the market supply outside of the country, resulting in extra shipping expense and causing variations in the steel price and consequently the cost of the entire tower. For a land-based wind power plant, the overall cost of a utility-scale wind turbine supported by a conventional steel tower of 80 m is estimated at nearly $66/MWh under the assumptions in the National Renewable Energy Laboratory (NREL) cost review, and the tower cost contributes more than 15 percent of the total turbine system cost. (Moné et al., 2015).

To expand the wind energy deployment in the United States, it becomes difficult for the current wind tower design with a hub height of 80 m to enter the regions which were considered to have the least wind resource at this height in the nation. This is because steel fatigue issues, transportation challenges and high reliance on steel imports associated with the conventional wind tower design can lead to dramatic increase in cost and consequently constrain wind turbines' ability to harvest wind power more profitably in these areas. Overcoming these challenges calls for technological advancement in the wind tower design.

1.1.2. Tall Towers

Motivation for Tall Towers

The total U.S. wind capacity has been steadily growing during the past decade and reached 96 GW in 2018. However, currently only 6.5% of the total electricity generation is provided from wind generation because powering from wind is largely restricted wind rich regions only. In low-wind speed regions, wind power generation is costly because of the current technologies and associated low capacity factors. To boost capacity factors in these regions, advancing tall tower technology and thereby increasing the hub height would be two critical steps to assist with increasing wind power producing in broader regions. The tall towers would also benefit the wind rich regions. More details about the benefits of using tall towers are described below.

Tall towers help wind turbines access faster and steadier wind resource. Compared to the wind condition at 80 m shown in Figure 1-2, the map of annual wind speed at 100 m in Figure 1-4 shows more land areas in the central belt of the continent with wind speeds higher than 7.5 m/s, which is commonly identified as a good wind speed to generate power. According to a technical wind resource assessment completed by the Department of Energy (DOE), the amount of the land-based wind resource potential in the US is estimated at 10,500 GW capacity at the 80 m hub height to support a gross capacity factor of at least 35 percent (Elliott, 2010). This capacity increases to 12,000 GW or about 14% if the tower heights go up to 100 m.

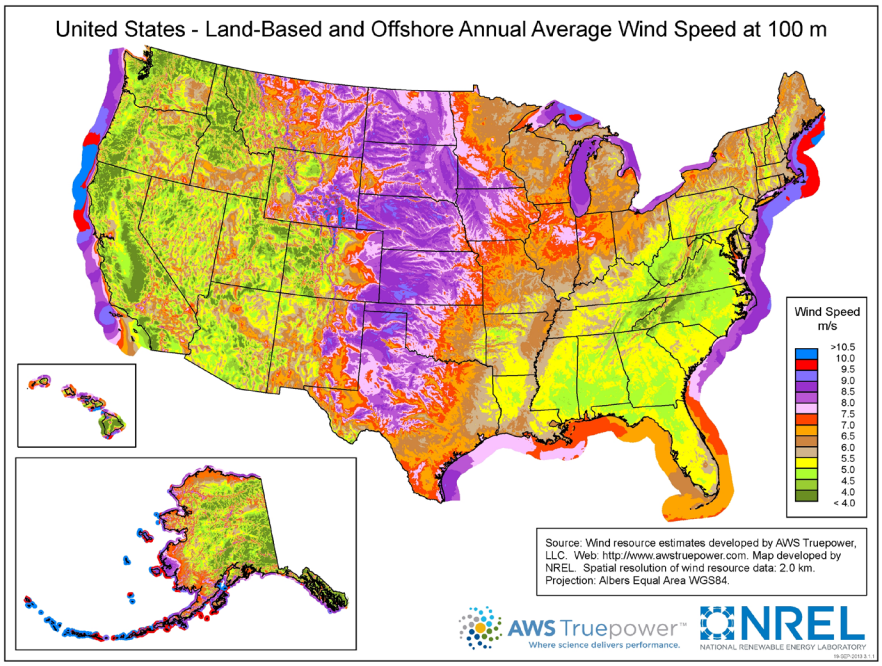

Figure 1-4. Annual average wind speed at 100 m above the surface in the US

Turbines reaching heights taller than 100 m would gain even more wind resource potential, which can be identified in the maps in Figure 1-5. This figure depicts the land areas at the chosen hub heights for wind energy potential (DOE, 2017). Dark regions in Figure 1-5 represent the states with a large amount of developable area and a high potential for wind. Compared to an 80-m (≈ 262 ft) wind turbine tower, the potential total area that sustains a gross capacity factor of 35 percent or greater increases by an additional 54 percent and 67 percent if the turbine height increases to 110 m (≈ 361 ft) and 140 m (≈ 459 ft), respectively (DOE, 2017). This suggests that installing wind turbines at higher hub heights would expand land substantially for wind power development that was previously considered not cost effective due to low wind-speed at a hub height of 80 m. These regions include Southeast and the Northeast, which have high electricity demands. Furthermore, tall towers will also improve cost effectiveness in wind-rich states, such as Iowa and Texas, which are

the current leading states for wind power generation. However, it is important to evaluate the potential use of tall towers in these states and their benefits. Since tall towers can be equipped with longer blades and larger power generators, wind turbines can produce electricity that is even more promising than realized today. Continuing to increase the efficiency of wind power will reduce the cost of energy and help achieve the goals of wind vision scenario outlined by DOE (DOE, 2015).

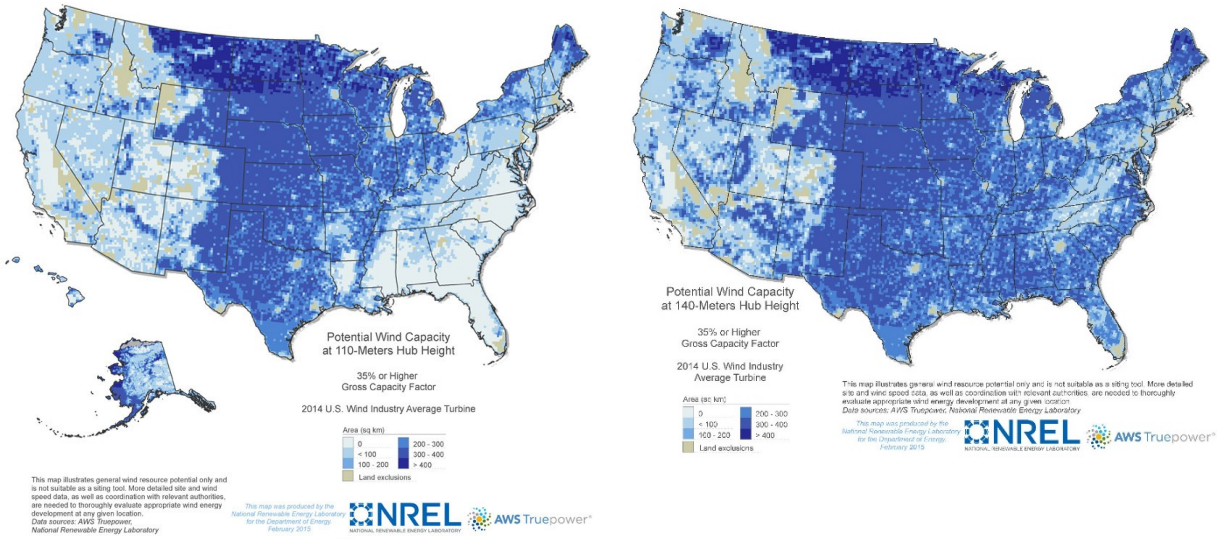

(a) Wind potential at a 110 m hub height (b) Wind potential at a 140 m hub height

Figure 1-5. Land area achieving a minimum 35% gross capacity factor based on desired tower technology at higher hub heights (DOE, 2017)

With the development of new wind tower technologies, wind turbine towers can be designed and constructed to reach hub heights of 140 m (≈ 459 ft) and higher to accommodate scaled-up turbines and longer blades, which increases the power output extracted from the wind. This increase in capacity also maximizes the efficiency of land utilization of wind farms by generating more electricity within a small footprint. Considering the typical wind speed profile, application of tall wind towers provides opportunities for turbines to access more productive wind resource at greater heights producing more wind energy than ever before, as shown in Figure 1-5. Most importantly, taller towers will

facilitate wind power production feasible in the regions where were considered to have low wind speed at the conventional height.

One criterion that is used to describe the economic value of wind power generation is the levelized cost of energy (LCOE). This measures the economics of a wind turbine or a wind power plant and serves as a criterion to compare cost effectiveness among different wind tower technologies for their design lives. The levelized cost of wind energy is typically calculated by dividing the total lifetime cost by the actual wind energy production during a single year, which is termed the Annual Energy Production (AEP). For onshore turbines, annual energy production and turbine lifetime cost are the two major contributors to LCOE reduction. By increasing the AEP, for instance through building wind turbine towers with a higher hub height, the wind turbine will generate more power with the additional advantage of reducing the LCOE, as shown in Figure 1-6 (Zayas et al., 2015). Although wind tower specialists can accurately estimate the lifetime cost of the respective towers, they will not be able to produce reliable LCOE unless AEPs are calculated accurately. This is due to not having access to reliable wind resources above 80 m and reliable model to simulate wind power at hub heights above 80 m.

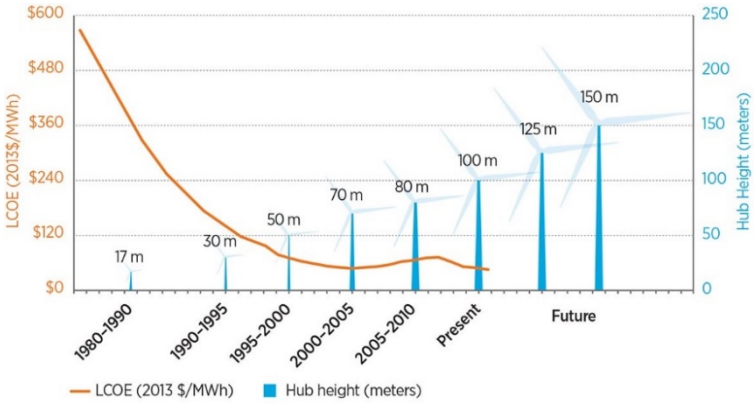

Figure 1-6. Development of the average hub height of wind turbines and its impact on the LCOE (DOE, 2015)

A cost evaluation completed by Engström et al. (2010) compares the investment of a given wind turbine per MWh among different tower technologies, which are conventional welded tubular steel towers, bolted steel shell towers, concrete circular towers with prestressing tendons, hybrid towers, lattice towers, and wooden towers. For a 3.0 MW turbine, Figure 1-7 shows a significant cost reduction per MWh/year for the considered tower designs as the hub height increases from 80 m to 150 m, but this trend does not continue above 150 m due to the availably of cranes to reach above 150 m and the associated high construction cost. Up to 100 m, the investment for different tower designs does not show wide variations, while at 125 m the welded tubular steel tower begins to reveal higher relative cost. For this reason, hybrid and bolted steel options appear to be relatively more attractive for towers above 100 m. The lattice and wooden towers have limited applications because of their numerous connections and considerable maintenance cost. The same could become an issue for bolted steel towers.

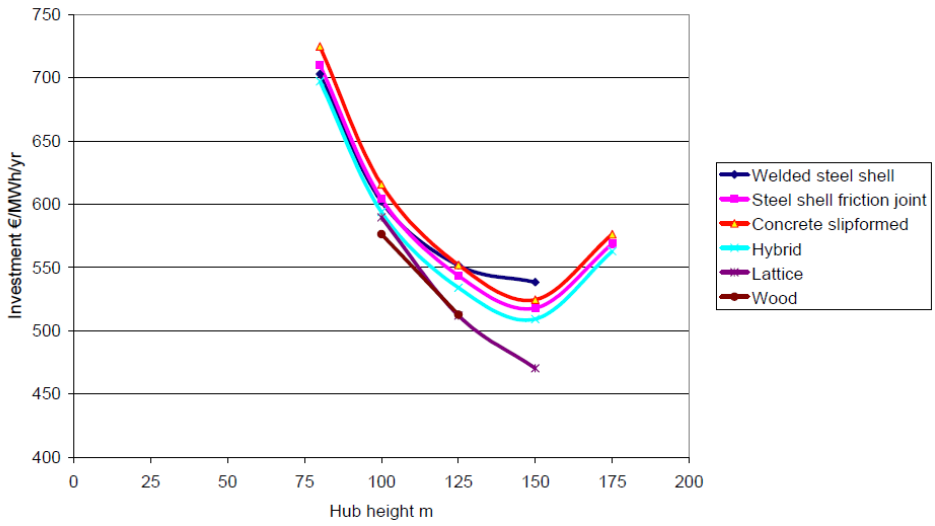

Figure 1-7. Specific costs of tower alternatives for a commissioned 3.0 MW wind turbine (Engström et al., 2010)

Challenges with Current Steel Tower Technology

Although there is an increasing motivation for installing taller wind towers, the chance of achieving the goal of 35 percent wind energy consumption by 2050 cannot be realized without addressing the two major challenges associated with designing tall steel towers. Compared to 80 m, towers with elevated hub heights would experience higher loads, which require an increase in size of tower components and overall strength to maintain stability. Heavier tower components due to the larger base diameter and thicker steel shells can cause transportation difficulties and higher cost, which makes steel towers less cost effective as the height increases.

One solution would be to design the tall towers with larger base diameters. To accommodate the increased base diameter, the desired tower foundation would require an increased size, which would also help support the increased weight and size of the tower structure. Moreover, more bolts or higher-grade bolts may be required to strengthen tower connections and transfer the larger forces from the tower to the foundation. While it is technically possible to construct tubular steel wind towers with hub heights up to 160 m at the constrained footprint of 4.3 m for transportation purposes, they will not be practicable. This is because steel towers need to be designed with thicker tower shells to overcome the increased overall forces from taller towers and larger rotors. As a result, the material and capital cost of steel towers would increase rapidly, making tall towers economically impractical to access areas including those have been offered great wind generation and those were historically thought to have limited wind potential (Zayas et al., 2015). Meanwhile, larger and heavier tower sections would need overload trucks in addition to specialized trailers for transportation, along with larger cranes and sophisticated logistics for delivering and installing wind turbine components in a limited space and time for construction. The

heaviest tower tube section can weigh over 50 tons, and highly specialized trailers could cost more than $500,000 to move each tower section, causing the transportation cost increases from $140 to $180 per mile (Cotrell et al., 2014; DOE, 2002). Larger crawler-cranes required to install the towers and turbines at 100 m height can be up to 1,000 tons, which is not commonly used in the field, thus further increasing the tower cost (DOE, 2002; Cotrell et al., 2014). For crawler cranes at and above the 650-ton class, the cost of crane mobilization and setup increases exponentially as the crane size increases, leading to a significant increase in the transportation and installation costs. The transportation logistics for delivering and assembling tower sections is the driving cost of installing taller steel towers in the United States. Extra costs resulting from the heavy special transportation and installation requirement could contribute up to 10 percent of the capital costs. The increasing cost of erecting tall steel towers makes wind energy less competitive in the energy market.

Another issue associated with taller tubular steel towers is long-term fatigue. Since the conventional tower uses bolted- or welded-connections to assemble tower segments, the longitudinal joints in each tapered tower segment and bolts between tower segments have been found to be susceptible to long-term stresses, and residual stresses in the joints could lead to fatigue cracks. The greater stresses in the joints due to the increased tower height will accelerate fatigue damage to the steel wind towers. Fatigue limit of the welding and buckling resistances of the rolled steel is the design criteria used for taller steel towers. As the tower height increases, the deflection can increase up to 2 ft at the top of the tower. To maintain and lower the drift at the top of the tower, external loads that cause the resisting and overturning moments on the tower structure need to be verified to satisfy the requirements.

Although tubular steel towers have been widely used in the U.S. wind industry, the challenges from transportation and construction constrain increasing the hub height, by which the deployment of wind energy can expand to all 50 states in the nation. Additionally, with increased hub height, wind energy can be more cost-effectively integrated into the grid in wind-rich regions because it can be produced more consistently. Therefore, persue of a new wind tower design for higher hub heights will help drive down the cost of tall wind towers and broaden the geographic area of wind energy to all the U.S. states.

1.1.3. State of the Art in Tall Tower Technology

Several tall tower technologies have been exlore worldwide and some have been used in the field especially outside of the United States. Use of these technologoies requires new manufacturing and installation techniques and can eliminate transportation challenges associated with conventional steel towers and minimize the cost for tall towers during their life-span. Steel, concrete, and hybrid tower options have been used for tall utility-scale wind farms. Descriptions of some these technologies are repesented below.

Andersen Bolted Steel Shell Tower

Steel shell tower with friction joints was proposed by Andersen to constrain the increasing base diameter for a tall tower. A joint venture was established between Andersen towers and Siemens Wind Power to install the first prototype at 90-m hub height in Hovsore, Denmark, May 2011 (Siemens AG, 2011). Another 115-m tower prototype with a capacity of 2.3 MW was installed on a test field in Lelystad, Netherland to reaffirm the possibility of building steel towers from small separated sections on site (EnecoGroup, 2012). Depending on the tower height, the bolted steel shell tower can be constructed by 9 or more segments, and each segment is made of 14-plus identical inward-facing flange shells (Siemens AG, 2011). These small identical shell elements, in large quantities, are not expensive to produce

and can be transported by standard flatbed trucks. All of the steel shell elements are connected together with tension-controlled bolts, which are designed so that re-torqueing during the designed lifespan is not required. Moreover, the bolted connection can be installed from the inside by pressing the outward-facing nut heads that are pre-assembled from the outside. The screws are mounted from the inside, holding the nuts in place. This connection solution reduces the risk of manufacture errors and long-term fatigue problem associated with welded joints in the conventional steel tower design. However, this connection method requires a well-designed hole-pattern to accommodate the steel shells so that holes can be matched perfectly and bolts are allowed to be placed in between to connect the shells.

GE Space Frame Tower

Instead of solid steel tube, General Electric introduced the Space Frame Tower design based on the concept of a truss structure and has completed its first prototype at 97-m hub height, supporting a GE 2.75 MW turbine in California (General Electric, 2015). The lattice tower is supported by five steel legs and enclosed by a PVC-polyester fabric, providing a closed tower section. All tower components are suitable for shipping by standard trucks and assembling on site. The covering fabric was tested to have high durability, extreme weather resistance and would not require replacement during its design life. These advantages therefore cut down the transportation and maintenance costs for tall towers. Furthermore, the base diameter can be less than 10 m (33 ft) for a 120 m tall tower with a 30% -50% tower weight reduction compared to the conventional steel tower design, reducing the capital cost and the overall cost of building wind farms by 3%-5% for the same size installation (DOE, 2002). However, because this tower design relies on the internal steel lattice structure, which involves numerous bolted connections, it requires extensive assembly fasteners to provide structural stability and reliability needed for its design life. The connection fasteners are not

easy to manufacture, and thereby the cost for large consumption of them can offset the transportation benefits.

Keystone Spiral Welded Tower

To eliminate bolted joints and make tall towers cost effective in the U.S., researchers recently used spiral-welded technology, a technique that has been widely applied in the pipeline industry for more than 50 years, to lower the transportation and manufacturing costs for tall steel towers (Keystone Tower Systems, 2018). Instead of stacking steel tower cells one on top of another, a series of trapezoidal steel sheets are rolled and welded simultaneously to form a conical shape by an innovative manufacture machine, which is capable of constructing large diameter towers on site. Depending on the strength capacity requirement for the tower, the thickness and dimension of trapezoidal steel sheets can be altered accordingly to match different tower diameters and tapered angles. This manufacturing technology allows tower diameters to exceed 7 m, enabling welded steel towers to reach hub heights over 140 m. The first prototype of this spiral-welded tower design was constructed by Keystone Tower System in Massachusetts, 2015. However, because edges of the trapezoidal sheets are welded together, the geometric precision of each steel sheet is very important, which requires the more proficient operation to overcome the geometric imperfection than the conventional tower design.

Freyssinet Concrete Tower with Lifting Technology - Eolift

Based on the challenges of building tall steel towers, concrete towers are beginning to be used more often for utility-scale wind turbines. Partnering with Alstom, Freyssinet offers a full concrete tower design that uses post-tensioning techniques to connect the tower from multiple precast concrete wall elements (English & Miller, 2014). Freyssinet also designed a patented lifting system, Eolift, to allow tower components, nacelle, and blades to be

assembled at the height of at least 120 m (≈ 394 ft) with less sensitivity to wind conditions as compared to existing available heavy cranes. Using this new lifting technology, a prototype of the precast concrete tower design was developed to support an Alstom ECO 122 2.7 MW turbine at a hub height of 119 m (≈ 390 ft). All concrete wall elements were constructed as curved shells, which were prefabricated in the concrete plant or on site with the use of local sources. Modular fabrication process reduces production time and on-site fabrication capability minimizes transportation costs compared with conventional steel tower technology.

Inneo Torres Concrete Tower

Spanish wind tower company Inneo Torres offers segmental concrete tower design at the hub heights between 80 m and 140 m (≈ 262 – 459 ft), which can be erected through a fast and reliable construction process to support wind turbines with a capacity from 1.5 MW to 5 MW (Jimeno, 2012). This design uses a similar concept of concrete rings connected by prestressed tendons when assembling the tower, which was developed into a hybrid tower by placing a steel tube as the final tower section on top of the concrete ring. Each precast concrete ring includes three or four curved wall elements and gradually reduces to two depending on the height. Each concrete element measures at 15 – 20 meters (≈ 49 – 66 ft) tall and 2 meters (≈ 6.6 ft) wide and can be manufactured in a mobile concrete batch plant. The mobile concrete plant can access the concrete material locally, lowering the cost variation induced from the international market and creating job opportunities for the project area. The in-situ construction technique also decreases the lead-time for assembly and the cost associated with transportation. Through the in-situ assembly of the small tower components, construction rate can reach on average 2.5 towers per week, equivalent to the existing steel

towers (Jimeno, 2012). So far, Inneo Torres has produced more than 100 full concrete towers in Spain and Latin America and is now expanding its market to North America.

Given the current available concrete tower technologies, towers are composed of curved wall elements to form a ring-shaped section. However, producing curved modules requires specific formwork that has implementation constraints: its dimension is constrained by the available technology and cost, and the time for assembling the formwork is longer than other readily-available formwork and dependent on the weather condition. These challenges will result in extensive capital cost compared to using flat concrete elements. Moreover, curved wall elements need more careful construction techniques than flat wall elements do, especially when post-tensioning tendons run radially through embedded sheathing pipes. Since these designs use regular strength concrete rather than high strength materials, the base diameter of the tower is commonly larger, causing a substantial increase in concrete volume and weight. As shown in Table 1-1, the larger tower diameters have an impact on the construction and assembly of tall concrete towers. These challenges associated with curved concrete elements discourage concrete towers from an economic point of view. Therefore, replacing the concrete shells by unique units that feature flat surface would be a good solution to minimize the manufacture challenges and mitigate cost risks.

Max Bögl Hybrid Tower System

Max Bögl leads the European market in developing wind tower technology and producing wind power. Equipped with the Alstom ECO 122 3.0 MW turbine, the first prototype of the hybrid tower system developed in 2010 included a concrete base at the lower two-thirds of the tower and a tubular steel section at the upper one third, featuring a total hub height of 139 m (≈ 456 ft) (Max Bögl Wind AG, 2014). The concrete tower base was constructed by ring-shaped precast concrete section, which was joined on top of each other

with prestressing. For manufacturing precast concrete units, high-strength concrete of compressive strength ranging from C70/85 (fc'=10.2 ksi) to C100/115 (fc'=14.5 ksi) was used to reduce the concrete volume compared with normal concrete. Additionally, the prestressing method of using external tendons to connect tower cells vertically protects the tendons from temperature-dependent corrosion and also allows to inspect these tendons from the inside of the tower, making quick on-site assembly possible. Since this connection type is "dry joint" and does not need grouting mortar after the prestressing process, it speeds up the assembly and installation process. Furthermore, because the prestressing technique has been well developed in building and bridge engineering, and no attempt of re-stressing is needed after the forces are formed in the tendons, connecting concrete wall elements with prestressing requires less maintenance work than the conventional steel tower design throughout the tower's lifespan. Once the vertical tendons have been prestressed and the concrete segment of the tower has been installed, a transition piece was placed between the steel section and the concrete base for housing prestressing anchorage and bolted connection to the upper steel section. The use of segmental precast concrete units requires no specialized trailer, making the entire transportation process easier and cheaper. The self-climbing revolving tower crane is a future direction of assembly technique to ease the installation process and reduce the cost.

MidAmerican Energy Hybrid Tower System

Although numerous tall wind towers have been developed and operated in Europe, few towers exceeding 80 m have been installed in the U.S., as shown in Table 1-1. A hybrid tower prototype owned by MidAmerican Energy started to operate in 2016 in Adams County, Iowa (MidAmerican Energy, 2016). This tower includes a 94-m (308 ft) tall concrete base and a 15-m (49 ft) tall regular steel tube. Twenty-four curved concrete segments were cast

onsite to assemble the concrete tower using 12 specialized forms provided by a local company - EFCO Corp. Contracted with MidAmerican Energy, Siemens Americas Onshore Wind had been working with Wind Tower Technology of Boulder, CO to supply and construct the patented concrete tower. All concrete tower sections had matching cast in order to provide full contact without using grout and to allow each section to match perfectly to its adjacent sections. Before installing the steel tube, a concrete ring beam of 7 m (22 ft) tall was placed as a transition piece. Once all tower segments were assembled, prestressing tendons were attached to the top and bottom of the concrete portion to provide the strength and stability of the tower. The nacelle was then installed to the top of the steel tower followed by the blades and hub erection.

While all of the tall tower concepts decribed above have been demonstrated in the field, some have been used for wind farm developement. Table 1-1 provides examples of these wind farms that have been commissioned by using different tall tower technologies.

Table 1-1. Operational wind turbine towers taller than 100 m

Owner/Developer	Concept	Hub height	Location	Base Diameter
Calandawind (Switzerland)	Tubular steel tower	119 m (390 ft)	Rhine Valley, Switzerland	4 m (13.1 ft)
Repower SE (Germany)	Tubular steel tower	120 m (394 ft)	Brunsbüttel, Germany	6 m (19.7 ft)
GoldWind (USA)	Tubular steel tower	130 m (427 ft)	Texas, USA	Foundation diameter of 22.1 m (72.5 ft)
Acciona Windpower (Spain)	Precast concrete tower	120 m (394 ft)	Vila Pará, Brazil	> 6.8 m (22.3 ft)
Freyssinet (France)	Precast concrete tower	119 m (390 ft)	Ceará, Brazil	7.2 m (23.6 ft)
Group Inneo Torres (Spain)	Precast concrete tower	100 m (359 ft)	Peña Blanca, Spain	Shell width of 2 m (6.6 ft)

Table 1-1. (continued)

Owner/Developer	Concept	Hub height	Location	Base Diameter
Advanced Tower System & JUWI (Netherlands)	Hybrid tower with 74 m (243 ft) tall concrete base	133 m (436 ft)	Grevenbroich wind test field, Germany	8.2 m x 8.2m (26.9 ft x 26.9 ft)
Max Bögl Wind AG (Germany)	Hybrid tower with 100 m (359 ft) tall concrete base	164 m (538 ft)	Hausbay, Rhineland-Palatinate, Germany	Constant shell thickness of 0.3 m (11.8 in)
MidAmerican (USA)	Hybrid tower with 94m (308 ft) tall concrete base	115 m (377 ft)	Adams County, USA	7 m (23 ft)

1.2. Introduction of Hexcrete Tower

To eliminate the constraints from curved concrete elements, researchers began to design tower components with a flat surface to replace concrete shells, which could contribute to easier fabrication, assembly and reduction labor costs. The Hexcrete tower was designed to reform the current tower technology to support utility-scale wind turbines for hub heights of at least 100 m (328 ft). To overcome the manufacturing and transportation challenges of curved concrete shells, this design utilizes hexogonal columns with flat surfaces and panels to ensure full contact between adjacent tower components. These prefabricated modular segments have been specially designed based on operational and extreme load conditions (Lewin, 2010). A full concrete tower using the Hexcrete tower technology consists of more than 12 tower sections, and each tower section is comprised of six identical concrete columns and six straight panels with heights up to 16 m (52.5 ft), as shown in Figure 1-8 (Sritharan, 2015a, 2015b).

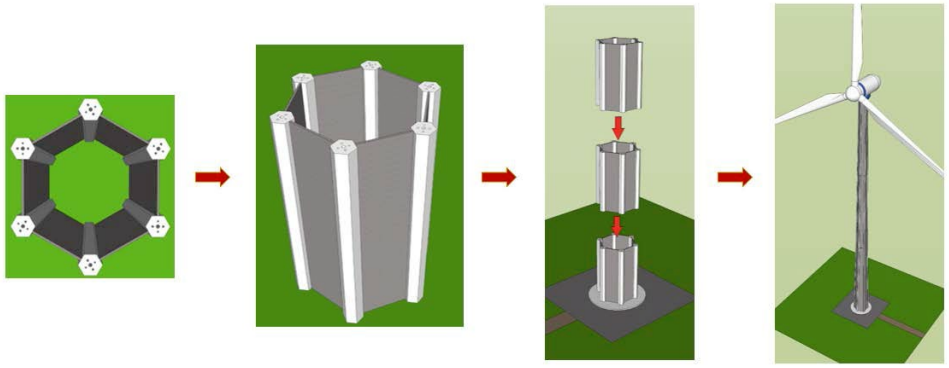

Figure 1-8. Hexcrete tower technology

In this concept, the cross-section of the tower is hexagonal, and so are the concrete columns thus lending its name to 'Hexcrete.' All panels in the tower section are designed to be rectangular or tapered wall elements, which are inserted between columns to form a six-sided tower section. Post-tensioning strands are applied through all six columns and panels in the radial direction to form a closed cross-section of the tower. The tower base section can be built directly on the foundation to eliminate the mobilization costs for the base section. The upper sections can be assembled on the ground first and stacked on the top of each other with vertical post-tensioning strands through columns, stressing from the foundation to the top of the tower. Columns at the base section are post-tensioned to the foundation which can be similarly designed as a shallow foundation for conventional steel towers. In this design, columns are the major tower components that resist loads from the wind and turbine rotor, while panels, which are not connected in the vertical direction, serve as the bracing elements to transfer the forces between columns. Unlike current concrete shell towers whose base diameters are at least 50% larger than steel towers, the base diameter of the Hexcrete tower can be controlled by using high-strength (HSC) concrete, ultra-high performance concrete (UHPC), and post-tensioning tendons.

All columns and panels in the tower use either HSC, UHPC, or a combination of these two concrete materials. The selection of concrete materials depends on the load and cost requirements for the desired tower as well as the dissemble considerations. The two types of concrete have different materials properties and unit prices. HSC has a compressive strength of 13 ksi (90 MPa), while the compressive strength of UHPC is 26 ksi (180 MPa) and the unit price of both materials is higher than normal concrete. Because UHPC has higher compressive strength than HSC, tower sections using UHPC require less concrete material than HSC sections. With a more efficient usage of materials in the Hexcrete tower than the regular strength concrete tower, a significant reduction is expected in the dimension and weight for each structural component and thus the footprint and weight for the entire tower. The design of the Hexcrete tower also calls for high strength strands. Unbonded strands are post-tensioned in the transverse direction at appropriate heights and in the longitudinal direction running through all columns from the bottom to the top of the tower. During the tower assembly procedure, once the post-tensioning forces are achieved in the strands, there is no need for the strands to be stressed again to regain forces during the lifetime of the tower. The connection method of post-tensioned strands provides high reliability and requires low maintenance cost until the end of the designed operation year, which provides economic benefits of using the Hexcrete tower for higher hub heights.

With modular components, Hexcrete tower design can overcome transportation challenges associated with the steel tower technology, as discussed in section 1.1.2. Each tower section in the Hexcrete tower is comprised of small modular segments, which features flat surfaces and can be manufactured in a mobilized concrete plant onsite or offsite without adding extra costs compared with curved shell elements. Moreover, these small modular

components can be safely transported by standard trucks and their dimensions are under the vertical clearance permitted in the existing highway system. These benefits indicate that segmental tower sections are more efficient and cost effective than conventional steel tower cells in terms of delivering and manufacturing.

In summary, compared with tubular steel towers that dominate the current market and other available concrete tower technologies, the benefits of Hexcrete tower include: a) segmental tower sections with a flat surface that do not require specialized formwork and can be fabricated in a modular fashion in a standard concrete plant offsite or at a mobile precast plant onsite This increases the pace of the fabrication process and also reduces cost for concrete formwork and therefore the manufacturing cost; b) segmental tower sections can be transported by standard loading trucks via the highway system in the United States, which does not require extra transportation cost; c) using HSC and UHPC to produce tower components provides high strength capacity and durability to the structure which leads to savings in the concrete volume and weight as well as the Operation & Maintenance (O&M) cost during the design life of the towers, although the unit price of these two materials is higher than the regular strength concrete; and d) applying unbonded multi-strand post-tensioning system to the tower connections enhances the constructability for taller tower sections. Therefore, less labor and time are required during the O&M period, which also reduces downtime on turbines and leads to cost savings throughout the life span of the towers.

To quantify the economic benefits of Hexcrete towers for elevated heights, an accurate prediction of wind energy production at elevated hub heights is needed and reliable wind resource information is an important input for estimating wind energy production. This

research relies on actual wind measurements from Iowa and Minnesota to calculate the energy production potentials at higher elevations, providing insights on the influence that energy production has on the cost estimate. Moreover, to make the Hexcrete tower a feasible structural design at greater heights, a more detailed analysis of the long-term performance on tower connections is necessary to investigate the durability of the tower technology. This research focuses on the fatigue behavior of tower connections under different loading amplitudes, which includes analyses on a large-scale experiment and numerical modeling. Further information for these researches is detailed in the following section.

1.3. Research Scope and Objectives

Although tall tower technologies are becoming available today, using of these technologies in developing wind farms is still limited, especially in the United States. One of the roadblocks in preventing implementation of these technologies is the inability to predict AEP accurately at elevated hub heights due to the lack of reliable wind resource information and reliable predictive models for estimating wind power. Therefore, establishing suitable business cases for the use of tall towers becomes a challenge. To overcome this challenge and implement tall tower technologies broadly into all 50 states in the nation, one objective of this study is to realize the benefits of tall towers in energy production by using extensive wind resource information at elevated hub heights. This will help estimate the overall LCOE and produce a feasible and accurate business model for wind project using tall tower technology such as Hexcrete tower. In addition, there is not much information available in terms of ensuring satisfactory fatigue design of tall wind turbine towers. Specific to Hexcrete tower that utilize UHPC, the available fatigue information is either generic or developed for the use of bridge design, whose fatigue cycles are expected in the range of 1 million (Aaleti et al., 2011). In order to validate the fatigue resistance of the connection method and tower

system of Hexcrete tower design, the other objective of this study is to evaluate the fatigue behavior of Hexcrete tower connections and tower system. More details of these objectives are presented below.

1.3.1. Wind Energy Potentials at Greater Hub Heights

Since the Hexcrete tower can stand up to 140 m to access better wind resource and has a potential to prolong the design life and reduce LCOE, a cost estimate for this innovative tower technology cannot be completed without a detailed analysis in quantifying the relationship between the wind energy potentials and the increased hub heights. This is because the increased energy production is likely to offset the cost increment for tall tower installations. To predict the wind energy potentials at greater hub heights, a common practice is to analyze the wind resource data from numerical weather forecasting models or measured wind data using instruments mounted to meteorological towers, SODAR or other means. However, assumptions in the numerical analysis have not been fully verified with the actual wind measurements, and extrapolation estimates would be applied to the data from short towers that may not be reliable. This is because the decreasing influence of surface roughness on wind shear and the increasing influence of lower atmospheric features, such as low-level jets and thermal circulations, makes simple extrapolation prone to large errors.

This objective focuses on realistically evaluating the wind energy potentials at elevated hub heights and providing quantification analysis on the annual energy production and capacity factor for wind farms from different locations. To achieve this, wind datasets are used in the research, including actual wind measurements from multiple locations and published wind data modeled by the weather forecasting system from NREL, to investigate the seasonal and diurnal variations of the energy production at desired hub heights. This involves tasks that are described as follows.

1. Develop a reliable model to calculate the AEP at different hub heights with reasonable assumptions;
2. Improve the accuracy of assessing the increased wind energy potentials at greater heights by using reliable wind resource information and applying the revised AEP model;
3. Investigate the influence of the increased energy production on the cost estimate of tall tower technology;
4. Determine parameters for a sensitivity analysis on estimating the energy production; and
5. Investigate the influence of wind characteristics and measuring techniques on the prediction of wind energy production at elevated hub heights.

1.3.2. Fatigue Performance of Hexcrete Tower Connections and Tower System

Although the connection methods have been considered applicable to the Hexcrete tower design, the fatigue resistances of the connections and tower system have only been subjected to limited testing. This is inadequate to represent the actual load condition and resulting responses may not accurately produce the fatigue resistance of the tower system. Therefore, a comprehensive analysis is needed on the tower connections and system focusing on the evaluation of long-term performance. This objective involves tasks that are described as follows.

1. Obtain accurate real-time strain and displacement measurements on the tower connections throughout the entire fatigue test, which undergoes 2.2 million load cycles;
2. Test the isolated column-panel-column system to ensure it meets the demands associated with the operation and extreme loads from the wind turbine;

3. Evaluate the long-term performance of the connections in the Hexcrete Tower technology under operational and extreme load conditions which are determined from the tower design; and
4. Compare the analysis results from the finite element model with the test measurements, and assess the fatigue resistance of the tower system and connections in this new tower design based on theoretical assumptions and experimental analysis.

1.4. Dissertation Layout

This dissertation is comprised of six chapters that focus on tall wind towers with an emphasis on the Hexcrete technology and wind power production at elevated hub heights. The research outcomes will be presented in the form of technical papers for submission to peer-reviewed journals in the field of wind energy development and structural engineering. Following the introduction and background information of wind turbine tower, the second chapter summaries studies and results related to the material properties and fatigue behavior evaluation of concerned concrete types. The third chapter provides an estimate model to predict wind energy production based on real-time wind climate measurements at heights greater than 80 m. The estimate model is validated by publicly available energy production data from wind market reports and then used to evaluate the wind power potential attributed to the installation of tall towers. Chapter 4 reaffirms the capability of using the calculation model for AEP in estimating wind energy production at chosen heights. This is done by examining the estimated results, which are based on the AEP calculation model and wind measurements from a tall meteorological tower, with the measured power output from a nearby wind turbine. To improve the understanding of wind power potential in the wind-rich regions, this chapter also utilizes simulated wind data up to 200 m for regions where no actual measurements are currently available. Chapter 5 quantifies the AEP growth with

increased tower heights in the U.S. southeastern regions, which were historically considered to be the least wind resource areas at the height of 80 m. Cost analysis for investing in tall towers in this region shows a clear financial increase for stakeholders if the tower height increases from 80 m to 120 m. The trend in AEP and cost obtained from the wind-rich regions and the Southeast provides an insight to find the optimal height for building tall towers at a different location. To assist with the application of the Hexcrete Tower technology, Chapter 6 investigates the fatigue performance of a representative test unit of the Hexcrete tower under cyclic loads. The test unit was designed to include three different connection types, which are column-to-column, column-to-panel, and column-to-foundation. By comparing the test responses with numerical results, the validated simulation model can be used to evaluate the fatigue behavior of the structural members. A summary of the research and concluding remarks are provided in the last chapter.

1.5. References

American Wind Energy Association. (2019). *U.S. Wind Industry Annual Market Report: Year Ending 2018*. American Wind Energy Association: Washington, D.C., USA.

Cotrell, J., Stehly, T., Johnson, J., Roberts, J. O., Parker, Z., Scott, G., et al. (2014). *Analysis of Transportation and Logistics Challenges Affecting the Deployment of Larger Wind Turbines : Summary of Results*. National Renewable Energy Laboratory: Golden, CO, USA. doi:NREL/TP-5000-61063

Elliott, D., Schwartz, M., Haymes, S., Heimiller, D., Scott, G., and Flowers, L. (2010). *80 and 100 meter Wind Energy Resource Potential for the United States.* NREL/PO-550-48036. National Renewable Energy Laboratory: Golden, CO, USA.

EnecoGroup. (2012). Siemens and Eneco Test Wind Turbine with High 'Construction Set' Tower. Retrieved from EnecoGroup: https://news.enecogroup.com/siemens-and-eneco-test-wind-turbine-with-high-construction-set-tower/

English, C., and Miller, S. (2014). Alstom Innovating to Improve and Expand its Onshore Wind Turbine Offering. https://www.alstom.com/press-releases-news/2014/3/alstom-innovating-to-improve-its-onshore-wind-turbine-efficiency Accessed June 21, 2018.

Engstròm, S., Lyrner, T., Hassanzadeh, M., Stalin, T., and Johansson, J. (2010). *Tall Towers for Wind Turbines, Report from Vindforsk Project V-342 Höga Torn för Vindkraftverk Elforsk Rapport* 10:48.

European Wind Energy Association (EWEA). (2015). *Wind Energy Scenarios for 2030*. European Wind Energy Association. doi:10.1017/CBO9781107415324.004

General Electric - Wind Turbine. (2015). Space Frame Tower. https://www.energy-xprt.com/products/space-frame-tower-318394

Global Wind Energy Council (GWEC). (2019). Global Wind Report in 2018. Retrieved from: https://gwec.net/wp-content/uploads/2019/04/GWEC-Global-Wind-Report-2018.pdf.

Jimeno, J. (2012, February). Concrete Towers for Multi-Megawatt Turbines. Retrieved from Wind Systems Magazine.

Kelley, N., Shirazi, M., Jager, D., Wilde, S., Patton, E.G., and Sullivan, P. (2004). *Lamar Low-Level Jet Project Interim Report.* National Renewable Energy Laboratory: Golden, CO, USA. doi:NREL/TP-500-34593

Keystone Tower Systems. (2018). Retrieved from Keystome Tower System: http://keystonetowersystems.com/.

Lewin, T. (2010). An Investigation of Design Alternatives for 328-ft (100m) Tall Wind Turbine Towers, Iowa State University. Ames, IA. 193.

Max Bögl Wind AG. (2014, February). High-Precision Precast Concrete Elements for Hybrid Wind Energy Towers. Retrieved from Concrete Plant International: www.cpi-wprldwide.com

Moné, C., Hand, M., Bolinger, M., Rand, J., Heimiller, D., and Ho, J. (2015). 2015 Cost of Wind Energy Review. NREL, no. May. doi:NREL/TP-6A20-66861

Siemens AG. (2011). An Innovative Solution for High Hub Heights: Bolted Steel Shell Tower. Retrieved from Siemens Energy: http://www.energy.siemens.com/us/pool/hq/powergeneration/renewables/wind-power/Bolted_Steel_Shell_Tower_brochure_EN.pdf

Sritharan, S. (2015a). Hexcrete Tower for Harvesting Wind Energy at Taller Hub Heights - Budget Period 2. Ames, Iowa. doi:10.2172/1361022

Sritharan, S. (2015b). Wind Turbine Towers: Precast Concrete Hexcrete May Help Increase Renewable Energy Capacity with Taller Hub Heights. *PCI Journal,* 60 (6): 33–38.

U.S. Department of Energy (DOE). (2017). WINDExchange: Wind Potential Capacity. *U.S. Department of Energy (DOE)*. https://windexchange.energy.gov/maps-data?category=potential Accessed June 21, 2018.

U.S. Department of Energy (DOE). (2002). *SBIR Advances Wind Turbine Towers Establish New Height Standard and Reduce Cost of Wind Energy Taller Tower Breakthrough for Large Wind Turbines.* DOE: Washington, D.C., USA. Retrieved from https://www1.eere.energy.gov/office_eere/pdfs/wind_tower_systems_sbir_case_study_2010.pdf

U.S. Department of Energy (DOE). (2015). *Wind Vision: A New Era for Wind Power in the United States*. DOE: Washington, D.C., USA. doi:DOE/GO-102015-4557

Wiser, R., and Bolinger, M. (2018). *2017 Wind Technologies Market Report*. Oak Ridge, TN. Retrieved from: https://www.osti.gov/scitech/

Zayas, J., Derby, M., Gilman, P., Ananthan, S., Lantz, E., Cotrell, J., et al., (2015). *Enabling Wind Power Nationwide*, no. DOE/EE-1218: 43. doi:DOE/GO-102015-4557

CHAPTER 2. LITERATURE REVIEW

This chapter summarizes the state-of-art of different types of concrete and steel in material and structural design level. It focuses on the structural behavior of high performance concrete and ultra-high performance concrete and the design recommendations for using these types of concrete in building wind towers. This chapter starts the discussion of material properties of each discussed concrete and steel type including the elastic modulus, compressive strength, tensile strength, which is followed by the stress-strain behavior of different types of concrete in compression and tension and the tensile response of steel. With the knowledge of the stress-strain response, material models suggested by different studies and codes are introduced for the design purpose. The maximum compressive and tensile strengths are then defined for concrete and steel in terms of the stress and strain limits in fatigue analysis. Finally, the design principle of concrete wind towers under repeated loads are evaluated for different design codes and specifications.

2.1. Material Models of Ultra-High Performance Concrete and High Performance Concrete

2.1.1. Material Properties

Modulus of Elasticity and Poisson's Ratio

Like conventional concrete, the elastic modulus of Ultra-High Performance Concrete (UHPC) and High Performance Concrete (HPC) is dependent on environment quality, such as the curing condition, age, and thermal environmental condition. To consider the effect of different aggregate composition and testing age, the Eurocode (The European Union Per

Regulation 305/2011, 2004) defined the elastic modulus of HPC as a function of the compressive strength of the concrete and time as in the following expression:

$$E_{cm}(t) = \left(\frac{f_{cm}(t)}{f_{cm}}\right)^{0.3} E_{cm} \quad (2\text{-}1)$$

where

E_{cm} is the modulus of elasticity determined at an age of 28 days in MPa;

f_{cm} is the mean value of compressive strength at 28 days in MPa and can be estimated from f_{ck}, the characteristic compressive strength of concrete, according to the Eurocode; and

$f_{cm}(t)$ is the compressive strength of concrete at the time of t days in MPa. This parameter accounts for the increasing trend of HPC compressive strength with time compared to the conventional concrete and can be estimated by

$$f_{cm}(t) = \beta_{cc}(t) f_{cm} \quad (2\text{-}2)$$

where

$\beta_{cc}(t) = exp\left\{s \cdot \left[1 - \left(\frac{28}{t}\right)^{0.5}\right]\right\}$, featuring the change in concrete strength under cyclic loading; and

s is the coefficient which only depends on the concrete grade and equals to 0.2 for concrete with yield strength larger than 60 MPa.

Although the above equations have been used to determine the modulus of elasticity for HPC in the Eurocode, limited discussions have been performed for UHPC until the recent Model Code was released. The new Model Code 2010 (International Federation for Structural Concrete (fib), 2013) recommended including a factor to count for the effect of

different composition, especially the type of aggregate, and the new estimation was written as in the following expression:

$$E_{ci} = E_{c0}\alpha_E \left(\frac{f_{cm}}{10}\right)^{1/3} \quad (2\text{-}3)$$

where

E_{ci} is defined as the slope of the secant of the unloading branch in the stress-strain diagram for uniaxial compression and tension. It equals to the mean value of the tangent modulus of elasticity at the age of 28 days, which is known as E_{cm};

E_{c0} equals to a constant of 21.5×10^3 MPa; and

α_E is the coefficient accounting the effect of types of aggregate on the modulus of elasticity and equals to1.0 for quartzite aggregate, 1.2 for basalt and dense limestone aggregates.

Based on its definition, E_{ci}, quantifies the mean value of the tangent modulus of elasticity in the stress-strain diagram but does not include the irreversible deformation at the beginning of the test (Figure 2-1). In order to consider the initial plastic strain, the modulus of elasticity should be modified as

$$E_c = \alpha_i E_{ci} \quad (2\text{-}4)$$

when $\alpha_i = 0.8 + 0.2\frac{f_{cm}}{88} \leq 1.0$ (Larsson, 2008). This factor counts the difference of E in the stress-strain diagram between the stress of up to $\sigma_c = -0.4f_{cm}$ and the unloading branch, as shown in the Figure 2-1.

With increased concrete strength, the loading and unloading branch become closer, and the factor α_i increases. For concrete with grades greater than C80, α_i approximately reaches 1.0 and the difference of E becomes smaller than 3% and could be neglected. Values of the tangent modulus of elasticity and the modified E can be obtained from Model Code

2010, which shows that the same E values were recommended for concrete with a grade higher than C80 (f_{cm}=80 MPa).With this conclusion, HPC and UHPC with f_{cm} higher than 90 MPa can use E_{ci} to determine the modulus of elasticity.

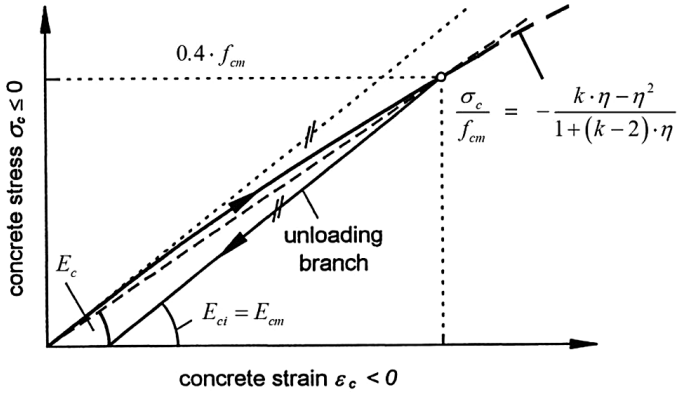

Figure 2-1. The difference of modulus of elasticity according to Model Code 2010

Apart from the Model Code studies, the French design guideline AFGC (Association Francaise de Genie Civil (AFGC), 2013) provided design recommendations for UHPC in addition to the evaluation of testing method. Likewise the definition in the previous studies, AFGC recommended using E_{cm} in the estimate of the elastic modulus and it can be calculated by

$$E_{cm} = k_0 f_{cm}^{\frac{1}{3}} \qquad (2\text{-}5)$$

where k_0 is the factor that can be determined by the mean value of the compressive strength and its corresponding strain. Note that both E_{cm} and f_{cm} are expressed in MPa.

Material properties of UHPC and HPC have not been documented in American concrete design code. However, ACI 318-14 (ACI committee 318, 2014) suggested similar expressions to characterize the properties for normal strength concrete as those in European codes and design guidelines. The modulus of elasticity was defined as the slope of the stress-

strain curve up to the stress of $0.45f_c'$ rather than $0.4f_c'$ in the Eurocode 1992. It can be calculated by

$$E_c = 57000\sqrt{f_c'(psi)} \quad (2\text{-}6)$$

To investigate the application of UHPC in bridge engineering, the Federal Highway Administration (Graybeal, 2013) have conducted numerous experiments to test the material properties of UHPC and developed design recommendations and guidelines for UHPC. The FHWA tested various UHPC cylinders with different curing methods and results showed the following relation between E_c and the compressive strength f_c' in standard steam curing treatment when f_c' is between 4.0 and 28.0 ksi (28 to 193 MPa)

$$E_c = 46200\sqrt{f_c'(psi)} \quad (2\text{-}7)$$

Comparing with other studies in estimating the modulus of elasticity, results (labeled as dash lines) obtained from the Equation (2-7) demonstrate more realistic predictions as shown in Figure 2-2.

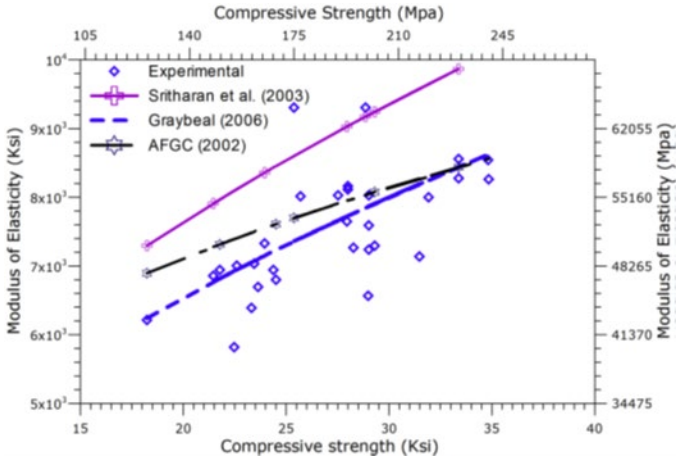

Figure 2-2. Measured and predictions of the modulus of elasticity of UHPC (Graybeal, 2013)

In the estimate of Poisson's ratio, the Eurocode and Model Code suggested a range between 0.14 and 0.26 for design with UHPC and HPC when considering the effect of crack formation. These design codes also suggested that 0.20 can be assumed as an initial value of the Poisson's ratio when the material properties are not available. Graybeal measured the Poisson's ratio of UHPC between 0.2 and 0.21 regardless of the curing method and thus 0.20 was recommended for designing with UHPC. (Graybeal, 2013)

Design Models of Stress-Strain Response in Compression and Tension

The stress-strain behavior of UHPC is important in determining the design capacity at ultimate and service load cases. Eurocode (The European Union Per Regulation 305/2011, 2004) and Model Code 2010 (fib, 2013) used the following schematic diagram (Figure 2-3) to describe the stress-strain relation of conventional concrete in compression. Model Code 2010 (fib, 2013) extended the study of concrete with a maximum grade of 90 MPa to 120 MPa. The strain value at the peak stress was suggested to be 0.003 for concrete with a compressive strength of higher than 80 MPa. The concrete stress-strain relationship can be determined by the following expression

$$\frac{\sigma_c}{f_{cm}} = \frac{k\eta - \eta^2}{1+(k-2)\eta} \qquad (2\text{-}8)$$

where

f_{cm} uses the same definition as it mentioned in the previous section;

E_{ci} is the tangent modulus of elasticity and $0.4f_{cm}$ can be used to calculate;

E_{c1} is the secant modulus of elasticity up to the maximum compressive stress f_{cm};

η is the ratio of strain at σ_c and the maximum compressive stress $f_{cm}$and equals to $\frac{\varepsilon_c}{\varepsilon_{c1}}$;

k is the plastic number and equals to $\frac{E_{ci}}{E_{c1}}$; and

ε_{c1} is the strain at the maximum compressive stress.

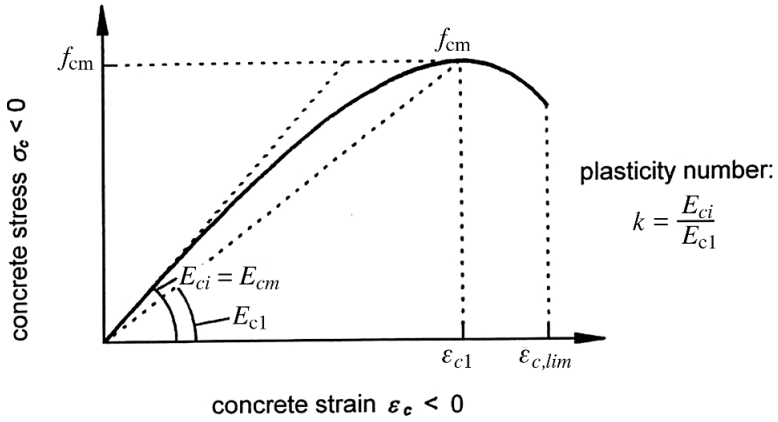

Figure 2-3. Stress-strain relation for conventional concrete under uniaxial compression

The descending part of the stress-strain curve is dependent on the material and test specimen. Considering the effect of fiber bridging on the compressive strength, the stress of UHPC may not decrease and the softening process may not occur right after the stress reaches the maximum compressive strength. Several studies attempted to measure the compressive stress of UHPC test cylinders with different configurations and considered to develop new stress-strain curves for UHPC after the stress reaches its peak value. In contrast to assuming a linear relationship between the stress and strain for the initial part of the curve, the Japanese code (Japan Society of Civil Engineers, 2008) tested numerous High Performance Fiber Reinforced Cement Composite (HPFRCC) specimens and recommended to use a defined curve to describe the initial branch (Figure 2-4). The curve expression can be defined using the following equation

$$\sigma_c' = \frac{0.85 f_{ck}'}{\gamma_c} \times \frac{\varepsilon_c'}{\varepsilon_m'} \times \left(2 - \frac{\varepsilon_c'}{\varepsilon_m'}\right) \quad (2\text{-}9)$$

where

ε_{cu}' is the ultimate compressive strain;

ε_m' is the compressive strain at the maximum stress and equals to nearly 0.004;

f'_{ck} is the characteristic compressive strength of HPFRCC in MPa; and

γ_c is the safety factor of 1.3.

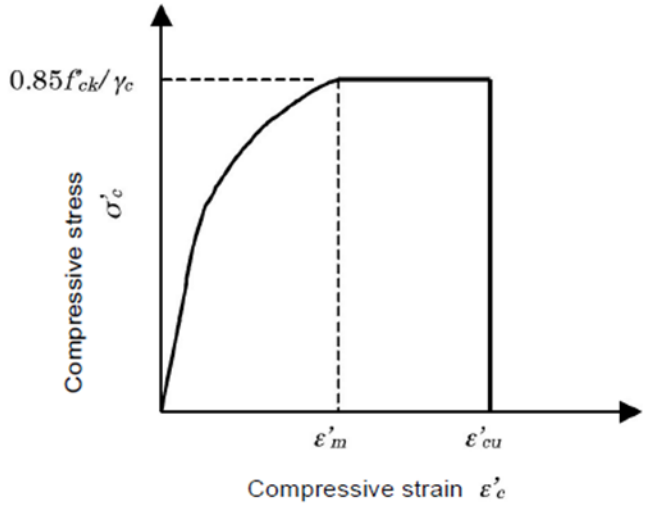

Figure 2-4. Compressive stress-strain response of HPFRCC

A comparison of the stress-strain behavior among these curves is shown in Figure 2-5. (Acker & Behloul, 2004; Graybeal, 2010; Sritharan et al., 2003) These experimental curves were found to be consistently linear up to 80 to 90 percent of the peak stress, as point A labeled in Figure 2-5. The strain corresponding to the peak stress value falls at approximately 0.0035 and 0.0041 for untreated and steam-cured specimens, respectively. Sritharan (Sritharan et al., 2003) recommended a linear elastic behavior of the compressive stress-strain response for UHPC up to the maximum stress of 24 ksi with a corresponding strain of 0.0032, as shown in Figure 2-5. (Sritharan et al., 2003) The maximum elastic strain is approximately the same as the maximum usable strain of 0.003 for designing normal concrete at extreme compression fiber. The compressive stress remains unchanged until the strain increases to 0.0042 and then reduces to zero when the strain reaches its ultimate limit of 0.007. Since the idealized stress-strain behavior in Figure 2-5b) shows a good agreement

with the experimental results in the initial linear inclination part before the peak stress, this curve and the corresponding E_c are applied in the following study.

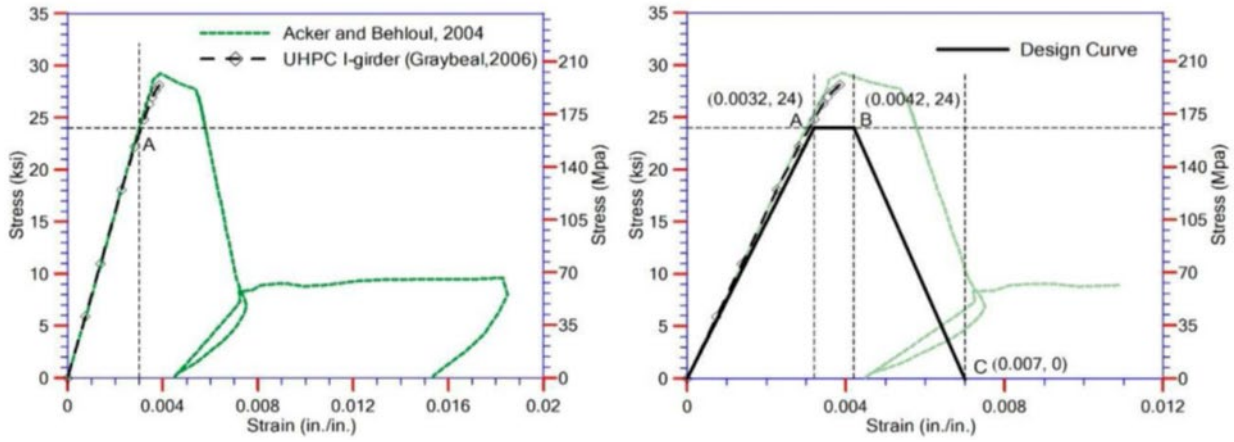

Figure 2-5. Measured (left) and design (right) stress-strain behavior of UHPC in compression

The newly published report from ACI (ACI 239R-18, 2018) overviewed and summarized the UHPC production, material properties, fundamental principles of designing with UHPC, and current UHPC applications. Because of its unique combination of material content, in contrast to conventional concrete, the tensile capacity of UHPC is also considered in the design. The stress-strain responses in compression and tension are simplified and determined by a number of parameters, as shown in Figure 2-6. The suggested compressive response by ACI 239R-18 in Figure 2-6(a) shows a similar tri-linear curve as the design stress-strain diagram suggested by the FHWA and the slope of the first linear segment of the curve defines the elastic modulus. Between the maximum elastic strain and ultimate strain, stress experiences a minimal change. Because of its cement type, UHPC can provide up to six times higher compressive strength than conventional concrete, and therefore, with the increased compressive strength, UHPC demonstrates a higher magnitude of the modulus of

elasticity, which means a steeper slope of the stress-strain curve within the elastic range. As a result, the material is more brittle than conventional concrete.

To describe the tensile response of UHPC, a direct tensile test on UHPC cylinders shows that UHPC's tensile strength should not be ignored and its tensile behavior can be characterized by three stages. The tensile behavior in Figure 2-6(b) presents a typical design curve, which assumes the strain-hardening and strain-softening stages following the initial elastic linear behavior. In contrast to Fiber Reinforced Concrete (FRC), the tensile stress of UHPC increases after the first crack and strain-hardening stage occurs. Figure 2-7 (Naaman, 2007) shows the higher tensile strength and post-cracking ductility of UHPC in comparison to conventional FRC. The first linear-elastic part in the two curves is similar until the stress reaches the cracking strength S_{cc}, but after the first crack, UHPC exhibits a higher post-cracking strength S_{pc} than the conventional FRC, presenting a strain-hardening behavior as the stress increases, as shown in Figure 2-7. At point B, the concrete stress begins to fall as the deformation increases and crack localization occurs. Similar to conventional FRC, until the specimen fails to take any load, this part of the curve shows the strain-softening behavior of UHPC. However, neither this FRC study nor the ACI report provides comprehensive design recommendations for UHPC under cyclic loads. Guidance associated with determining capacithe ty of UHPC under fatigue loads has been developed by Schmidt and Fehling (Schmidt & Fehling, 2005), the international federation of structural concrete (fib, 2010) and the Eurocode (Eurocode, 2004).

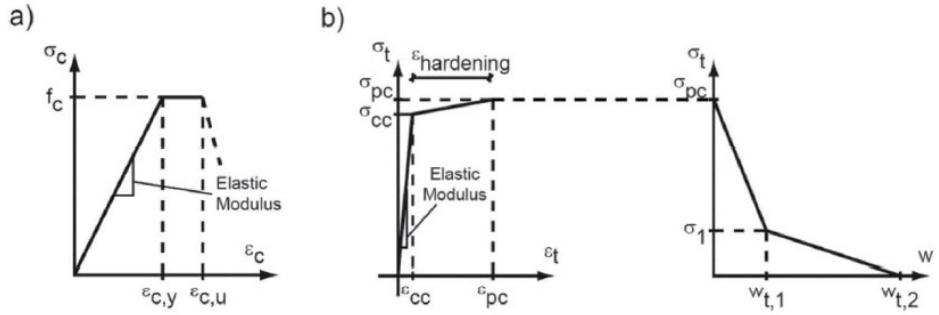

Figure 2-6. Schematic stress-strain relationship for design with UHPC in (a) compression and (b) tension (ACI 239R-18, 2018)

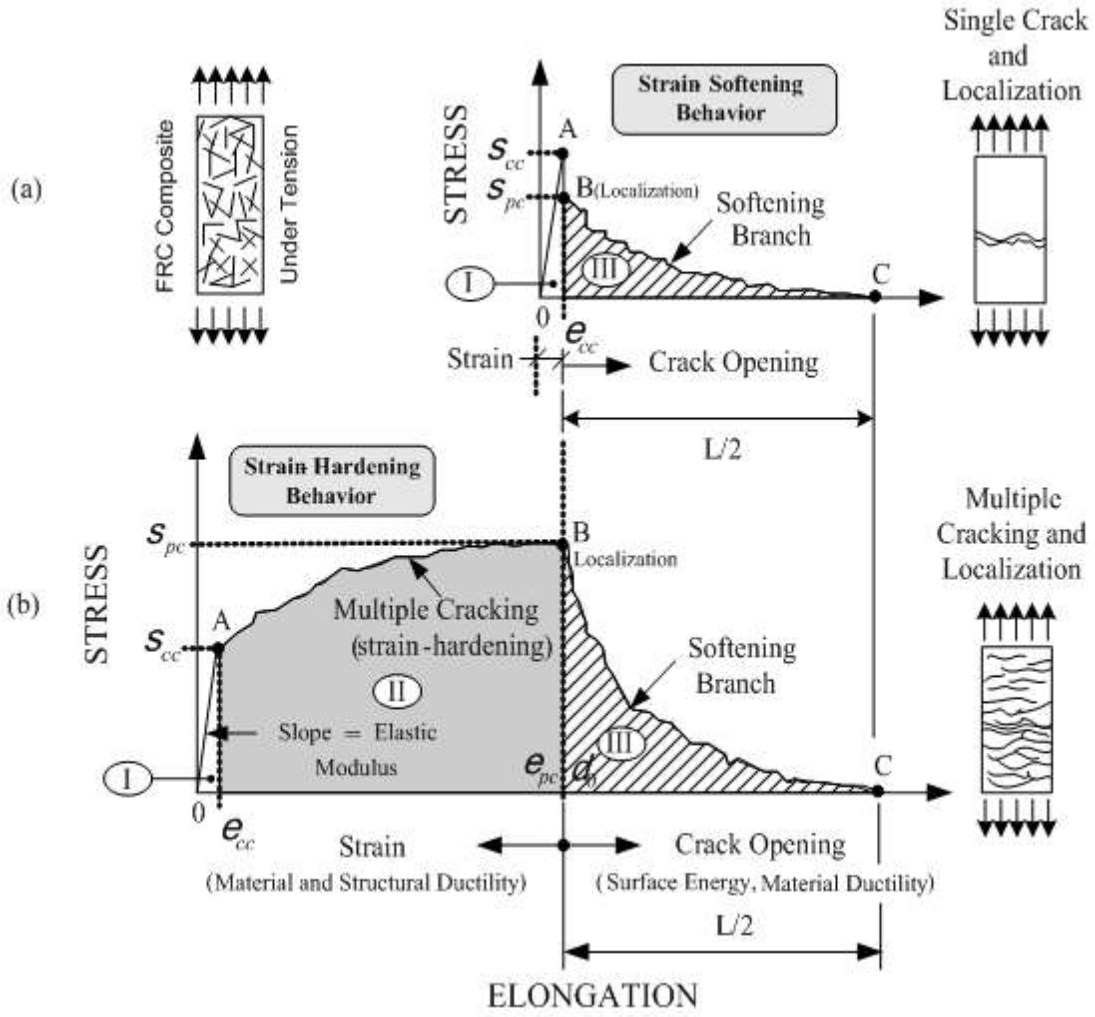

Figure 2-7. Stress-strain behavior of (a) conventional FRC and (b) UHPC in tension (Naaman, 2007)

Design Compressive and Tensile Strengths

Consistent with the Eurocode, Model Code (fib, 2013) defined the compressive strength for structure analysis and design as the following Equation (2-10). Likewise, the design tensile strength can be determined by considering the safety factor γ_c and calculated by Equation (2-11).

$$f_{cd} = \alpha_c f_{ck}/\gamma_c \quad (2\text{-}10)$$

$$f_{ctd} = \alpha_{ct} f_{ctk}/\gamma_c \quad (2\text{-}11)$$

where

f_{ck}, f_{ctk} are the characteristic compressive and tensile strength of concrete cylinders after 28 days in MPa;

γ_c is the safety factor for concrete and equals to 1.5; and

α_c, α_{ct} are assumed to be 1.0 or 0.85 if the compressive or tensile strength is determined at an age greater than 28 days.

With an increasing interest in applying fiber reinforced concrete (FRC) in structural engineering in the U.S. market, ACI committees have become realized the importance of developing guidelines for FRC structural design in the nation. ACI 544.4R-18 (ACI Committee 544, 2018), a recent ACI published report, was intended to provide technical support and guidelines for design with FRC and introduce construction practices for FRC. Contrary to the Whitney Stress Block convention used to determine the compressive stress in normal concrete, the distribution of compressive stress for FRC was assumed to be triangular with a maximum stress of f_c' rather than $0.85f_c'$ for normal concrete. This higher stress assumption considers the positive effect of the unique composition of concrete and fiber in the compressive zone. For FRC structure components subjected to pure compression, ACI

544.4R-18 suggested to use 0.002 as the compressive strain limit, which also defines the maximum compressive strain of the elastic linear part of the stress-strain behavior. For FRC components not in pure compression, a value of 0.0035 was suggested to be the maximum usable strain of FRC in compression. (Vandewalle et al., 2003)

Graybeal (2013) conducted cylinder tests on UHPC with different sizes and curing treatments. Based on a regression analysis, he recommended using the following expression to determine the increasing compressive strength with age greater than 0.9 days:

$$f'_{ct} = f'_c \left[1 - exp\left(-\left(\frac{t-0.9}{3}\right)^{0.6}\right)\right] \quad (2\text{-}12)$$

where

f'_{ct} is the UHPC compressive strength at the age of t days in ksi; and

f'_c is the UHPC characteristic compressive strength in ksi at 28 days;

The tensile strength of UHPC was found to be higher than normal concrete with the use of steel fibers and thus cannot be ignored after cracking in the design. Depending on the curing method, Graybeal (2013) reported that the tensile strength f_{ct} can be related to the compressive strength f'_c by the following equation based on regression analysis:

$$f_{ct} = 7.8\sqrt{f'_c(psi)}\ or\ 8.3\sqrt{f'_c(psi)} \quad (2\text{-}13)$$

Subsequent studies of the UHPC tensile strength found that the stress-strain behavior in tension can be assumed to be linear elastic up to the peak tensile stress with the corresponding pullout strain of 0.007. (Graybeal, 2010) These tests characterized the tensile response of UHPC to be four phases: elastic behavior (Figure 2-8(a)): inelastic cracking when multiple cracks occur individually, crack straining while individual cracks become wide, and crack localization when the fibers bridge cracks which strains exceed their limit. The design curve in Figure 2-8(b) shows consistent with the test results during the linear

elastic stage, and therefore this design curve was suggested to represent the elastic behavior response of UHPC.

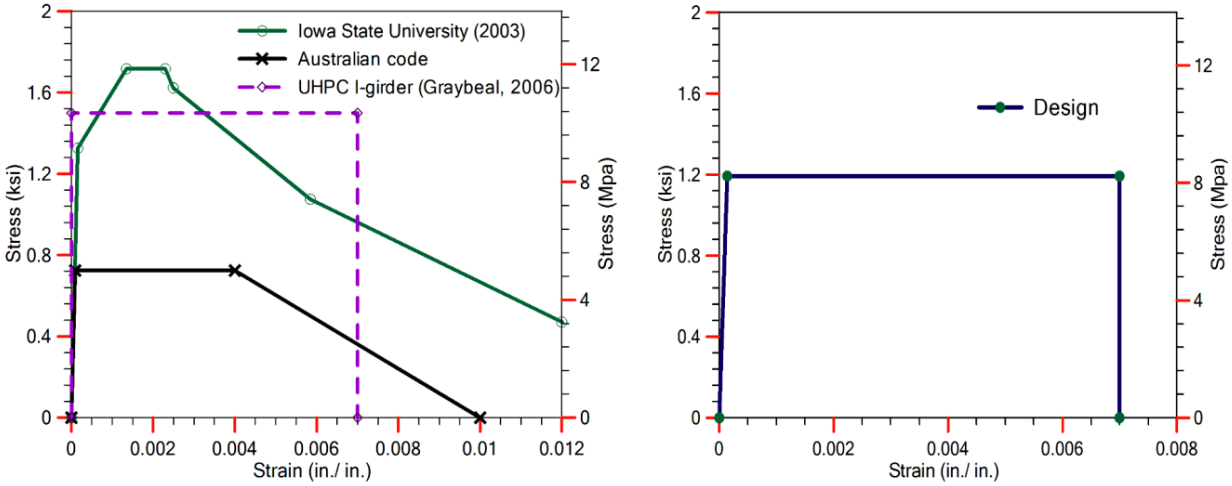

Figure 2-8. (a) Measured and (b) design stress-strain behavior of UHPC in tension

Design Fatigue Strength

In the evaluation of fatigue performance, γ_c is also written as $\gamma_{c,fat}$ and f_{cd} is replaced by $f_{cd,fat}$. According to the Eurocode (The European Union Per Regulation 305/2011, 2004), fatigue verification for concrete under compression can be assumed if the compressive stresses satisfy the following condition

$$\frac{\sigma_{c,max}}{f_{cd,fat}} \leq 0.5 + 0.45\,\frac{\sigma_{c,min}}{f_{cd,fat}} \begin{cases} \leq 0.9 \text{ for } f_{ck} \leq 50 \text{ MPa} \\ \leq 0.8 \text{ for } f_{ck} > 50 \text{ MPa} \end{cases} \quad (2\text{-}14)$$

where

$\sigma_{c,max}$ is the maximum compressive stress at a fiber under the frequent load combination;

$\sigma_{c,min}$ is the minimum compressive stress at the same fiber where $\sigma_{c,max}$ occurs;

$f_{cd,fat}$ is the design fatigue strength of concrete.

The recommended value of $f_{cd,fat}$ for the number of cycles $N \leq 10^6$ in this European code is

$$f_{cd,fat} = \beta_{cc}(t)\beta_{c,sus}(t,t_0)f_{ck}\left(1-\frac{f_{ck}}{250}\right)/\gamma_{c,fat} \quad (2\text{-}15)$$

where

$\beta_{c,sus}(t,t_0)$ is chosen to be 0.85 to account for the effects of actual frequencies of loading on the fatigue strengths since in most practical cases the loading frequencies are significantly lower than those applied in laboratory tests;

$\gamma_{c,fat}$ is the safety factor of 1.5; and

$\beta_{cc}(t), f_{ck}$ use the same definition as it mentioned in the previous section.

Given HPC has relatively small porosity, the effect of drying and water penetration on the HPC is concentrating on the HPC surface and the design formulation above can also be used for determining the fatigue strength of HPC. In the discussion of the design compressive strength of UHPC, French Standard NF P18-710 (French Standard Institute, 2016), which serves as a national addition to the European code 1992, added new design specifications for UHPC. The material characteristics of UHPC maintained the same as those of HPC recommended in the European design code in terms of the value of Young's modulus, Poisson's ratio, safety factor, and the bi-linear stress-strain relation of UHPC in compression. In the process of quantifying the compressive strength of UHPC for design under cyclic loading, and the expression is written as follows

$$\frac{\sigma_{c,max}}{f_{ck}} \leq 0.4 + 0.4\,\frac{\sigma_{c,min}}{f_{ck}} \quad (2\text{-}16)$$

where $\sigma_{c,max}$, $\sigma_{c,min}$, and f_{ck} are the same parameters as those described in the above design recommendation. This fatigue verification of UHPC under compression in the new French

Standard also relies on the maximum and minimum compressive stresses but the compressive stresses follows a more rigid condition under fatigue loads.

2.2. Material Models of Reinforcing and Prestressed Steel

2.2.1. Design Models of Stress-Strain Response

The stress-strain response of reinforcing steel in tension shown in the Eurocode (The European Union Per Regulation 305/2011, 2004) suggested a bilinear curve to characterize the relationship. Modulus of elasticity E_s of the normal reinforcing steel was defined as the slope of the curve up to the yield strength $f_{yk}$and its value was measured to be 29000 ksi (200 GPa). This value does not change in the definition of the steel modulus of elasticity in the new European and American codes (ACI committee 318, 2014; fib, 2013), and thus it will be applied to the following analysis in the dissertation. A typical stress-strain diagram for hot-rolled carbon reinforcing steel is illustrated in Figure 2-9, including an elastic stage up to the yield strength, a stress plateau with an increasing deformation until the strain hardening stage reaches, and the last stage of accumulative stress at a reducing rate until the ultimate tensile stress limit f_u and the corresponding ultimate strain ε_{uk}. For design purposes, there are two different design models used to represent the stress-strain behavior (see two B curves in Figure 2-10. One model features an idealized curve with the assumed linear strain-hardening stage with a strain limit of ε_{ud} and a maximum stress of kf_{yk}. The other curve consists of an elastic range up to the yield strength and a yield strength plateau without the strain-hardening stage. The former model assumes an inclination in stress with the strain increases, considering the influence of strain hardening in the capacity design while there is no stress plateau included. The latter model with a horizontal branch simplified the stress-strain behavior by replacing the strain hardening stage with a continuous strain growth at a

constant stress level. Therefore, this model suits for applying for analysis of steel within the elastic range.

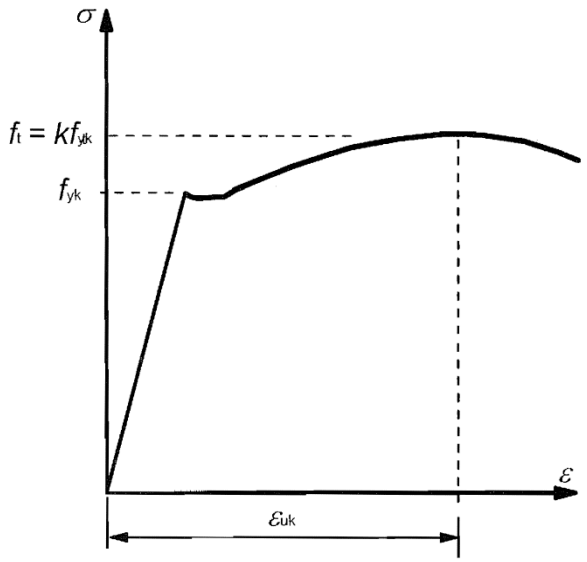

Figure 2-9. Typical stress-strain curve of hot-rolled carbon steel

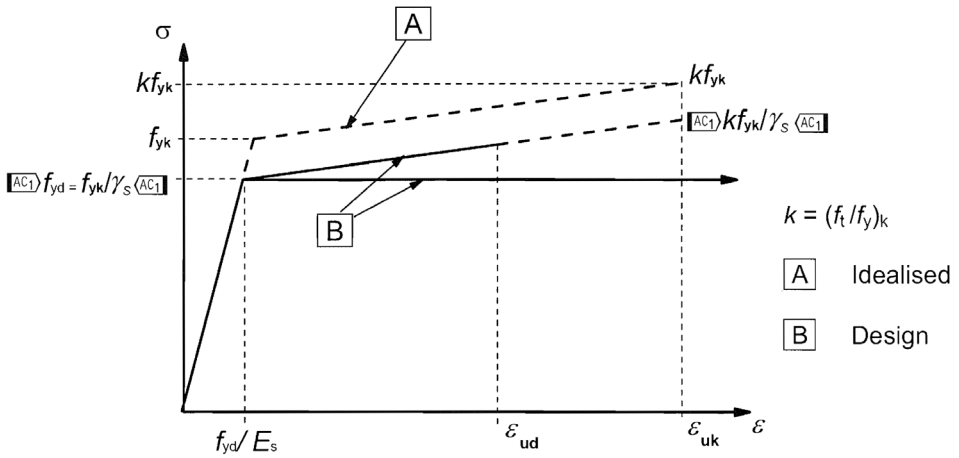

Figure 2-10. Comparison of idealized and design stress-strain behavior of conventional reinforcing steel in Eurocode 1992 (The European Union Per Regulation 305/2011, 2004)

When defining the stress-strain behavior of prestressing steel under normal thermal conditions, the stress-strain curve was also assumed bilinear in Eurocode 1992, as curve A demonstrated in Figure 2-11. (The European Union Per Regulation 305/2011, 2004) This

curve can be determined by the 0.1% proof stress $f_{p0.1k}$, modulus of elasticity E_p, ultimate tensile stress f_{pk}, and the corresponding strain ε_{uk}. The value of the modulus of elasticity varies between 28282 and 30458 ksi (195 to 210 GPa), depending on the material. E_p can be taken as 28282 ksi for strands and 29732 ksi for wires.

For design purposes, γ_s was introduced to be the safety factor and the value equals to 1.15 in fatigue verification. Two similar models, labeled as B in Figure 2-11, were suggested for prestressing steel as those used for designing with reinforcing steel. Model with a strain limit ε_{ud} starts with a linear elastic stage followed by an inclination branch characterizing a linear strain-hardening relationship up to the strain limit, which was recommended to be 0.9 times of the ultimate strain limit ε_{uk}. The other model recommended for cross-section design used a horizontal top branch to assume the stress-strain behavior after the yield point in the plastic range. Since the linear elastic range is of interest in this study, the model with a stress plateau is adopted to capture the linear behavior of the stress-strain relation of prestressing steel in tension.

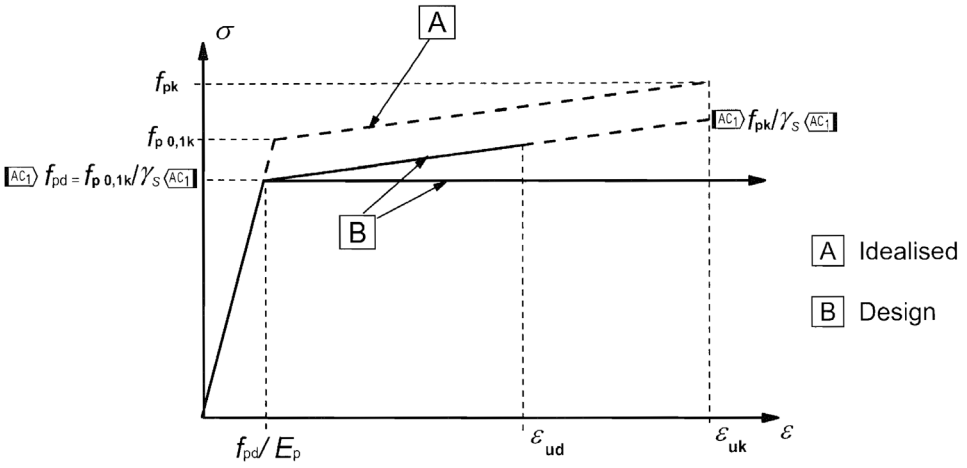

Figure 2-11. Comparison of idealized and design stress-strain behavior of prestressing steel in Eurocode (The European Union Per Regulation 305/2011, 2004)

2.2.2. Design Fatigue Strength

Analysis of the fatigue behavior of steel in the Model code 2010 (fib, 2013) was recommended developing S-N curves to determine the stress limit under cyclic loads. Models for calculating the stress ranges of reinforcing and prestressing steel under fatigue loads used linear elastic assumption, indicating that the stress increases proportionally to the strain as the load increases. The fatigue requirement for steel can be met if the maximum stress range under the critical load combination is less than the designed capacity in the steel, which can be written as

$$\gamma_{Ed} max \Delta\sigma_{Es} \leq \Delta\sigma_{Rsk}/\gamma_{s,fat} \quad (2\text{-}17)$$

where

$\Delta\sigma_{Rsk}$ is the steel stress range obtained from a characteristic fatigue strength function at 10^8 cycles and its values are given in Table 2-1and Table 2-2 for reinforcing and prestressing steel, respectively;

$\Delta\sigma_{Es}$ is the damage equivalent stress range for steel calculated from the acting loads;

$\gamma_{Ed} = 1.1 \; or \; 1.0$ if the stress analysis is conservative and verified by in-situ observation; and

$\gamma_{s,fat} = 1.15$ is a safety factor for steel.

Table 2-1. Parameters of S-N curves for reinforcing steel

	N^*	Stress exponent		$\Delta\sigma_{Rsk}\ (MPa)$	
		k_1	k_2	at N^* cycles	at 10^8 cycles
Straight and bent bars $D(mandrel\ diameter) \geq 25\phi(bar\ diameter)$	10^6	5	9	210	125
$\phi \leq 16\ mm$	10^6	5	9	160	95
$\phi > 16\ mm$	10^6	5	9	*	*
Bent bars $D < 25\phi$	10^7	3	5	50	30

Note: *Fatigue strength for those bars is the value for corresponding straight bars reduced by a factor that depends on the ratio of D/ϕ.

Table 2-2. Parameters of S-N curves for prestressing steel

	N^*	Stress exponent k_1	Stress exponent k_2	$\Delta\sigma_{Rsk}$ (MPa) at N^* cycles
Pretensioned steel				
Straight strands and wires	10^6	5	9	185
Post-tensioned steel				
Single strands in plastic ducts	10^6	5	9	185
Straight tendons or curved tendons in plastic ducts	10^6	5	10	150
Curved tendons in steel ducts	10^6	5	7	120
Splicing devices	10^6	5	5	80

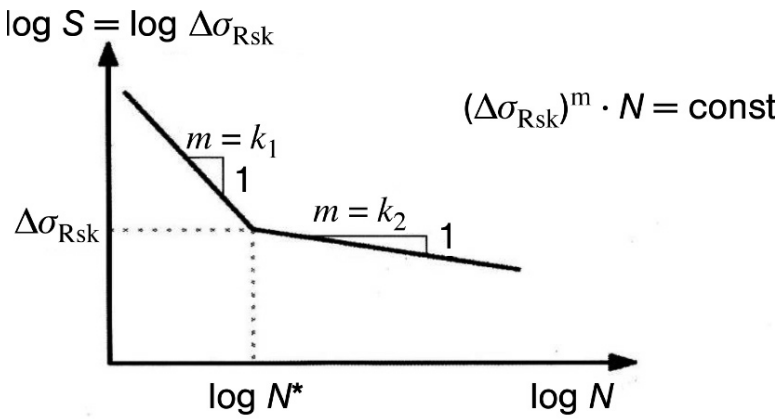

Figure 2-12. An S-N curve for steel (CEB-FIP, 2010)

2.3. Fatigue Design for Concrete Wind Towers

2.3.1. Equivalent Damage Model from CEB-FIP 2010

Linear elastic model of the concrete stress-strain behavior in the new Model Code (fib, 2013) was used to analyze the stress for reinforced and prestressed concrete members under fatigue loading. In practice, the required lifetime due to the applied load needs to be lower or equal to the number of cycles to failure. To fulfill the fatigue requirement, the maximum stress in steel $max\Delta\sigma_{Es}$ calculated under the combination of loads should meet the

requirement in Equation (2-17) and the maximum concrete stress $\sigma_{c,max}$ should check with the qualification below.

$$\gamma_{Ed}\sigma_{c,max}\eta_c \leq 0.45 f_{cd,fat} \quad (2\text{-}18)$$

where

η_c is an averaging factor to count for the stress gradient of concrete in the compression zone and equals to $\eta_c = \frac{1}{1.5-0.5|\sigma_{c1}|/|\sigma_{c2}|}$;

$|\sigma_{c1}|$ is the minimum absolute value of the compressive stress within 300 mm from the surface under the relevant load combination of actions; and

$|\sigma_{c2}|$ is the maximum absolute value of the compressive stress within 300 mm from the surface under the same load combination as that for which $|\sigma_{c1}|$ was determined in Figure 2-13. Definition of stress $|\sigma_{c1}|$, $|\sigma_{c2}|$.

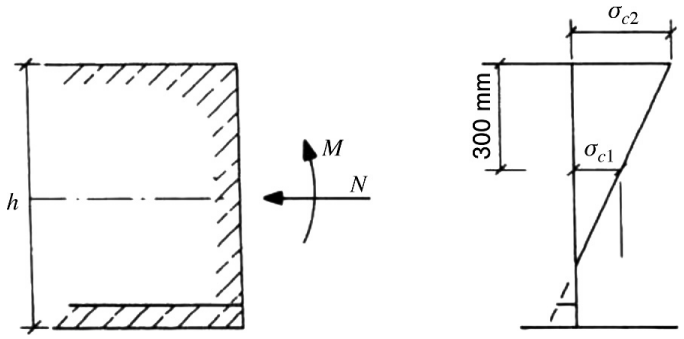

Figure 2-13. Definition of stress $|\sigma_{c1}|$, $|\sigma_{c2}|$

If the designed compressive strength in concrete does not satisfy the criteria above, a detailed calculation regarding the concrete stresses under fatigue loading needs to be carried out as follows.

a) Pure Compression:

If $S_{cd,min} > 0.8$, the S-N curve in Figure 2-14 for $S_{cd,min} = 0.8$ applies;

If $0 \leq S_{cd,min} \leq 0.8$, the $\log N$ can be calculated as follows:

$$\log N_1 = \frac{8}{Y-1}(S_{cd,max} - 1) \quad (2\text{-}19)$$

$$\log N_2 = 8 + \frac{8 \cdot \ln(10)}{Y-1}(Y - S_{cd,min}) \cdot \log(\frac{S_{cd,max} - S_{cd,min}}{Y - S_{cd,min}}) \quad (2\text{-}20)$$

with:

$$Y = \frac{0.45 + 1.8 \cdot S_{cd,min}}{1 + 1.8 S_{cd,min} - 0.3 S_{cd,min}^2} \quad (2\text{-}21)$$

$$S_{cd,max} = \gamma_{Ed} \sigma_{c,max} \eta_c / f_{cd,fat} \quad (2\text{-}22)$$

$$S_{cd,min} = \gamma_{Ed} \sigma_{c,min} \eta_c / f_{cd,fat} \quad (2\text{-}23)$$

$$\Delta S_c = |S_{cd,max}| - |S_{cd,min}| \quad (2\text{-}24)$$

where

(a) if $\log N_1 \leq 8$, then $\log N = \log N_1$;

(b) if $\log N_1 > 8$, then $\log N = \log N_2$.

The design fatigue reference strength for concrete in compression is introduced to count for the increasing fatigue sensitivity with increasing compressive strength and expressed as

$$f_{cd,fat} = \beta_{cc}(t) \beta_{c,sus}(t, t_0) f_{ck} \left(1 - \frac{f_{ck}}{400}\right) / \gamma_{c,fat} \quad (2\text{-}25)$$

b) Compression-tension with $\sigma_{ct,max} \leq 0.026 |\sigma_{c,max}|$:

$$\log N = 9(1 - S_{c,max}) \quad (2\text{-}26)$$

c) Pure tension and tension-compression with $\sigma_{ct,max} > 0.026 |\sigma_{c,max}|$:

$$\log N = 12(1 - S_{ct,max}) \quad (2\text{-}27)$$

$$S_{ct,max} = \sigma_{ct,max} / f_{ctk,min} \quad (2\text{-}28)$$

where

N is the number of cycles to failure;

$S_{c,max}$ is the maximum compressive stress level due to the design load combination;

$S_{c,min}$ is the minimum compressive stress level due to the design load combination;

$S_{ct,max}$ is the maximum tensile stress level due to the design load combination;

ΔS_c is the stress level range;

$\sigma_{c,max}$ is the maximum compressive stress under the upper load effect in MPa;

$\sigma_{c,min}$ is the minimum compressive stress in MPa at the same level which $\sigma_{c,max}$ occurs;

$\sigma_{ct,max}$ is the maximum tensile stress in MPa;

f_{ck} is the characteristic cylinder compressive strength determined at 28 days in MPa;

$f_{cd,fat}$ is the fatigue reference compressive strength calculated from Equation (2-25);

$f_{ctk,min}$ is the minimum tensile strength in MPa (fracture strength);

$\beta_{cc}(t)$ is the coefficient which depends on the age t of concrete at the beginning of a fatigue test. If considering the temperature effects on the maturity of concrete, t may be adjusted as t_T, which is calculated as $t_T = \sum_{i=1}^{n} \Delta t_i \, exp\left[13.65 - \frac{4000}{273+T(\Delta t_i)}\right]$, where Δt_i is the number of days where a temperature T prevails, and $T(\Delta t_i)$ is the mean temperature in ℃ during the time period Δt_i.

$\beta_{c,sus}(t, t_0)$ is defined the same as the previous section;

t is the age of the concrete at loading in days;

$t - t_0$ is the time under fatigue loads in days; and

$\gamma_{c,fat}$ is the safety factor for concrete and equals 1.5.

d) Fatigue damage D was defined as the Palmgren-Miner sum for a spectrum of load levels. The value of this summation is between 0.2 and 1.0, and the damage analysis is based

on the linear damage approach of Palmgren-Miner, which assumes that each damage caused by every load cycle accumulates linearly until failure of the structural component. The accumulative damage D can be calculated as

$$D = \sum_{i=1}^{j} \frac{n_{Ei}}{N_{Ri}} \leq D_{lim} \qquad (2\text{-}29)$$

where

n_{Ei} is the number of fatigue cycles at the stress level i of steel and concrete; and

N_{Ri} is the number of fatigue cycles to failure at the same stress level i of steel and concrete. For steel, it can be estimated from the steel S-N curves given in Table 2-1 and Table 2-2; and for concrete, its value can be estimated from the above calculations.

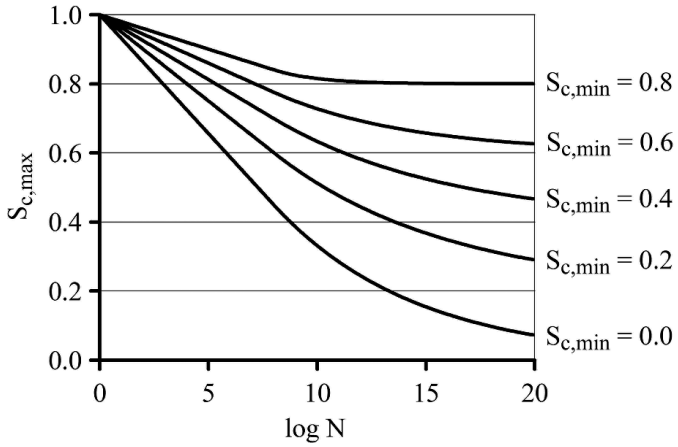

Figure 2-14. S-N curves of plain concrete according to CEB-FIP Model Code 2010

2.3.2. Concrete Structures for Wind Turbines

Detailed design guidelines completed by Grünberg and Göhlmann (Grünberg & Göhlmann, 2013) suggested using the analyzing method in line with Model Code 1990 to serve as the basis for designing concrete structures for onshore wind towers.

One major difference from the new version of Model Code is that a smaller design fatigue strength of concrete in compression was used, which is determined as

$$f_{cd,fat} = \beta_{cc}(t)\beta_{c,sus}(t,t_0)f_{ck}\left(1-\frac{f_{ck}}{250}\right)/\gamma_{c,fat} \quad (2\text{-}30)$$

where all parameters are consistent with the new code. A larger factor of $\left(1-\frac{f_{ck}}{400}\right)$ applied in the new code intends to increase the fatigue resistance of concrete structure based on the recent analysis. Using the relatively conservative estimate of the fatigue strength in Equation (2-30), a reduced fatigue capacity is expected if the structure life span is assumed to be consistent with the new Model Code, especially when the design fatigue life is below 2×10^8 cycles (Figure 2-15).

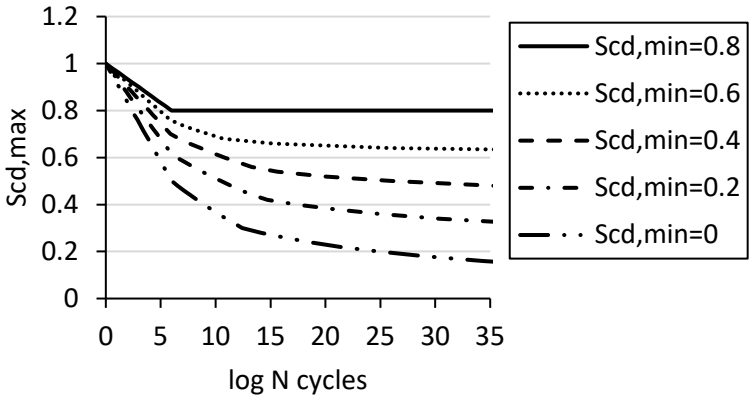

Figure 2-15. S-N curves of plain concrete according to CEB-FIP Model Code 90

2.3.3. Japan Society of Civil Engineers

Fatigue data was usually presented by a relationship between the stress ratio and the number of loading cycles N. In the Japanese code (Japan Society of Civil Engineers, 2008), the design compressive and flexural strength of HPFRCC under repeated loads f_{rd} were assumed to be affected by the static load induced stress σ_p and the fatigue life N when the

loading cycles are smaller than 2 million cycles. The design fatigue strength can be determined by

$$f_{rd} = 0.85 f_d (1 - \frac{\sigma_p}{f_d})(1 - \frac{\log N}{17}) \quad (2\text{-}31)$$

To examine the design fatigue capacity, the calculated fatigue strength needs to be verified by the following equation:

$$\frac{\gamma_i \sigma_{rd}}{f_{rd}/\gamma_c} \leq 1.0 \quad (2\text{-}32)$$

where

σ_p is the design stress at permanent load in MPa;

f_d is the compressive strength of HPFRCC in MPa;

f_{rd} is the design fatigue strength in MPa;

γ_c is the safety factor of HPFRCC in the fatigue limit state and equals to 1.3; and

σ_{rd} is the stress due to variable load in MPa.

2.4. References

Aaleti, S. R., Sritharan, S., Bierwagen, D., and Wipf, T. J. (2011). Experimental Evaluation of Structural Behavior of Precast UHPC Waffle Bridge Deck Panels and Connections. In *Transportation Research Board 90th Annual Meeting Compendium of Papers,* Vol. 2251, pp. 82–59. Washington, D.C., USA.

ACI Committee 318. (2014). *Building Code Requirements for Structural Concrete and Commentary*. American Concrete Institute, Farmington Hills, MI. Vol. 2007.

ACI Committee 544. (2018). *Guide to Design with Fiber-Reinforced Concrete*. Farmington Hills, MI, USA.

Acker, P., and Behloul, M. (2004). Ductal Technology: a Large Spectrum of Properties, a Wide Range of Applications. In *Proceedings of the International Symposium on Ultra High Performance Concrete* (pp. 11–24). Kassel, Germany: Kassel University Press.

Association Francaise de Genie Civil (AFGC). (2013). *Betons fibres a ultra-hautes performances: recommendations*.

Association Francaise de Normalisation (AFNOR — French Standard Institute). (2016). *National addition to Eurocode 2 - Design of concrete structures: specific rules for*

Ultra-High Performance Fibre-Reinforced Concrete (UHPFRC) (2016–04–P ed., Vol. 33). Association Francaise de Normalisation (AFNOR - French standard institute).

Graybeal, B. A. (2010). *Behavior of Field-Cast Ultra-High Performance Concrete Bridge Deck Connections Under Cyclic and Static Structural Loading*. FHWA-HRT-11-023. Federal Highway Adminstration: McLean, VA, USA.

Graybeal, B. A. (2013). *Ultra-High Performance Concrete : A State-of-the-Art Report for the Bridge Community*. Federal Highway Adminstration: McLean, VA, USA. https://doi.org/FHWA-HRT-13-060

Grünberg, J., and Göhlmann, J. (2013). *Concrete Structures for Wind Turbines*. *Concrete Structures for Wind Turbines*. Ernst & Sohn: Berlin, Germany. https://doi.org/10.1002/9783433603291

International Federation for Structural Concrete (Federation internationale du beton [fib]). (2013). *CEB-FIP Mode Code for Concrete Structures 2010*. Wilhelm Ernst & Sohn: Lausanne, Switzerland. Retrieved from www.fib-international.org

Japan Society of Civil Engineers. (2008). Recommendations for Design and Construction of High Performance Fiber Reinforced Cement Composites with Multiple Fine Cracks (HPFRCC). *Concrete Engineereing Series*, 82, Testing Method 6-10. https://doi.org/http://dx.doi.org/10.1016/j.dci.2010.01.003

Larsson, R. (2008). *CEB Bulletin 42 Constitutive Modelling of High Strength/ High Performance Concrete - State-of-Art Report*. Engineering. Lausanne, Switzerland.

Naaman, A. E. (2007). High Performance Fiber Reinforced Cement Composites in High Performance Construction Materials - Science and Application. World Scientific Publishing Co. Pte. Ltd.

Schmidt, M., and Fehling, E. (2005). Ultra-High-Performance Concrete: Research, Development and Application in Europe. *Seventh International Symposium on the Utilization of High Strength/High-Performance Concrete*, 51–78. Retrieved from http://download.contec-aps.com/uploads/tx_mpdownloadcenter/pp_fp_2005_003_eng_01.pdf

Sritharan, S., Bristow, B. J., and Perry, V. H. (2003, October). Characterizing an Ultra-High Performance Material For Bridge Applications Under Extreme Loads. *3rd International Symposium on High Performance Concrete*, Montpellier, France.

The European Union Per Regulation 305/2011. (2004). *Eurocode 2: Design of concrete structures - Part 1-1: General rules and rules for building*. *The European Union Per Regulation*. Brussels, Belgium: European Committee for standardization. https://doi.org/10.2514/2.2772

Vandewalle, L., Demegeer, D., Balazs, G. L., Barr, B., Barros, J. A. O., Bartos, P., et al., (2003). Final Recommendation of RILEM TC 162-TDF: Test and Design Methods for Steel Fibre Reinforced Concrete Sigma-Epsilon-Design Method. *Materials and Structures*, *36*(262), 560–567. https://doi.org/10.1617/14007

CHAPTER 3. AN EVALUATION OF WIND ENERGY PRODUCTION AT ELEVATED HUB HEIGHTS

A paper to be submitted to a wind energy related journal

Bin Cai[1], Phuong Vo[1], Sri Sritharan[1], and Eugene S. Takle[2]

[1] *Department of Civil, Construction, and Environmental Engineering, Iowa State University, Ames, IA 50011, USA*

[2] *Department of Geological and Atmospheric Science, Iowa State University, Ames, IA 50011, USA*

3.1. Abstract

Since the 1980s, the levelized cost of energy (LCOE) from wind has declined six-fold in the U.S., while hub height has gone from about 20 to 80 plus meters. A further increase in hub height is expected to enhance wind energy production and subsequently reduce the energy cost. Since wind resource information is limited at elevated heights, it is a challenging task to predict the annual energy production (AEP) at new heights and determine the corresponding LCOE. To promote the use of tall towers, this paper uses reliable wind data collected up to 200 m above ground and establishes the AEP increase offered by achieving higher hub heights at multiple sites. The calculation procedure of AEP is validated by comparing the wind generation data from Midcontinent Independent System Operator with the AEPs for a site in Homestead (Iowa, USA). There are negligible variations found in the diurnal and seasonal cycles of the normalized energy production among these data sources, indicating that the procedure is suitable for estimating wind energy production. The AEP results further suggest that with a 20 m increase in hub height from 80 m, the energy production can increase by up to 10 percent. Such a nonlinear increase of AEP with hub height indicates that tall wind turbine towers should use an optimal hub height to continue to reduce the LCOE as opposed to using a standard height at all locations. To broaden the estimation of AEP at elevated hub heights, wind information from the National Renewable

Energy Laboratory (NREL) Wind Integration National Dataset (WIND) Toolkit are examined instead of using measured data. The WIND Toolkit is found to be appropriate as it leads to somewhat conservative results.

KEYWORDS
tall tower; field measurement; wind speed; annual energy production; levelized cost of energy; WIND Toolkit

3.2. Introduction

Wind power cost expressed in terms of the levelized cost of energy (LCOE) have decreased nearly 40 percent within the past decade in the United States and are expected to reduce by an additional 9 percent by 2020 and 16 percent by 2030 (U.S. Department of Energy (DOE), 2015; Lantz, 2012; DOE, 2015). Cost savings are estimated using the current wind technologies. To further reduce the LCOE, one economical solution is to focus on the development of tall wind turbine towers as an increase in hub height exposes a wind turbine to faster and steadier wind speeds, thereby helping prolong the wind harvesting time. With a higher wind energy potential, a tall tower will likely offset the additional capital cost and reduce the LCOE (Engström et al., 2010; Sritharan, 2016). An added advantage of using tall towers in the U.S. is that they can increase the gross area for developing wind energy by 54 percent and 67 percent when turbine hub heights of 110 m and 140 m are used, respectively (DOE, 2015, 2014). Both increments are with respect to an 80 m hub height as a baseline and assume a gross capacity factor of 35 percent or higher. Expanded gross areas will significantly influence the wind-rich regions, such as Iowa, Minnesota and Texas, which attribute to most of the U.S. wind generation today and account for more than half of the total wind installations from 2012 and 2019 (DOE, 2014, 2019). If the standard hub height of 80 m is maintained, land-based wind power production will not be possible in southeastern

states such as Tennessee and Carolinas. However, increasing the turbine hub height to 110 m to 140 m in this region would offer a tremendous amount of added gross area that is suitable for wind energy production. As a result, wind power can be produced in all 50 states in the U.S. (DOE, 2015) and will result in significant increase in nation's wind power production, facilitating accomplishment of various wind vision scenarios set forth by the U.S. Department of Energy (DOE, 2014, 2019; American Wind EnergyAssociation (AWEA), 2019).

Since the 1980s, the power capacity of a commercial wind turbine in the U.S. has increased from approximately 100 kilowatts to an average of 2.4 MW. Over the same period, the hub height and rotor diameter have increased by four to five folds to average values of 88 m and 116 m in 2018, respectively (AWEA, 2019) . In the interior region, which includes the state of Iowa, the typical hub height for turbines built in 2018 ranges from 80 to 90 m, and it has been a common practice in the U.S. for wind turbines to be supported by 80-m tall tubular steel towers. They are prefabricated in three sections with a diameter for the base section reaching just over 4.0 m. When this dimension exceeds 4.3 m, delivering tower sections over highways and railroads becomes impossible due to the transportation restrictions. Taller tubular steel towers will have a larger base diameter and exponentially increased weight, both of which cause transportation challenges (DOE, 2015; Wise et al., 2019; International Electrotechnical Commission (IEC), 2005; Lewin & Sritharan, 2010; Sritharan, 2015). Although tubular towers can be segmented for transportation purposes, assembling them in the field increases the cost significantly and adds new maintenance challenges (DOE, 2015; Cotrell et al., 2014). As a result, technology such as Hexcrete has been introduced with support from the Department of Energy to overcome the

aforementioned challenges and facilitate building of taller towers. The Hexcrete tower technology (Sritharan, 2016, 2015), which uses prefabricated modular segments to assemble a tapered concrete tower with prestressing, has been used to complete design of concrete and hybrid towers for heights up to 140 m (see Figure 3-1) .

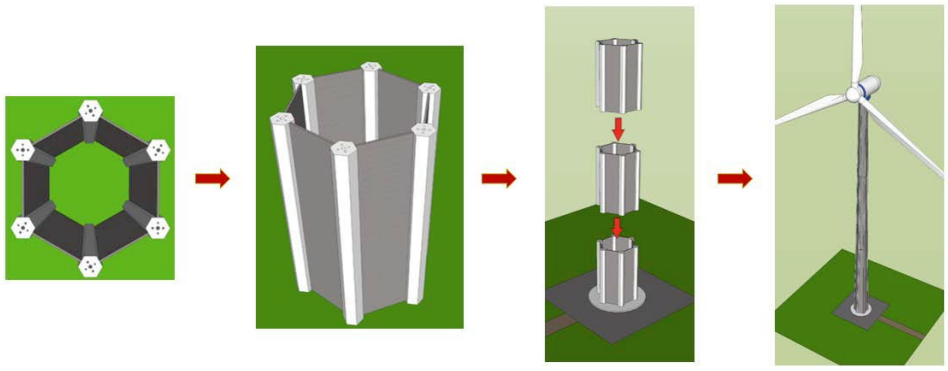

Figure 3-1. Hexcrete tower technology concept

To support the growing trend in the turbine capacity and rotor diameter in the wind energy industry, an increase in hub height is inevitable (Lantz et al., 2019). This increase in hub height will elevate the tower cost and therefore, the use of the tall tower technology should ideally be justified using LCOE that accounts for both the AEP and tower costs. However, the information on the cost of tall towers is limited in the U.S. because the corresponding technologies have not matured. Therefore, this paper focuses on estimating the AEP at elevated hub heights as it helps advance the knowledge towards estimating the LCOE of tall towers accurately.

It is worth noting that as tall tower technologies mature, the expectation is that the corresponding LCOE will be reduced because: 1) the number of towers per wind farm will be lessened; 2) these tower technologies are likely to be built with alternative cranes instead of large crawler cranes as currently used by the industry; and 3) the balance of system cost will be reduced since the new technologies could offer advantages in transportation and erection

(Lantz et al., 2019; Barutha et al., 2019; Moné et al., 2015) . However, detailed wind resource at elevated heights is not widely available in the U.S., making it impossible to establish reliable AEP calculations and justify the use of tall wind towers. Due to the lack of wind data at higher elevations, extrapolation methods use datasets at relatively lower heights and the $1/7^{th}$ power law to forecast wind speed and wind power at the new hub heights (Takle, Brown, & Davis, 1978). Given the spatial variations of wind speed, a constant power-law exponent would not produce accurate forecasts (Storm et al., 2009; Walton, Takle, & Gallus, 2014). Furthermore, relying on mean values or short-period wind observations collected at higher elevations over a period of less than a year can cause significant errors in making AEP predictions, even at a site where the data were collected. These discrepancies are largely attributed to the lack of understanding and inaccurate representation of diurnal and seasonal variations of wind speeds and the power-law exponent (Takle, Brown, & Davis, 1978; Walton, Takle, & Gallus, 2014; Kelley et al., 2004; Schwartz & Elliott, 2005; Redburn, 2007; Davenport, 1961; Petersen et al., 1998). In addition, it is important to establish validated wind power production models so that they can be utilized in the AEP and subsequently in the LCOE calculations.

Recognizing that reliable wind data are required to establish accurate AEPs for taller wind turbine towers, this paper utilizes measured wind data obtained over heights up to 200 m elevations from five sites in Iowa and one site in Minnesota and quantifies various AEPs and the corresponding trends as a function of hub height. The variation in wind speed and power laws as a function of height, diurnal and season cycle are first examined. A robust model for calculating wind power production is then established and validated. Finally, the energy production potentials at elevated heights are determined and the net AEPs and

capacity factors are assessed. As an alternative of using measured wind data, the paper also explores the potential use of the National Renewable Energy Laboratory (NREL) Wind Integration National Dataset (WIND) Toolkit—a commonly-used public online database. By using a site in Iowa with measured data, it is determined whether the Toolkit is an effective tool for estimating the AEPs and capacity factors for tall wind towers (Draxl et al., 2015). It is noted that WIND Toolkit data were established using Weather Research and Forecasting model to simulate the wind resource information.

3.3. Wind data

Wind data used in this study are summarized in Table 3-1, which includes the locations of various stations. The field data in Iowa were acquired from the Iowa Energy Center and measured from wind meteorological towers at five wind stations, namely Quimby, Palmer, Mason City, Altoona, and Homestead (AWS Truepower, 2010) , as identified in Figure 3-2. These sites are located in different wind resource regions as seen in the figure that also depicts the wind speed at 80 m elevation. The sites in the northeast have relatively more favorable wind conditions than those in the southeastern part of the state. These five towers were instrumented at 50, 100, 150, and 200 m to collect wind-energy resource data from December 2006 to April 2009, except Palmer which was not instrumented at 200 m. Acquired wind data characteristics included temperature, mean wind speed, wind speed standard deviation, mean wind direction, and wind direction standard deviation. All measurements were recorded at 10-minute intervals for all heights, and the time was recorded in local standard time.

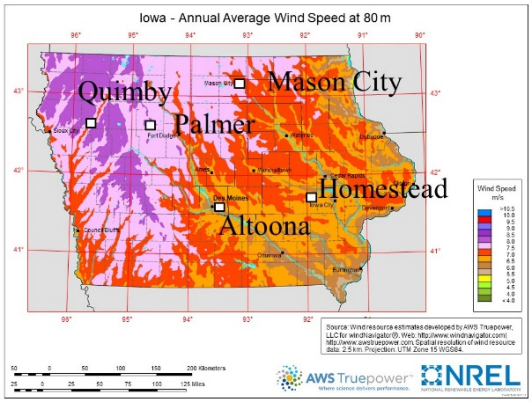

Figure 3-2. Annual average wind speed for the five wind stations in Iowa at 80 m height (DOE, 2017). The squares denote the site of a tall meteorological tower used for assessing wind power potential.

Table 3-1. Summary of locations of meteorological towers

Location	Terrain Exposure	Meteorological Tower Instrumented Heights	Data Period and Data Variables
Homestead, IA	Hilly, rural area with a river to the north	Four heights: 50, 100, 150, and 200 m (Applies to Homestead, Altoona, Quimby, Mason City, and Palmer that did not have measurements at 200 m)	December 2006 – April 2009; data variables include wind speed and direction, and air temperature (Applies to Homestead, Altoona, Quimby, Mason City, and Palmer)
Altoona, IA	Suburban housing surrounding with a flat area to the southeast		
Quimby, IA	Hilly, rural area with a small river to the southeast		
Mason City, IA	Flat, rural area with a lake to the southeast, urban area to the southwest		
Palmer, IA	Flat, rural area with a lake to the northeast		
Rosemount, MN	Flat, rural area with the Twin Cities urban area to the north	Ten heights: 125.9, 101.5, 76.7, 51.5, 27.1, 7.3, 127.9, 79.1, 29.6, and 9.9 m	One-month data in July 2014; data variables include wind speed and direction, air temperature, relative humidity, and barometric pressure at 76.7 m

Table 3-2. Summary of missing or unavailable wind data in Homestead

Height	Wind Speed		Wind Direction	
	Daytime	Nighttime	Daytime	Nighttime
50 m	1.33%	1.59%	13.33%	9.4%
100 m	3.65%	3.17%	37.75%	35.71%
150 m	4.46%	4.21%	13.68%	11.12%
200 m	30.85%	36.29%	40.71%	42.61%

The data at meteorological towers, including periods of downtime when icing and lightning events occurred, were collected by sensors and controlled by replacing missing times with "NaN". For a detailed description of the datasets used in Iowa, the reader can refer to the study completed by Walton (Walton, Takle, & Gallus, 2014). To demonstrate the analyses of the wind data and estimation of AEPs at different heights, Homestead is used herein as an example site. Missing or unavailable data for Homestead, IA from heights 50 to 200 m are indicated in Table 3-2. The wind speed and direction data were chosen to characterize the diurnal and seasonal variations of wind shear in the rotor layer which is between 50 m and 150 m. Within this range, wind measurement data loss was less than 5%; data loss of above 30% occurred to the wind direction measurement at 100 m in Homestead, IA. In addition, wind speed data were validated as part of this study by comparing against the measurements from nearby wind stations to ensure that the collected data sufficiently represent the variations in the wind speed over time. Note that the wind speed percentages at this site for heights from 50 to 150 m are small and this applies for the remaining sites as well. Since these values are small and AEP is calculated based on the accumulation of average hourly energy productions in this study, it is acceptable to exclude the missing wind speeds from this range when determining the wind characteristics and energy productions at the desired hub height.

To calculate AEP, two methods are tested. It is found that the AEP values for any given hub height are similar to the averaged AEP values calculated from the wind data at the top and bottom of the rotor layer. For this reason, analyses are completed using the former method as it requires fewer data and computations. Regarding the information used to assess the energy production for hub heights up to 140 m, only wind speed distribution from 50 to 150 m is needed as this range covers the hub height in which rotors are operating.

Another dataset that has been used in this study is the Eolos wind research station at Rosemount, MN, which provides wind measurements including wind speed, wind direction, temperature, air density and pressure, and humidity (Showers, 2014). This monitoring center records information from a Clipper Liberty 2.5 MW wind turbine and a 130 m (426 ft.) tall meteorological tower, which was instrumented at ten different heights to record wind data every one minute. As with the Iowa data, each dataset from Rosemount was filtered by replacing unavailable and error data points with "NaN"s to eliminate the effects of random events.

As previously noted, data used for analyzing energy production also include numerically simulated datasets from the NREL Techno-Economic WIND Toolkit. Wind data collected from this toolkit pertain to wind speed and direction, temperature, air density and pressure of more than 126,000 wind farm sites across the nation. Simulated wind data were modeled based on nearby wind tower data, and the wind information was created at a five-minute interval from January 2007 to December 2012 (Draxl et al., 2015; King, Clifton, & Hodge, 2014). Again, Homestead is used as an example site for examining the simulated data based on the WIND Toolkit and determining how well this data could be used for estimating the AEPs.

3.4. Assessment of Energy Production Potential

Prediction of the energy production potential from a wind turbine or a wind plant depends on estimates of wind speeds within the rotor layer and turbine capacity. Because wind speeds increase nonlinearly with height, the power-law relationship is used to describe the relationship between wind speed and height above sea level, which can be written as (Davenport, 1961; Petersen et al., 1998)

$$\frac{u_2}{u_1} = \left(\frac{z_2}{z_1}\right)^{\alpha} \qquad (3\text{-}1)$$

where u_1 and u_2 are the wind speeds measured at heights z_1 and z_2, respectively. Note that the wind speed observations u_1 and u_2 are in the form of either time histories or average values for a specified period. This relationship calculates wind speeds at desired heights using the observations at the referenced height and the power-law exponent α, which is frequently used to illustrate the effects of surface roughness. The α value falls in the range of $0.05 \leq \alpha \leq 0.5$, but is commonly considered a constant exponent of 1/7 when adequate topographic information is unavailable and has been used power production estimates (Moné et al., 2015; Takle, Brown, & Davis, 1978).

Equation (3-1) is used to calculate the mean wind speed above measurement heights, which estimates the potential wind resource for a given area. However, it cannot be used to estimate the energy production if it fails to reflect the wind speed variations that occur over a period. One method to capture the variations of wind speed is to use the Weibull distribution, which is used to describe the scale and shape of wind speed distributions (Celik, 2003; García-Bustamante et al., 2008; Deaves & Lines, 1997; Hennessey, 1977). The corresponding probability density function is defined using Equation (3-2)

$$f(v_i;\eta,\beta) = \frac{\beta}{\eta}\left(\frac{v_i}{\eta}\right)^{\beta-1} \exp\left[-\left(\frac{v_i}{\eta}\right)^{\beta-1}\right], v_i > 0 \qquad (3\text{-}2)$$

where η is the shape factor depending on the flatness of the distribution, and β is the scale factor of the distribution. Both of these variables can be determined by statistical methods, such as the maximum likelihood estimate method (Meeker & Escobar, 1998). Furthermore, v_i values represent the average wind speed over a short time frame (e.g., 10 minutes) (Moné et al., 2015), and the Weibull probability density function $f(v_i;\eta,\beta)$ serves as the basis for calculating the frequency distribution of each wind speed increment.

Combining the probability distribution of wind speeds with the provided power curve, annual energy production can provide an estimate of wind power potential on an annual basis and be calculated using Equation (3-3) to Equation (3-5)

$$AEP_{gross} = \sum_{k=1}^{12}\left\{\sum_{j=1}^{d}\left[\sum_{h=1}^{24}\left(\frac{\sum_{i=1}^{m} E(v_i)}{m}\right)*6\right]\right\} \qquad (3\text{-}3)$$

$$E(v_i) = P(v_i)p(v_i) \qquad (3\text{-}4)$$

$$AEP_{net} = AEP_{gross} \times losses \times availability \qquad (3\text{-}5)$$

where v_i in this study uses 10-minute average wind speed established from the raw data unless otherwise noted; $P(v_i)$ and $p(v_i)$ are the electric power output and number of occurrences for wind speed v_i, respectively; and m is the total number of available data points for each hour per month, considering missing data. The product of power output and the number of occurrences for wind speed v_i provides wind energy production $E(v_i)$ for each wind speed increment. Thus, the 10-minute average energy production for each hour per month is the sum of $E(v_i)$ in the same hour per month divided by the amount of available 10-minute wind speed samples m. An estimation of the average hourly power potential can be

obtained by multiplying $E(v_i)$ by six, which denotes the number of 10-minute intervals in an hour. Summing the hourly energy production for total hours within a single year provides the AEP. This approach for estimating the wind power potential is based on the use of the 10-minute frequency distribution of wind speed within each hour and the given power curve obtained from the turbine manufacturer. To determine AEP from a set of 1-minute average wind data acquired from the Minnesota wind station, the hourly power potential is computed by multiplying the 1-minute average energy production for each hour per month $\frac{\sum_{i=1}^{m} E(v_i)}{m}$ by sixty, the number of minutes in each hour. To verify that the 1-min wind data from Rosemount provide acceptable time-intervals, 10-min average wind data were tested and found that there were minimal differences in energy production at given heights. Therefore, this paper uses the original 1-min wind data for this particular site as this provides a means to examine the AEP production using different time intervals.

In this study, the net AEP is explicitly calculated for two utility-scale turbines, which are a 2.3 MW turbine with 108-m rotor diameter and a 3.2 MW turbine with 113-m rotor diameter. They were chosen since the power curves for these two Siemens turbines are readily available (Studylib, n.d.; Wind-turbine-model.com, n.d.).

With considerations to production losses, the analysis of net AEP conducted here applies the losses assumptions from the 2013 NREL Cost of Wind Energy Review that are associated with turbines and sites (Moné et al., 2015). These assumptions include: (1) a 15% reduction to account for array wake losses, electric collection and transmission losses, and blade soiling losses; and (2) turbine availability of 98% indicating that wind turbines produce power between the cut-in and cut-out speed 98% of the time (Moné et al., 2015; Krohn, Morthorst, & Awerbuch, 2009). Additionally, to remain consistent with the NREL study,

assumptions used to characterize the air density and altitude above sea level at selected wind farm sites are: (1) the average air density of 1.163 kg/m^3 at the hub height of 80 m, and (2) the altitude above mean sea level of 450 m for the Midwest region of the United States (Moné et al., 2015). Due to lack of information, a constant air density was assumed for estimating power production in Iowa. However, for Rosemount, air density was adjusted by introducing virtual temperature to different hub heights. This process can be obtained by applying the air pressure, ambient temperature and relative humidity measurements into the hydrostatic expression, all of which were available for this site (List, 1951). Monthly energy production from the varied air density showed less than a 2% difference compared to the results from the non-adjusted air density, justifying the use of a constant air density for the sites.

The other important quantity to evaluate the wind energy production is capacity factor, which can be obtained from the net AEP and calculated from Equation (3-6)

$$\text{Net Capacity Factor} = \frac{\text{AEP}_{\text{net}}}{\text{turbine capacity}*8760} * 100\% \qquad (3\text{-}6)$$

where net capacity factor is the nominal power capacity for a selected turbine; 8760 denotes the number of total hours in a single year; AEP_{net} is the net annual energy production determined from Equation (3-5). Net capacity factor as well as net annual energy production are criteria to compare power potentials among various sites and provide insights into determining the most productive and profitable locations to build wind farms. Since all the calculations in this paper include the assumed losses and reduction factors, reported AEP and capacity factor in the remainder of the paper reflect the net production.

3.5. Validation of AEP

The measured wind data at 100 m from Homestead is used as an example to assess the ability of the AEP model in estimating wind energy production. To do this, wind speed and power-law exponent are first analyzed using procedures outlined in the previous section. Hourly averages of wind speeds obtained from the on-site measurements are plotted as a function of time in Figure 3-3. This figure exhibits different diurnal trends of wind speed for the four meteorological seasons. Field measurements show higher wind speeds during nighttime (1800 – 0600 LST, where LST stands for Local Standard Time) than daytime (0600 – 1800 LST), which agrees well with the diurnal patterns of wind speeds from early studies (Walton, Takle, & Gallus, 2014; Kelley et al., 2004). Wind speeds from the field samples show their maximum at around midnight and their minimum around noon. The mean wind speed at nighttime is between 6.0 and 8.0 m/s in the summer (June, July, August, i.e., JJA) and between 8.5 and 9.5 m/s during the following seasons: spring (March, April, May, i.e., MAM), fall (September, October, November, i.e., SON), and winter (December, January, February, i.e., DJF). During daytime, the mean wind speed differs less than that observed for the nighttime hours and shows an average of 5.5 m/s in the summer and 7.9 m/s in other seasons. Although the wind speeds during the summer are lower than other seasons, the diurnal variations exhibit a similar pattern to the other seasons.

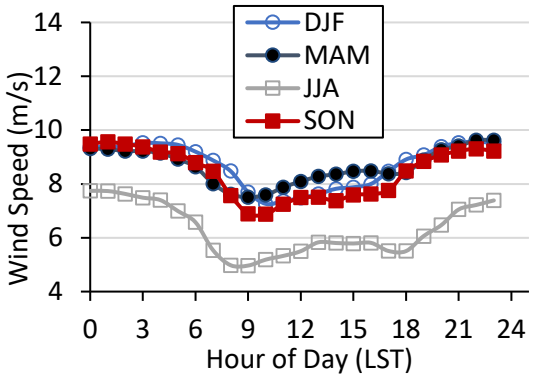

Figure 3-3. Diurnal variation of measured wind speed at Homestead

The power-law exponent determined between 50 m and 150 m varies as a function of time and is plotted in Figure 3-4 (Walton, Takle, & Gallus, 2014). In comparison to the actual power-law exponents, it is clearly see that the commonly used theoretical value of 1/7 does not adequately represent the diurnal variation occurring between 50 m and 150 m, which is the rotor layer for utility-scale wind turbines. The IEC Standard, labeled as a dotted line, suggests a higher value of 0.2 to represent the Normal Wind Profile (NWP) in Iowa, but it also fails to capture the actual distribution of the power-law exponent. The log-scale cumulative distribution presented in Figure 3-4(b) reflects the variation in the power-law exponent, which illustrates that using a single distribution function may not accurately fit the data (Smith et al., 2002). From the diurnal cycle plot in Figure 3-4(a), it is further seen that using a constant value significantly underestimates the power-law exponent at nighttime when the production is expected to be high and slightly overestimates it during daytime. The measured power-law exponent is in the range of 0.06 and 0.38, depending on the season and the hour. During the warm season (MAM, JJA), the variations of the power-law exponent are generally comparable to the cold season (DJF, SON), while the observed yearly nighttime exponents are generally three times higher than the daytime exponents. A power-law exponent higher than 0.2 during the nighttime, implying a higher wind shear condition,

which should be given consideration to minimize any operational challenges associated with the wind turbines (Kelley et al., 2004). Since nighttime hours have higher wind speeds and higher power-law exponent than during the day, calculating the wind power production over a short time interval is important to obtain accurate estimates of AEP.

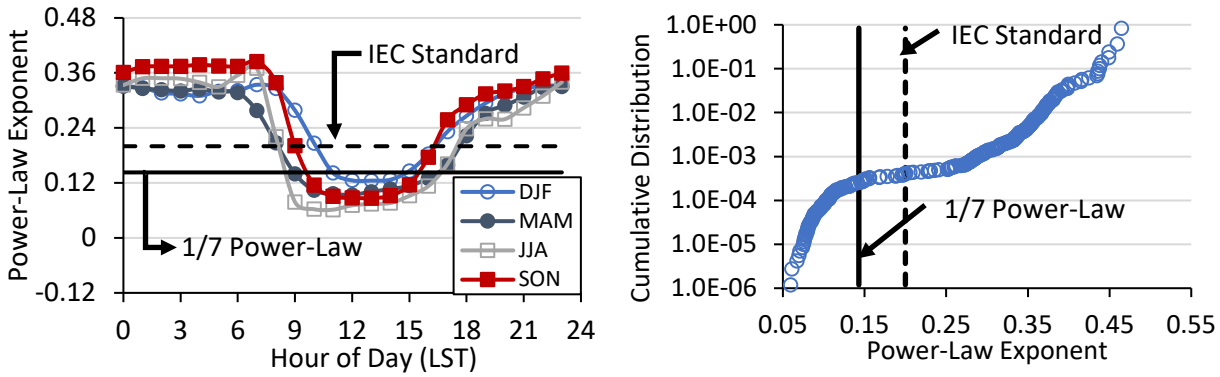

(a) Diurnal variation (b) Probability distribution

Figure 3-4. 50-150-m power-law exponent at Homestead from measured data

A comparison of the seasonal energy production is made between the calculated energy production and the observations from Midcontinent Independent System Operator (MISO) using data obtained over one year within the measurement duration (MISO, 2014). Data received from MISO provide an average energy production for wind generation in the entire MISO Midwest region, in which varying hub height of 55 to 100 m is used. To minimize the effect of varying hub height, the average hourly energy production is normalized by dividing it to the total energy production, and the result is presented in Figure 3-5(a). Also included in this figure is the normalized energy production (labeled as MET) obtained for Homestead using measured wind data. The normalized Homestead energy production shows more fluctuations than the MISO results which exhibit much flatter diurnal patterns. This difference in the normalized production is not unexpected for the following reasons: 1) the MISO energy production from wind is influenced by the market demand and

unexpected turbine curtailment in individual wind farms; 2) peak and off-the-peak hours of wind speeds may change with geographic locations of the wind farms; and 3) terrain condition and the hub height are variables in the MISO data. For this reason, the hourly energy production is averaged and reported in the figure as MET_ave at 4.1 percent. As can be seen, both averages compare closely, confirming a satisfactory comparison between the calculated AEP for Homestead and MISO wind energy production.

The two data sources are further analyzed for their normalized seasonal productions, as presented in Figure 3-5(b). Results for both MET and MISO normalized production demonstrate higher values during winter (DJF) and spring (MAM) and lower for summer (JJA) and fall (SON) seasons. A strong agreement in seasonal patterns between MET and MISO suggests that the AEP equation is a satisfactory model in providing annual energy production. Application of the AEP model has been adequate in not only calculating energy production but also representing seasonal variability, therefore making it a valuable tool for assessing case studies concerning other sites.

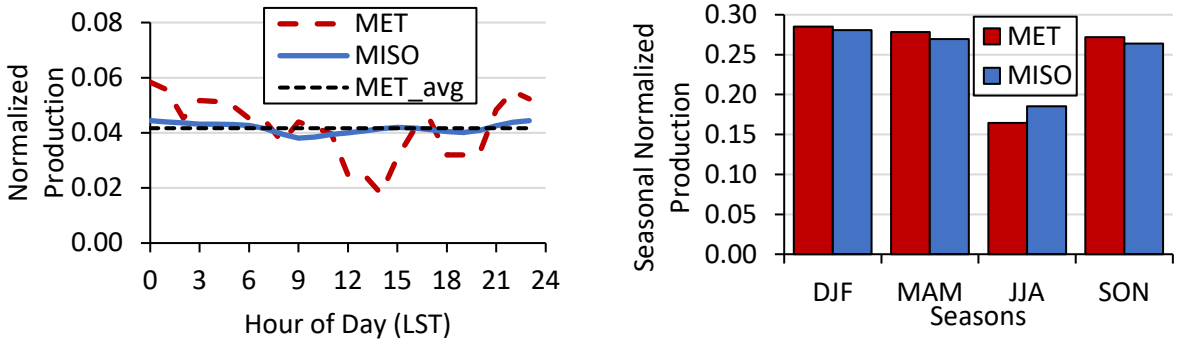

(a) Diurnal cycles (b) Seasonal cycles

Figure 3-5. Diurnal and seasonal cycles of the estimated normalized energy production from different data sources

3.6. Results

Using the AEP model described in the previous section, a parametric study is conducted for sites in Iowa and Minnesota. Specifically, wind data from the Iowa locations (i.e., Homestead, Altoona, Quimby, Mason City and Palmer) are three-year (12/2006-04/2009) datasets while the dataset from Eolos wind research site at Rosemount, MN, is for one-month (07/2004) duration.

3.6.1 Energy Production Assessment

As Figure 3-6 shows the value of α calculated for all six sites during summer months, which as expected, varies drastically from commonly assumed constant values. For the sites in IA, data from all three summer months over the height of 50 m – 150 m are used, whereas the MN data reflect the average α established for July using wind data over a 30 m – 130 m height range.

As seen in Figure 3-6, all sites generally exhibit comparable diurnal patterns for α. For IA sites, some variations in power-law exponents are seen, especially at night, while the MN site shows consistently higher exponents compared to IA sites. For all sites, the minimum power-law exponents are obtained during the daytime (i.e., 0600-1800 LST) with the peak near midnight or early morning hours. The observed trends of the diurnal patterns are found to support historical measurements reported for the Midwest (Walton, Takle, & Gallus, 2014; Kelley et al., 2004; Smith, 2002). The exponent values for all the curves range from 0.26 to 0.46 at night while they vary from 0.01 to 0.09 during the day. Data from these sites also demonstrate that the hourly average exponents are estimated at 0.248 for the data duration and consistently deviate from constant values of 1/7 and 0.2 as previously noted. To accurately estimate the AEP for all of these sites, the respective power-law exponents shown

in Figure 3-6 are updated using the entire data for each site and then used in the power estimation.

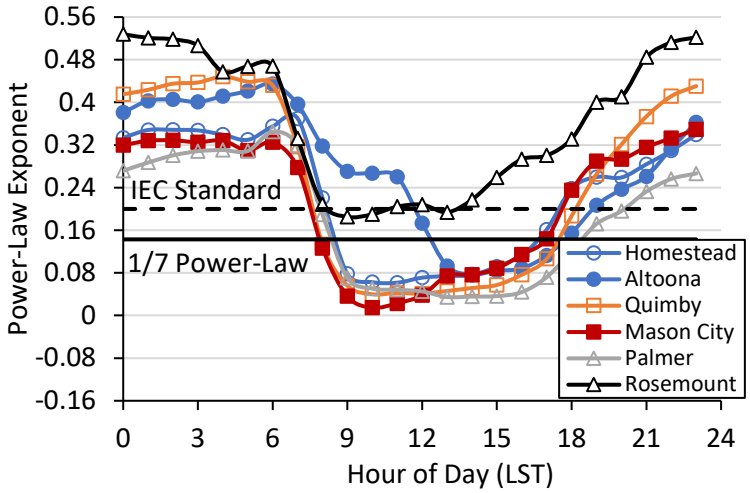

Figure 3-6. Diurnal variation of the power-law exponent from 50-150 m at multiple observed sites

Using the respective power-law exponent established for each site, wind speeds are computed for desired hub heights, namely 50 m, 80 m, 100 m, 120 m, and 140 m. Figure 3-7 demonstrates the variations in average hourly wind speeds calculated for the entire available durations at different hub heights (see Table 3-1 for durations). As expected, wind speed increases with height at all sites and the vertical gradient of wind speed becomes more pronounced as the hub height increases. A persistent diurnal variation is seen for wind speeds above 80 m at all locations, showing higher at night than during the day. However, at the relatively low elevation of 50 m, the highest wind speeds are observed during the mid-afternoon. As the sun rises during the day, the air near the surface ground becomes warmer and couples with the cooling air from the upper level, causing an opposite trend for the wind speed. The inversed diurnal variation at relatively low altitudes agree with the historical wind speed trend in the Midwest (Takle, Brown, & Davis, 1978; Storm et al., 2009; Walton, Takle, & Gallus, 2014; Kelley et al., 2004). Consistent with the lower power law seen before, the

variation in wind speed at different hub heights is insignificant during daytime (i.e., 0600-1800 LST). At Rosemount, the change in wind speed has a different trend and the corresponding magnitudes are slightly lower than the IA sites. This is partly due to using data from one summer month for this site.

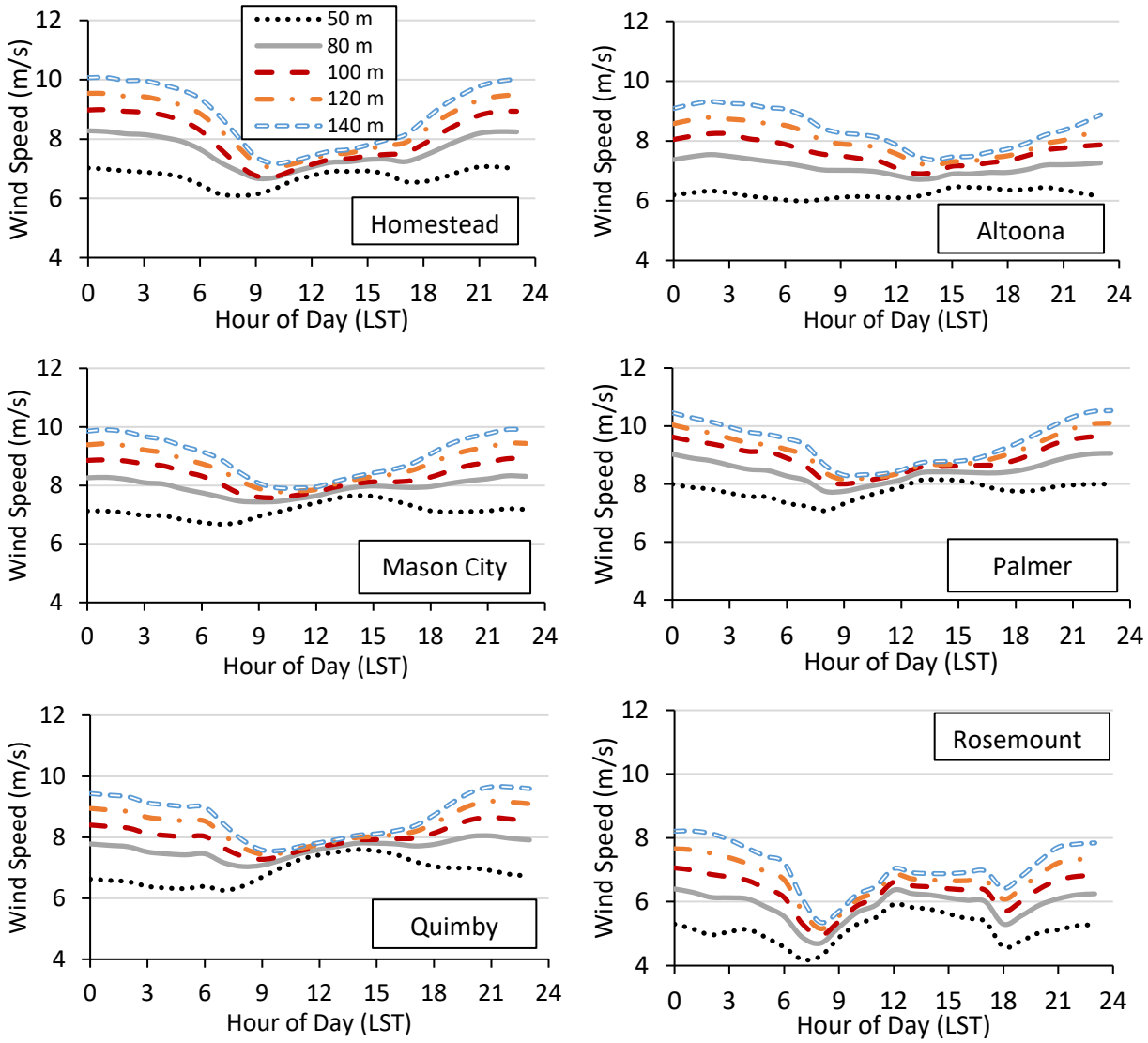

Figure 3-7. Diurnal variations of the annual average of wind speed at various heights

Using actual wind speeds obtained from wind farm sites and the appropriate power curves for the two turbines, the average annual energy productions are estimated for each site for the entire measurement period. Both the AEP and capacity factor are calculated in each

case. Figure 3-8 and Figure 3-9 present the capacity factor for each Iowa site as a function of hub height while Table 3-3 presents the average values for AEP and capacity factor obtained for all five sites. As seen in the figure and table, it is concluded that as the hub height increases, the averaged AEP of the observed sites at 100 m increases as much as 10 percent more than the average AEP at 80 m, which continues to be the typical height for turbines in the U.S. today. A similar increase is seen when the hub height increases from 100 m to 140 m, implying that the benefit in hub height increase is more significant for the first 20 m. This observation is confirmed in Figure 3-8 and Figure 3-9, which also shows that the capacity factor can be increased by as much as 25 percent in comparison to 80 m tall towers by simply elevating the hub height to 140 m. It is also seen that the benefit of tall towers varies depending on the location and therefore collecting wind data at the actual wind farm location is critical for realizing the optimal hub height for tall towers.

As the hub height increases, the capacity factors for both turbines increase significantly, reaching net capacity factors in the range of 48 to 52%. Although the production of a 3.2 MW turbine is higher than the 2.3 MW turbine due to its bigger turbine size and larger rotor diameter, the 2.3 MW turbine consistently produces higher capacity factors. This is due to the specific power of the 2.3 MW being lower than that of the 3.2 MW turbine. However, when the benefits of the two turbine sizes are compared with respect to the tower height, Table 3-3 shows that the percentage increase in capacity factor is moderately higher for 3.2 MW with taller towers. The combination of increased AEP and higher percentage increase in capacity will favor the large-size turbine with an appropriate power curve for tall tower applications. By utilizing a bigger rotor to reduce the specific power, increase in net capacity factors can also be realized for the 3.2 MW turbine.

Table 3-3. The AEP and capacity factor (CF) obtained by averaging the production from all five sites in Iowa

Height (m)	Average AEP 2.3 MW (MWh)	Average CF 2.3 MW (%)	Percent Change 2.3 MW	Average AEP 3.2 MW (MWh)	Average CF 3.2 MW (%)	Percent Change 3.2 MW
80	8.40×10^3	41.7		10.4×10^3	37.0	
100	9.18×10^3	45.5	9%*	11.5×10^3	40.9	10%*
120	9.45×10^3	46.9	13%*	11.9×10^3	42.6	15%*
140	9.82×10^3	48.7	17%*	12.5×10^3	44.6	20%*

*with respect to 80 m tower

Another observation from Figure 3-8(b) and Figure 3-9(b) is that the benefits of tall towers have site dependency in the percentage increase in capacity factor as the increased tower height produces relatively larger scatter. This observation again emphasizes that finding an optimal tower height using measured wind data for each localized region is important to fully realize the benefits of tall towers and minimize the LCOE. Moreover, it is clear that the lowest capacity factors for the two turbine configurations are between 33% and 37% at 80 m, which are higher than the average of 30.8% among all project samples built from 2004 to 2011 obtained for an NREL study. This improvement is impacted by the industry trend of higher hub heights and lower specific power. Particularly, 20 m taller than the conventional hub height of 80 m already contributes to a 9% increase in capacity factor for all sites, which provides significant growth in wind resource. This suggests that towers should be built to at least 100 m to achieve greater wind power production and make LCOEs more competitive.

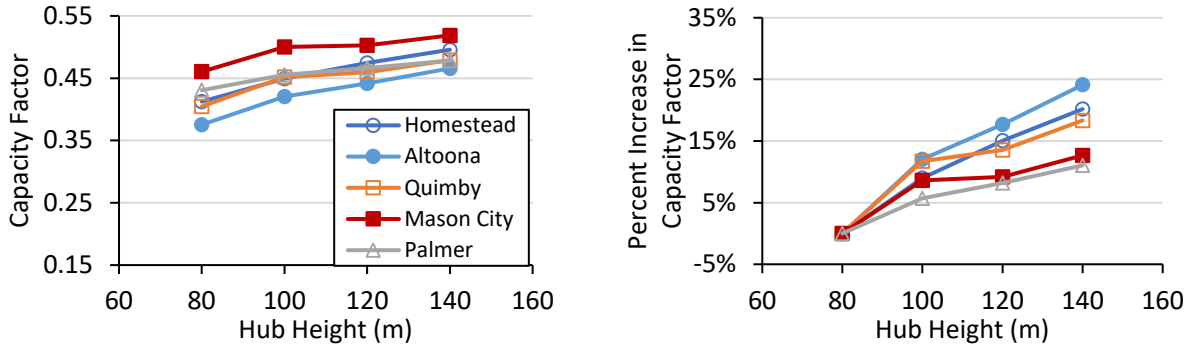

(a) Capacity factor (b) Percent increase in capacity factor

Figure 3-8. (a) Capacity factors and (b) their percentage increases for a 2.3 MW turbine at hub heights in Iowa sites

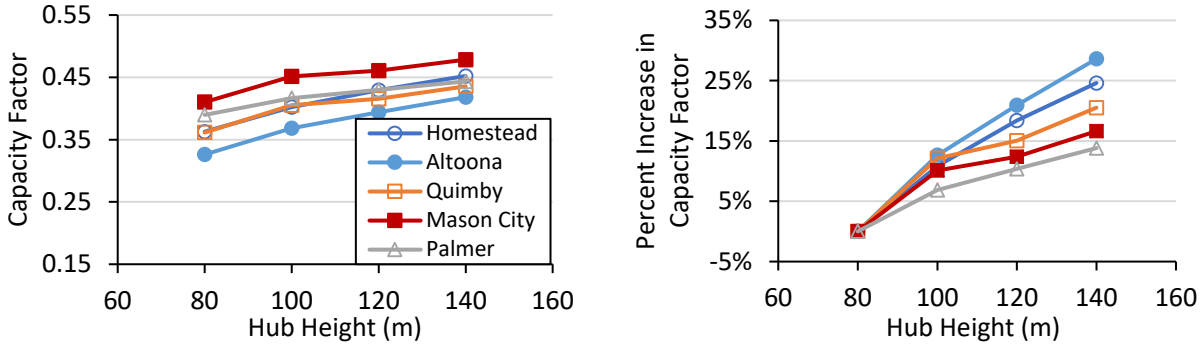

(a) Capacity factor (b) Percent increase in capacity factor

Figure 3-9. (a) Capacity factors and (b) their percentage increases for a 3.2 MW turbine at hub heights in Iowa sites

Since the recorded period for Rosemount is short, the relationship between the capacity factor and hub height for this site is plotted separately in Figure 3-10 with respect to the 2.3 MW and 2.5 MW turbine. Compared to the average summer (JJA) values of capacity factor in Iowa, Rosemount shows a similar upward increasing trend with hub height and the capacity factors in July are within 10% difference from the Iowa average values for a 2.3 MW turbine. The capacity factors for a 2.5 MW turbine are lower than the values for the 2.3 MW turbine, which is driven by the decline in turbine specific power, suggesting that estimating the wind energy production for elevated hub heights is greatly helpful for turbine and tower height selection.

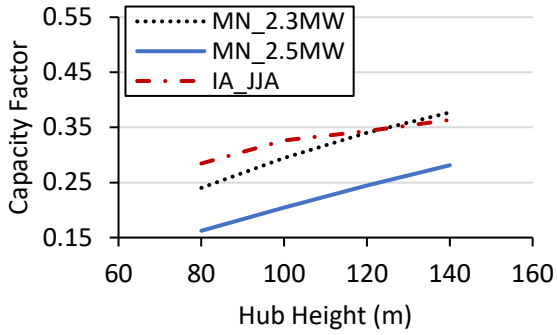

Figure 3-10. Capacity factors for Rosemount in July and the average capacity factors for IA sites in summer (JJA) at different hub heights

3.6.2 Case Study using WIND Toolkit Data

Since measured wind data are not readily available for broader regions at elevated heights, this section examines the possibility of using the WIND Toolkit (Draxl et al., 2015) to estimate the wind speeds and evaluate the AEP at higher hub heights. The Techno-Economic WIND Toolkit provides data for the entire U.S. at 120,000 locations. This WIND Toolkit contains 7-year data at 5 minute interval at 100-m elevations. To examine the quality of the data, diurnal and seasonal variations for wind speeds at Homestead are first examined and compare them to those obtained from measured wind data. The WIND Toolkit site chosen for this comparison is located within 2 miles of the Homestead site. As shown in Figure 3-11(a), similar to the wind measurements obtained from the meteorological tower at 100 m, the maximum wind speed from the WIND Toolkit occurs at night and the minimum wind speed is experienced after sunrise. Additionally, the diurnal and seasonal variations obtained from the simulated wind data show similar trends to those obtained from the wind measurements. However, the seasonal averages of daytime (DT [0600 – 1800 LST]) and nighttime (NT [1800 –0600 LST]) wind speeds from the WIND Toolkit slightly underestimate the actual average values (Figure 3-11(b)). This observation suggests that

calculating the energy production using the WIND Toolkit would yield conservative results, but the difference between the Toolkit data and tower measurements would be minimal for the energy production estimates.

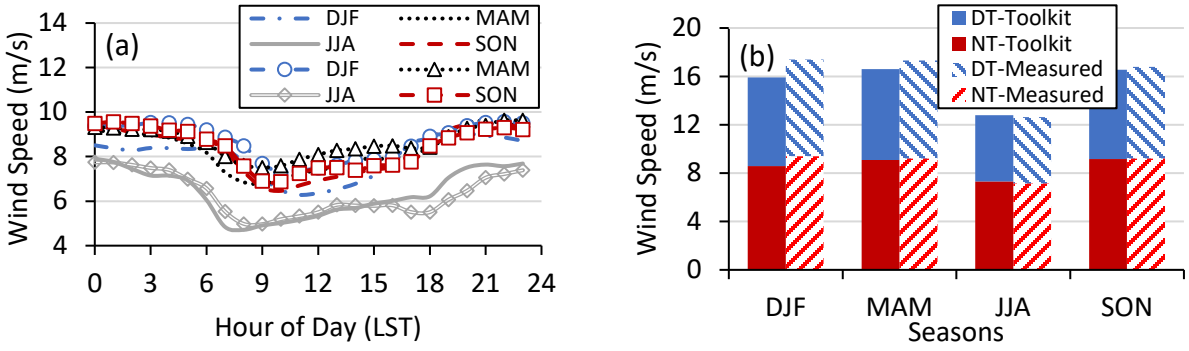

Figure 3-11. (a) Diurnal and seasonal variations of wind speed and (b) seasonal averages of daytime (DT) and nighttime (NT) wind speed at Homestead from WIND Toolkit (lines) and observations (lines with markers)

Next, the daytime (DT [0600 – 1800 LST]) and nighttime (NT [1800 –0600 LST]) wind roses at a 100 m height in Homestead are analyzed for each wind data source and their respective seasons, as displayed in Figure 3-12. The seasonal and diurnal patterns from the measured data agree well with earlier findings that confirm wind speeds during daytime are likely to be lower than the nighttime values for all seasons, and the maximum wind speed usually occurs during nighttime hours (Walton, Takle, & Gallus, 2014; Kelley et al., 2004). Results from the WIND Toolkit show a good agreement with tower measurements for all seasons, but exhibit lower speed for northwest winds during the daytime and nighttime hours in winter, as shown in Figure 3-12 and Figure 3-11.

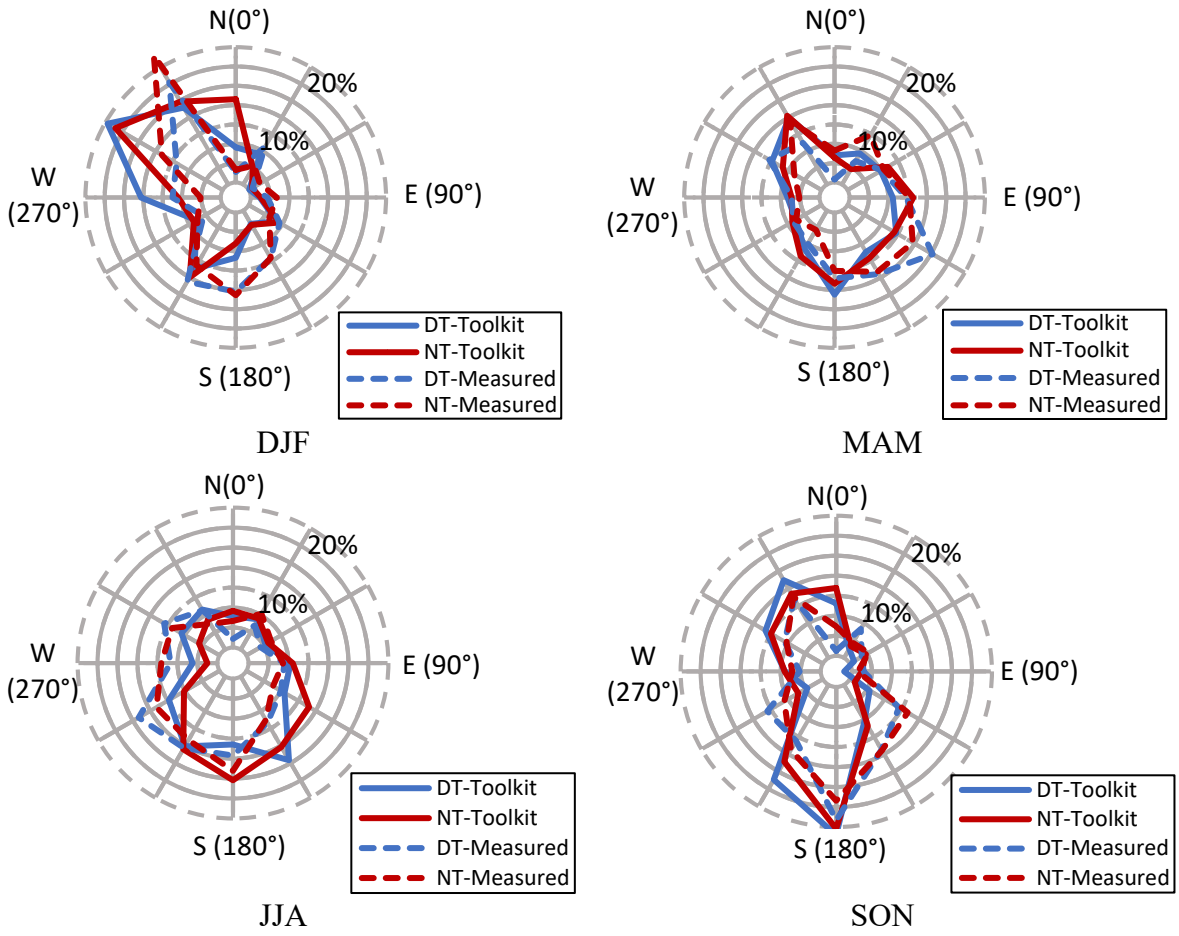

Figure 3-12. Wind rose of wind speed for Homestead from WIND Toolkit and Measured data

To examine the reliability of using the Toolkit in estimating AEP, Figure 3-13 compares the daytime (DT) and nighttime (NT) energy production between the measured data and WIND Toolkit data by using the actual power-law exponent calculated from wind speeds at 50 m and 150 m and the constant value of 1/7 for power law. For the Siemens 2.3 MW turbine model, the increments in two types of energy productions that use measured power law show similar trends for both the field and simulated data, while for the energy productions calculated from the constant power law show a slower increase with the hub height during the day. This difference is impacted by diurnal variations of power-law exponent captured in Figure 3-4. With this analysis, using daytime wind data from WIND

Toolkit will underestimate the annual energy production. This inadequate estimate can be influenced by the low wind speeds modeled by the WIND Toolkit, as was discussed at the beginning of section 3.6.2. Similar conclusions can also be made for the Siemens 3.2 MW turbine model. The total annual energy production that uses measured power law exponent for the measured data and WIND Toolkit data are summarized in Table 3-4, which shows that the AEP prediction from WIND Toolkit yields less than 8% conservative results.

Table 3-4. Comparison of annual energy production and net capacity factor for Homestead at 100 m

Parameters	NREL WIND Toolkit	Met-Tower Data	NREL WIND Toolkit	Met-Tower Data
Tower hub height, m	100	100	100	100
Turbine size, kW	2300	2300	3200	3200
Design life, years	20	20	20	20
Wind speed at 50 m height, m/s	6.51	6.72 (+3%)	6.51	6.72 (+3%)
Average power law α	0.248	0.248	0.248	0.248
Altitude above sea level, m	450	450	450	450
Air density at 80 m height, kg/m^3	1.163	1.163	1.163	1.163
Cut-in wind speed, m/s	3	3	3	3
Cut-out wind speed, m/s	25	25	25	25
Annual energy production, MWh/year	8,433	9,056 (+7.4%)	10,479	11,274 (+7.6%)
Net capacity factor (%)	41.9	44.9 (+7.4%)	37.4	40.2 (+7.6%)

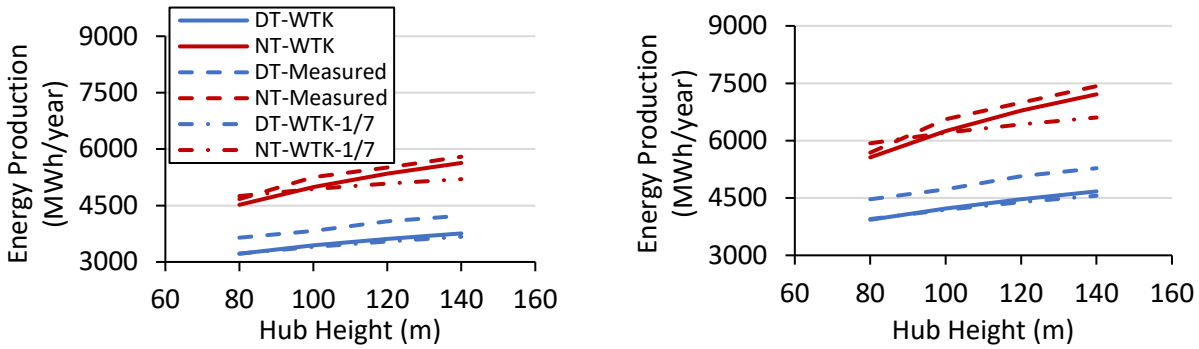

(a) Energy Production for a 2.3 MW turbine (b) Energy Production for a 3.2 MW turbine

Figure 3-13. Comparison of daytime (DT) and nighttime (NT) energy production between measured data and WIND Toolkit (WTK) data using measured and 1/7 power-law exponents

3.7. Conclusions

Unique wind observations with sufficient quality from the states in the wind-rich region (i.e., Iowa and Minnesota) serve to evaluate the energy production and realize the benefits of tall towers by using an estimate model to determine annual energy production and capacity factor. Although the wind condition in these areas is suitable to produce power at a turbine height of 80 m, there is a significant increase in energy production gained from tall towers. The subsequent cost estimate of using a tall tower technology (e.g., Hexcrete Tower) can be lower than the conventional steel option. Therefore, the optimum turbine height for wind projects in this region is worthwhile to reconsider and the paper provides insights into better understanding the benefits of developing tall towers. This study began with the validation of the AEP estimate model by comparing the normalized energy production calculated from the model with historical records. Wind characteristics are then investigated for all six sites in Iowa and Minnesota, providing actual variations of wind speed, wind direction and power-law exponent for estimating AEP. Using the validated model, AEP and capacity factor are calculated for different desired hub heights regarding the two chosen turbine model. Similar assessment of wind characteristics and energy production is

undertaken by using the 100-m dataset from Techno-Economic WIND Toolkit for Homestead, IA. The following conclusions can be drawn from this study:

- A similar diurnal variation of wind speed is seen consistently at the chosen sites for different seasons and tower heights, showing consistently higher wind speeds at night than during the day. With increased hub heights, nighttime wind speeds increase significantly while a minimal change in wind speed is found during the day.
- In contrast to a theoretical constant value, wind data in Iowa and Minnesota sites featured significant variations of the power-law exponent as a function of time and the annual averages for each chosen site. These values averaged to about 1/4 as oppose to a routinely used value of 1/7 assumption. To obtain realistic estimates, it is important to incorporate a power-law exponent as a function of time in the AEP calculations.
- The calculation model for estimating AEP is validated using measured wind data and varied power-law exponents and produced satisfactory results of energy production for a day and four seasons when compared to MISO records. Although MISO records presented more stable diurnal cycles of energy production than the measured data, the difference of annual averages between the two sources is minimal, indicating that the AEP calculation as adopted in this study is suitable for assessing wind energy production.
- The energy production potentials generally show an increase of more than 9 percent in AEP and capacity factor with a 20-m increase in hub height, indicating that there is an advantage to raise turbine height by at least 20 m. More promising wind power potential is expected for towers taller than 100 m, recommending that it can be

feasible to use 100-plus m tall towers in the wind-rich regions to obtain optimal wind energy production.

- Simulated data from WIND Toolkit are also used to estimate AEP and capacity factor for areas where limited or no field measurements are available. Wind data from the Toolkit are first examined for accuracy with the actual measurements and showed a good representation of the variation of the actual wind speed and direction at 100 m with lower estimates in wind speed, indicating a lower estimate for energy production.
- A less than 8% difference in energy production estimate is reflected between the simulated data from the WIND Toolkit and the field measurements when the actual power-law exponent is used. However, the percentage increases up to 12% for 140-m wind towers if using the constant value of power-law exponent in the estimate, indicating that obtaining the power-law exponent from the actual wind project site or nearby available locations is critical to predict wind power potentials at elevated heights.

3.8. Acknowledgements

This study was partially funded by the Office of Energy Efficiency and Renewable Energy of the U.S. Department of Energy under Award No. DE-EE0006737. The first author was supported by a Ph.D. scholarship from the Chinese Scholarship Council based in Beijing. The authors are very grateful to the Iowa Energy Center for providing the wind resource data in Iowa and Eolos Wind Research Station at the University of Minnesota for providing additional wind data measurements.

3.9. References

American Wind Energy Association. (2019).U.S. *Wind Industry Annual Market Report: Year Ending 2018.* American Wind Energy Association: Washington, D.C., USA.

AWS Truepower, Inc. (2010). *Final Report: Iowa Tall Tower Wind Assessment Project - Iowa State University.* Iowa Energy Center.

Barutha, P., Nahvi, A., Cai, B., Jeong, H. D., and Sritharan, S. (2019). Evaluating Commercial Feasibility of A New Tall Wind Tower Design Concept Using A Stochastic Levelized Cost of Energy Model. J*ournal of Cleaner Production,* 240: 118001.

Celik, A. N. (2004). A Statistical Analysis of Wind Power Density Based on the Weibull and Rayleigh Models at the Southern Region of Turkey. *Renew Energy*, 29:593–604. doi:10.1016/ j.renene.2003.07.002

Cotrell, J., Stehly, T., Johnson, J., Roberts, J. O., Parker, Z., Scott, G., et al. (2014). *Analysis of Transportation and Logistics Challenges Affecting the Deployment of Larger Wind Turbines: Summary of Results*. NREL/TP-5000-61063. National Renewable Energy Laboratory: Golden, CO, USA.

Davenport, A. G. (1961). The Spectrum of Horizontal Gustiness Near the Ground in High Winds. *Q J R Meteorol Soc*, 87:194–211. doi:10.1002/qj.49708737208

Deaves, D. M., and Lines, I. G. (1997). On the Fitting of Low Mean Windspeed Data to the Weibull Distribution. *J Wind Eng Ind Aerodyn,* 66:169–178. doi:10.1016/S0167-6105(97) 00013-5

Draxl, C., Clifton, A., Hodge, B. M., McCaa, J. (2015). The Wind Integration National Dataset (WIND) Toolkit. *Appl Energy*, 151:355–366. doi:10.1016/j.apenergy.2015.03.121

Engström, S., Lyrner, T., Hassanzadeh, M., Stalin, T., and Johansson, J. (2010). *Tall Towers for Wind Turbines, Report from Vindforsk Project V-342 Höga Torn För Vindkraftverk Elforsk Rapport* 10:48.

García-Bustamante, E., González-Rouco, J. F., Jiménez, P. .A, Navarro, J., and Montávez, J. P. (2008). The Influence of the Weibull Assumption in Monthly Wind Energy Estimation. *Wind Energy*, 11:483–502. doi:10.1002/we.270

Hennessey, J. P. Jr. (1977). Some Aspects of Wind Power Statistics. *J Appl Meteorol*, 16:119–128. doi:10.1175/1520-0450(1977)016<0119:SAOWPS>2.0.CO;2

International Electrotechnical Commission (IEC). (2005). *IEC 61400-1: Wind Turbines – Part I: Design Requirements.* 3rd PPUB ed. International Electrotechnical Commission (IEC): Geneva, Switzerland.

Kelley, N., Shirazi, M., Jager, D., Wilde, S., Patton, E. G., and Sullivan, P. (2004). Lamar Low-Level Jet Project Interim Report. NREL/TP-500-34593. National Renewable Energy Laboratory: Golden, CO, USA.

King, J., Clifton, A., Hodge, B. M. (2014). *Validation of Power Output for the WIND Toolkit*. NREL/TP-5D00-61714. National Renewable Energy Laboratory: Golden, CO, USA.

Krohn, S., Morthorst, P., and Awerbuch, S. (2009). *The Economics of Wind Energy*. European Wind Energy Association: Brussels, Belgium.

Lantz E, Wiser R, Hand M, Arapogianni A, Ceña A, Simonot E, et al. (2012). *IEA Wind Task 26: The Past and Future Cost of Wind Energy, Work Package 2.* National Renewable Energy Laboratory: Golden, CO, USA.

Lantz, E., Roberts, O., Nunemaker, J., DeMeo, E., Dykes, K., and Scott, G. (2019). *Increasing Wind Turbine Tower Heights: Opportunities and Challenges.* NREL/TP-5000-73629. National Renewable Energy Laboratory: Golden, CO, USA.

Lewin, T., and Sritharan, S. (2010). Design of 328-ft (100-m) *Tall Wind Turbine Towers Using UHPC,* ISU-ERI-Ames Report ERI-ERI-10336. Ames, Iowa.

List, R. J. (1951). Smithsonian Miscellaneous Collections: *Smithsonian Meteorological Tables.* vol. 114. Sixth Revi. Smithsonian Institution Press: Washington, D.C., USA.

Meeker, W. Q., and Escobar, L. A. (1998). *Maximum Likelihood: Log-location-Scale Based Distributions.* Stat. Methods Reliab. Data, John Wiley & Sons, p. 135–172.

Midcontinent Independent System Operator (MISO), Inc. (2014). Archived Historical Hourly Wind Data. https://www.misoenergy.org/markets-and-operations/real-time--market-data/market-reports/#nt=/MarketReportType:Summary/MarketReportName:Historical%20Hourly%20Wind%20Data%20(csv) Accessed April 8, 2018.

Moné, C., Hand, M., Maples, B., and Smith, A. (2015). *2013 Cost of Wind Energy Review.* NREL/TP-5000-63267. National Renewable Energy Laboratory: Golden, CO, USA.

Petersen, E. L., Mortensen, N. G., Landberg, L., Højstrup, J., and Frank, H. P. (1998). Wind Power Meteorology. Part I: Climate and Turbulence. *Wind Energy,* 1:2–22. doi:10.1002/(SICI)1099-1824(199809)1:1<2::AID-WE15>3.0.CO;2-Y

Redburn, R. (2007). A Tall Tower Wind Investigation of Northwest Missouri. MS Thesis, University of Missouri.

Schwartz, M., and Elliott, D. (2005). Towards a Wind Energy Climatology at Advanced Turbine Hub-Heights NREL/CP-500-38109. *15th Conf. Appl. Climatol.*, American Meteorological Society: Savannah, GA, USA. pp:1–11.

Showers, D. (2014). System Identification for the Clipper Liberty C96 Wind Turbine. MS Thesis, University of Minnesota.

Smith, K., Randall, G., Malcolm, D., Kelley, N., and Smith, B. (2002). Evaluation of Wind Shear Patterns at Midwest Wind Energy Facilities. P*roc. American Wind Energy Association (AWEA) WINDPOWER*. AWEA: Portland, Oregon, USA.

Sritharan, S. (2015). Wind Turbine Towers: Precast Concrete Hexcrete May Help Increase Renewable Energy Capacity with Taller Hub Heights. *PCI Journal*; 60:33–38.

Sritharan, S. (2016). Hexcrete Tower for Harvesting Wind Energy at Taller Hub Heights - Budget Period 2. Ames, Iowa. doi:10.2172/1361022

Storm, B., Dudhia, J., Basu, S., Swift, A., and Giammanco, I. (2009). Evaluation of the Weather Research and Forecasting Model on Forecasting Low-Level Jets: Implications for Wind Energy. *Wind Energy*,12:81–90. doi:10.1002/we.288

Studylib. (n.d.). The New Productivity Benchwork: Siemens Wind Turbine SWT-2.3-108. Siemens Market-Specific Solution. https://studylib.net/doc/10458843/the-new-productivity -benchmark-siemens-wind-turbine-swt-2... Accessed July 18, 2017.

Takle, E. S., Brown, J. M., and Davis, W. M. (1978). Characteristics of Wind and Wind Energy in Iowa. *Iowa State J Res*,52:313–339.

U.S. Department of Energy (DOE). (2014). *WINDExchange: Wind Potential Capacity.* U.S. Department of Energy. https://windexchange.energy.gov/maps-data?category=potential Accessed June 21, 2017.

U.S. Department of Energy. (2015). *Enabling Wind Power Nationwide.* U.S. Department of Energy, Office of Energy Efficiency and Renewable Energy: Washington, D.C., USA.

U.S. Department of Energy (DOE). (2015). *Wind Vision: A New Era for Wind Power in the United States*. DOE/GO-102015-4557. U.S. Department of Energy (DOE): Washington, D.C, USA.

U.S. Department of Energy (DOE). (2019). *Annual Energy Outlook 2019.* U.S. Department of Energy (DOE): Washington, D.C., USA.

Walton, R. A., Takle, E. S., and Gallus, W. A. (2014). Characteristics of 50-200-m Winds and Temperatures Derived from an Iowa Tall-Tower Network. *J Appl Meteorol Climatol,*53:2387–93. doi:10.1175/JAMC-D-13-0340.1

Wind-turbine-models.com. (n.d.). Siemens SWT-3.2-113 Power Curve. https://en.wind-turbine-models.com/turbines/966-siemens-swt-3.2-113#datasheet Accessed July 18, 2017.

Wiser, R., Bolinger, M., Barbose, G., Darghouth, N., Hoen, B., Mills, A., et al. (2019). *2018 Wind Technologies Market Report.* DOE/GO- 102019-5191. U.S. Department of Energy (DOE): Washington, D.C., USA.

CHAPTER 4. QUANTIFYING THE BENEFITS OF TALL WIND TURBINE TOWERS IN THE U.S. WIND-RICH REGIONS

A paper to be submitted to the Wind Energy journal

Bin Cai[1], Sri Sritharan[1], Eugene S. Takle[2], and Chris Milliren[3]

[1] *Department of Civil, Construction, and Environmental Engineering, Iowa State University, Ames, IA 50011, USA*

[2] *Department of Geological and Atmospheric Science, Iowa State University, Ames, IA 50011, USA*

[3] *St. Anthony Falls Laboratory, University of Minnesota, Minneapolis, MN 55414, USA*

4.1. Abstract

The current wind turbine towers in the U.S. are commonly built at the hub height between 80 m and 90 m due to the transportation challenges, while towers taller than 100 m have been consistently growing in Europe for wind power generation. With continued tower technology development, tall towers are expected to drive wind energy production enhancement and further reduce the cost, which highlights the need for precise estimation in annual energy production (AEP) and cost savings. However, due to the lack of reliable wind resource information at elevated hub heights, the value of reaching higher heights has not been fully quantified. To assess the benefits of tall towers, this study begins by validating an early-studied AEP calculation model for the actual wind measurements up to 130 m and power generation data from one turbine at a test site near Minneapolis, MN. Comparable results are found in the hourly and monthly cycles of the energy productions among these data sources, indicating that this AEP model is suitable for estimating wind energy production at elevated hub heights. The AEP increase and the resultant potential revenue are then estimated for other new heights, which shows a pronounced growth for taller towers throughout the entire duration, specifically when an intense electric load is observed in the region. To assess the potential opportunity offered by increased hub height in the wind-rich

regions, simulated wind data up to 200 m obtained from the National Renewable Energy Laboratory (NREL) are applied to the AEP model. Analysis results demonstrate that with a 20-m hub height increase from the current practice, the average energy production for all sites increases by 11%, which agrees with early findings in Iowa. Resultant AEP results are then used to quantify the cost benefits of higher hub height, which helps determine the optimal heights for developing taller towers in this region.

KEYWORDS

tall tower; annual energy production; levelized cost of energy; wind measurements; power generation

4.2. Introduction

The worldwide interest of utilizing tall wind turbines in the power supply has accelerated in the past decade as an increasing number of tall towers are being made to support turbines to harness more power from the stronger winds. However, it is not always easy and financially benefitial to increase the tower height from 80 m in that tubular steel towers that dominate the wind industry today are limited in height due to transportation constraints in the United States (U.S. Department of Energy (DOE), 2017; Lantz et al., 2012). Currently, a majority of tubular steel towers in the U.S. is designed with a maximum diameter of 4.3 m for shipping under bridges on the existing highway system (DOE, 2015; Cotrell et al., 2014). This means that developing tall steel towers, which requires larger base diameters or thicker steel plates to form a higher strength structure, creates transportation challenges and thus increases the overall cost of wind energy – Levelized Cost of Energy (LCOE). Increased LCOE will eventually make wind energy less competitive to other power generating technologies, which puts a high uncertainty to achieve the wind generation scenarios suggested by the DOE (DOE, 2015).

Although tall wind towers have limited deployment in the United States, 100-plus m wind towers have been widely built and operated in European countries. Wind towers taller than 120 m with larger turbines have already been used in Germany to supply power generation by implementing the lattice steel tower concept or mixing a concrete base with a conventional steel tower on top (Engström et al., 2010). Due to the land area constraints, these two tower designs with increased hub height and turbine capacity in Germany resulted in higher cost of energy compared to the United States (Hand, 2018; LaNier, 2005). Since design conditions in Germany are different from those in the U.S., an innovative design of wind towers with considerations of design optimals is desirable for wind energy development in the nation. Additionally, wind industry in Germany and Latin America have been seeking full concrete options for wind turbine towers with hub heights above 130 m by using large precast concrete shells with a maximum height of 20 m (Sun & Wind Energy, 2012; Concrete Plant International, 2016; Jimeno, 2012). However, this technology utilizes curved concrete segments to form tower sections, which requires a large amount of specialized formwork to match different section dimensions along the tower height, and therefore would significantly increase the total capital cost. As a result, a newly-developed tall tower technology – Hexcrete tower - is expected to lower the LCOE for wind energy without triggering transportation challenges. The Hexcrete tower sections comprise of six hexogonal-shaped concrete columns and six rectangular and/or tapered concrete panels (see Figure 4-1). All concrete components are designed in sizes that are suitable to transport without being constrained by the current highway system (Lewin & Sritharan, 2010; Sritharan, 2015). It was suggested that using this novel concrete tower technology, tower heights for new installations are able to increase to 140 m and the LCOE of wind energy production can

potentially decrease by nearly 6% compared to the steel tower design at the same height (Sritharan, 2017). In addition to the cost savings from applying the Hexcrete tower technology to tall towers, enabling deployment of wind turbines at greater altitudes will open up new land areas to develop wind power in all but the most wind-rich regions of the United States, which includes areas from the Midwest, Plains, and Texas (DOE, 2014, n.d.; American Wind Energy Association (AWEA), 2017). With continued technological developments focusing on improving tower heights, the gross land area from the wind-rich regions is estimated to grow 67% for a turbine at 140 m with a minimum net capacity factor of 30%, greatly expanding the potential areas for developing wind energy (DOE, 2015).

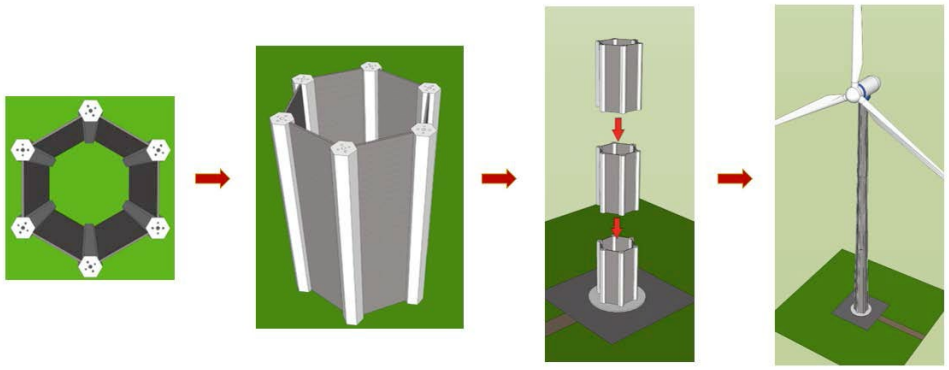

Figure 4-1. Hexcrete tower technology concept

It has been realized that realistic estimates of the growth in annual energy production (AEP) with increased hub height is essential to understand the economic benefits of developing tall towers (Wiser et al., 2016; Moné et al., 2016). Although the AEP estimate procedure has been examined with the aggregated wind data collected from the Midcontinent Independent System Operator (MISO), the AEP results have not been fully validated with power generation data from the same wind plant. Moreover, there are uncertainties to measure the impact of increased hub heights on the financial gain to the power generation sellers. This is due to: a) the absence of accurate and reliable wind observations at high

elevations since the commonly used method to record data in the field is to set up meteorology towers, which requires sufficient financial support and expert monitoring assistance, causing difficulties to accurately characterize atmosphere conditions in the rotor layer, such as wind speed profile, wind direction, and air density at the desired heights; b) lack of comprehensive power validation using calculated results from meteorology tower data and the actual wind generation data because of limited access to the power generation data that are obtained from a nearby wind turbine; and c) regional power prices are sensitive to the market share of each power source and not always available because of power policy issues, particularly outside of the wholesale electricity market.

Because of the aforementioned issues related to the data uncertainty at high elevations, it is important to use reliable wind observations from the project sites to make realistic wind energy estimates, which in turn helps determine the economic benefits for tall towers. This paper applies actual measurements from Minnesota, which comprises meteorological data up to 130 m and real-time power data from a 2.5 MW Clipper Liberty turbine at the hub height of 80 m, to the early-studied AEP calculation model for further examination of its accuracy in the hourly wind energy assessment (Cai et al., in review). With considerations of market power price, the economic performance of powering from tall towers is then compared with those from 80-m towers. Besides, the corresponding monthly variation is obtained to characterize the dependence of the predicted benefits on time. Furthermore, to broaden the estimation of wind energy growth in the wind-rich regions, sets of modeled wind data from levels at the ground surface up to 200 m are chosen from the state of Iowa, Minnesota, and Texas, to anticipate the AEP for wind projects in these areas. Finally, LCOE estimation are performed on the same chosen sites to quantify the cost

reduction as the hub height increases and suggest the optimal range of hub height for different turbine sizes..

4.3. Data Description and Processing

4.3.1. On-Site Wind Measurements in Rosemount, MN

Field measurements collected from the Eolos Wind Research Station in Rosemount, MN include a yearlong wind dataset in 2013 from a 130-m meteorological tower and an actual power generation dataset in the same period from an operating wind turbine at 80 m, which is located 160 m north of the observed meteorological tower. Wind data discussed in this paper were obtained from an instrumented tall tower by cup anemometers and wind vanes at six levels, namely 7.3 m, 27.1 m, 51.5 m, 76.7 m, 101.5 m, and 125.9 m. In addition, four three-dimensional sonic anemometers were also installed at the height of 9.9 m, 29.6 m, 79.1 m, and 127.9 m to represent the boundaries of rotor layer and the height from the ground to the mid-span of the blades. Detailed instrumentations of this measuring tower is described in Stone (2017). During the observation period, wind data were available at every one minute, including wind speed and direction, temperature, and humidity at all levels and barometric pressure at the hub height of 80 m. This paper uses the actual power information that were monitored from a Clipper Liberty 2.5 MW wind turbine with a rotor diameter of 96 m and hub height of 80 m. Real-time power generation and power curtailment data were also accessible by the turbine's Supervisory Control and Data Acquisition System (SCADA) throughout the entire year of 2013. All available measurements were recorded at every one minute, providing a set of high-resolution field data for power validation analysis.

Before estimating and validating the wind energy production at the hub height, both the measured wind and power generation data are filtered based on different conditions. Wind data are not included in the energy production calculation if the values are NaN, -999,

or remain constant for a long duration, which indicates that the measuring sensor might not be in a normal working state due to events such as icing and high precipitation. The corresponding data availability for wind speed data is summarized in Table 4-1. Data availability of wind speed in Rosemount, MN. Similar data filtering was carried out for the power generation data in the same period. Power data obtained from the wind turbine in Rosemount are replaced by "NaN" if 1) data are missing; 2) the turbine operating limit is observed to be less than 2500 kW; and 3) the turbine running index is recorded less than one which indicates that the wind turbine was operating with a noticeable energy curtailment and thus using the power curve for corresponding turbines would not accurately predict the power generation in the energy production calculation. This data filtering method leads to an absence of power data for June and October through December. Data availability for other months is listed in Table 4-2. It was noted that July would not be applied in the analysis of energy production due to the insufficient information observed in the power data series.

Table 4-1. Data availability of wind speed in Rosemount, MN

Availability	Jan	Feb	Mar	Apr	May	Jul	Aug	Sep
7.3 m	100.0%	100.0%	100.0%	100.0%	100.0%	100.0%	71.3%	99.6%
27.1 m	100.0%	100.0%	100.0%	100.0%	100.0%	100.0%	71.3%	99.6%
51.5 m	100.0%	100.0%	100.0%	100.0%	100.0%	100.0%	71.3%	99.6%
76.7 m	100.0%	100.0%	100.0%	100.0%	100.0%	100.0%	100.0%	100.0%
101.5 m	99.9%	100.0%	100.0%	99.9%	100.0%	100.0%	100.0%	100.0%
125.9 m	100.0%	100.0%	100.0%	100.0%	100.0%	100.0%	100.0%	100.0%
9.9 m	96.7%	96.9%	99.3%	97.7%	99.2%	100.0%	71.3%	99.3%
29.6 m	91.5%	98.1%	97.2%	91.3%	92.0%	100.0%	71.3%	99.4%
79.1 m	84.7%	98.3%	95.5%	85.8%	91.6%	100.0%	99.0%	99.4%
127.9 m	85.6%	95.5%	92.6%	79.6%	91.1%	100.0%	80.3%	69.6%

Table 4-2. Data availability of power generation for the observed 2.5 MW Clipper wind turbine

Month	Jan	Feb	Mar	Apr	May	Jul	Aug	Sep
Availability	25.5%	67.1%	82.8%	62.9%	41.7%	1.7%	65.3%	15.6%

To consider the impact of dry and moist air environment on the turbine production efficiency, the air density at the hub height is corrected by converting the measured air temperature to virtual temperature using the ratio of water vapor to dry air (List, 1968). For this reason, air density value plugged in the energy production calculation is a function of pressure, adjusted air temperature, and relative humidity, and the expression can be written as

$$\text{Air density} = \frac{\text{Air pressure}}{\text{Gas constant for dry air} \times \text{Virtual temperature}} \quad (4\text{-}1)$$

From Equation (4-1), the hydrostatic equation can also be written by replacing the air temperature obtained from the measuring sensor by the virtual temperature, providing a more precise reference to calculate air pressure and density at heights other than the hub height.

Potential power generation at all discussed sites in this study is estimated based on two wind turbine configurations from the Siemens utility-scale turbine series: 2.3 MW turbine with a 108 m rotor diameter and 3.2 MW turbine with a 113 m rotor diameter. General characteristics of the turbines are detailed in the Siemens technical reports (Siemens market-specific solution, n.d.; Wind-turbine-models.com, n.d.).

4.3.2. Quality Insurance for the Field Measurements

To testify the quality of the measured dataset in the Eolos Wind Station, wind speed and direction, as well as air pressure are compared with observations from a nearby standard climate station. The 1-minute average wind speed and direction for the 10-m height is chosen as an example for evaluating the accuracy by comparing the measurements with the historical data obtained from the nearby Minneapolis International Airport monitoring station (National Oceanic & Atmospheric Administration, n.d.). The difference between the two datasets in a chosen month of February is plotted in the Figure 4-2. It shows that wind speeds and directions in Rosemount have similar diurnal and monthly variations as in the observed

airport. Minimal differences in the wind speed and direction suggested that measured wind data have a relatively high quality. Comparison of air pressure at ground level exhibits only 0.1% difference in the hourly average value between the two data sources, confirming that the acquired data from the wind station was already corrected from the sea level and can be used directly in the hydrostatic equation to obtain air pressures at desired hub heights.

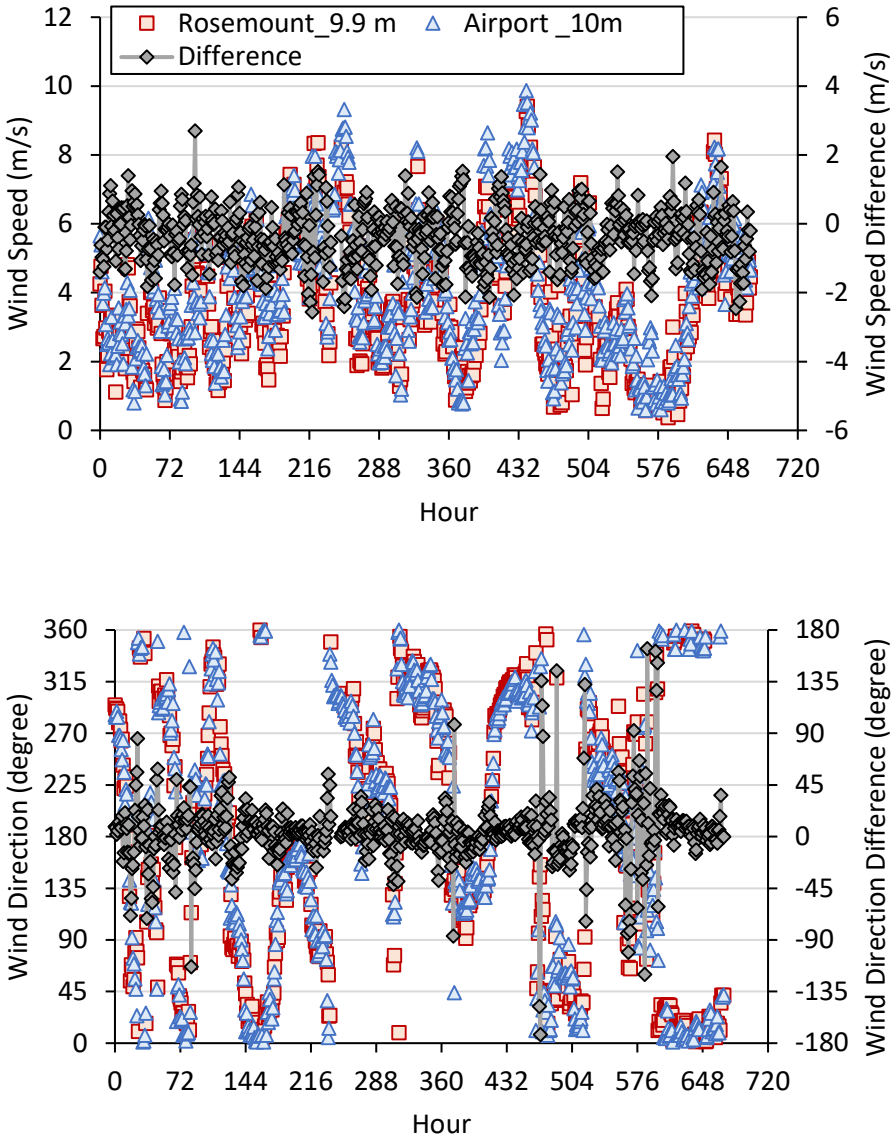

Figure 4-2. Comparison of wind speed and direction between tower measurement and airport history

4.3.3. Modeled Wind Resource Information

As wind resource data from the actual project locations are rarely available at greater heights or have limited access due to commercial policies, numerical wind data are included to assist with the assessment of energy production with increased hub height. The numerical wind database is derived from the Weather Research and Forecasting (WRF) numerical model, which has been credited as the basis for weather forecasting in the United States, providing a representative sample for the analysis. This modeled wind dataset is obtained from an accessible data repository – Gridded Atmospheric Wind Integration National Dataset (WIND) Toolkit, operated by the National Renewable Energy Laboratory (NREL), and can be accessed through a data extraction application programmable interface (Hodge, 2016).

The Gridded Atmospheric WIND Toolkit has a time resolution of one hour and it covers a 7-year duration from 2007 to 2013, containing parameters of meteorological and atmospheric conditions in the US. They are wind speed and direction at nine heights (i.e., 10 m, 40 m, 60 m, 80 m, 100 m, 120 m, 140 m, 160 m, and 200 m), air temperature at the ground surface and the same nine heights, air pressure at three heights (i.e., 0 m, 100 m, and 200 m), and relative humidity at 2 m above the ground.

The potential increment of wind energy production at elevated heights in the wind-rich regions is an important quantity of interest to make economic performance estimates for tall towers. This study uses wind data from the nine sites in Iowa, Minnesota, and Texas to create a geographically diverse data and form a representative sample (see Figure 4-3). Five sites in Iowa including Homestead, Altoona, Mason City, Palmer, and Quimby, as well as Rosemount from Minnesota, are chosen to make comparisons with the actual wind observations from a previous study (Walton, Takle, & Gallus, 2014). The geographic coordinates of the six sites in the WIND Toolkit are obtained by searching the nearest

available data point in the grid. This investigation also helps determine when the WIND Toolkit has difficulty in predicting wind power at higher heights. Together with other three randomly picked sites from the mentioned three states, this paper attempts to ascertain the energy production enhancement and economic benefit for tall towers.

Figure 4-3. Locations of the chosen sites from the WIND Toolkit (red circles indicate a presence of measured data, blue squares indicate the sites from the WIND Toolkit)

4.4. Results

Although the AEP model has been examined with MISO aggregated power data at the seasonal level, the estimated AEP results have not been fully validated with field generation data from the same wind plant (Cai et al., in review). In this section, this estimated hourly energy production is firstly compared with the actual power data obtained from the same wind plant during the same period. Second, the economic outcomes gained by powering from tall towers are estimated using the aggregated power price data from the Midcontinent Independent System Operator (MISO). The WIND Toolkit data are then analyzed and applied in the AEP model in a similar manner to assess wind energy production for more locations in the wind-rich regions. Estimates of the LCOE are finally compared for the chosen sites based on the wind production prediction at different levels.

4.4.1. Comparison of Calculated Energy Production and Wind Power Production

Wind speed and direction at the Minnesota site are firstly analyzed and time histories of hourly-averaged parameters at the heights for commercial utility-scale wind turbines are

plotted in February and August in Figure 4-4. At all considered heights, wind speeds are generally faster at higher elevations but in February, as the northeast winds dominate at all levels, wind flow measured at 101.5 m can easily be blocked by the turbine from the north. Wind speeds at 101.5 m are slightly smaller than the lower level at isolated hours, as illustrated in Figure 4-4a. However, the hourly wind speed has a consistent variation in August as the large wind flow comes from south during this period. Wind direction variations for all heights show similar readings, suggesting that a least wind veer was observed. The patterns of wind speed and direction also agree well with the seasonal variations of historical data in Minnesota (Wichser & Klink, 2008). Noting that the meteorological tower is located to the south of the turbine and their distance is within two rotor diameters, the shading effect that is induced by the strong north wind creates wind speed losses on the meteorological tower and undermines energy production prediction, which is indicated in Figure 4-6. The shading effect is described as a function of wind speed and downwind distance from the effect-generating turbine in previous models and generates a spatial impact on the wind speed deficits, which shows reduced wind speeds along the distance from the generator but also along the height of the tower.

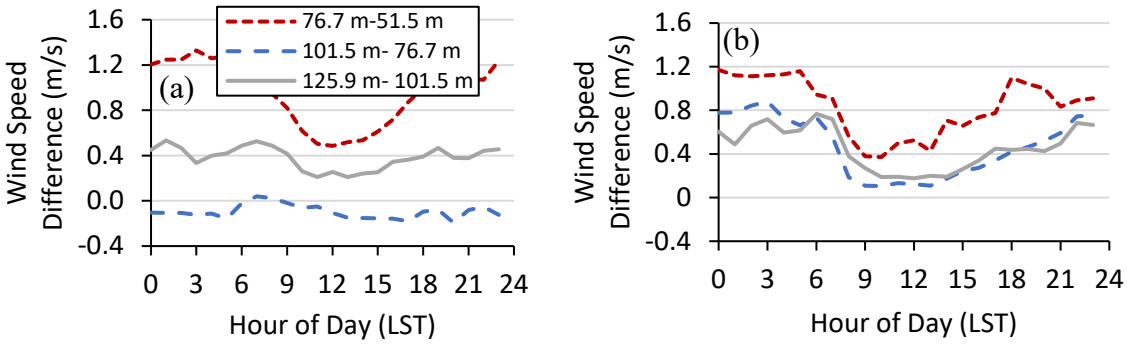

Figure 4-4. Wind speed, wind direction and wind roses at different heights for the chosen month of February (a, c, e) and August (b, d, f) derived from the hourly-averaged data in Rosemount, MN.

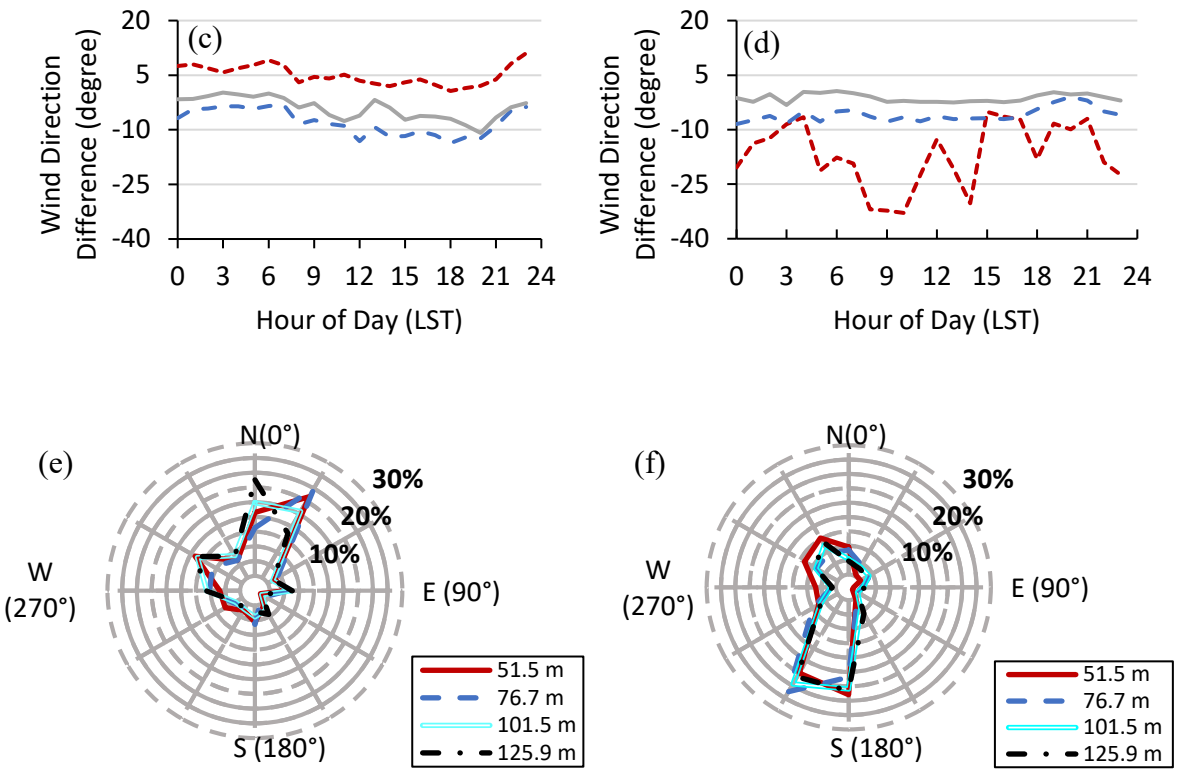

Figure 4-4. (continued)

Since the frequency distribution of wind speed is a vital factor to determine wind characteristics, Figure 4-5 demonstrates the probability distribution of hourly wind speeds compared to Normal and Weibull distribution for the chosen month of February. The histogram and probability distribution of the wind speed in this month show an apparent inconsistency with the Normal distribution but exhibits a Weibull-like distribution (Takle, Brown, & Davis, 1978), especially for wind speed between 3 m/s and 16 m/s, which is the majority range of wind speed in the observation site. Therefore, in the following AEP calculations, Weibull distribution is used to model the frequency distribution of wind speeds for all chosen sites.

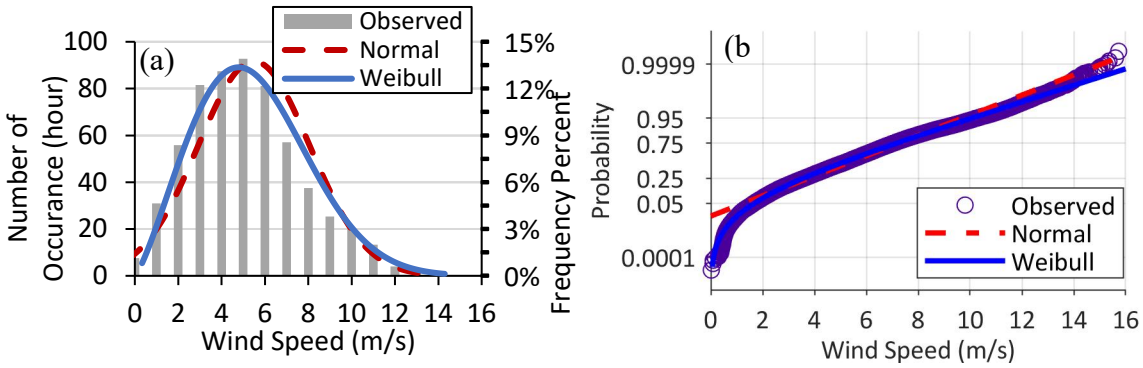

Figure 4-5. Frequency distribution and probability plot of the hub-height wind speed in February

Based on the evaluation of wind characteristics for all considered months, the following validation of the AEP model concentrates on the energy production results that are most relevant to the power generation data. Since the strong north winds play an important role in winter at this site, the comparison conducted for months from January through April presented in Figure 4-6 includes data for all directions and for direction without north flow, which is assuming ±10 degree from the north. This assumption is based on early observations from a wind farm array, claiming that wind wakes would expand 5 degree from the upwind turbine within the first 10 times of D distance, where D is the rotor diameter of the upwind turbine (Barthelmie et al., 2010). It clearly shows that in winter months when the north wind dominates, results calculated from wind speed measurements underestimate the actual energy production if all wind data are considered in the comparison. However, the evaluated energy production can provide estimates more reliable if removing the north winds from the measured dataset as the shading effects from the neighboring turbine impose vital influences on the measurements of the meteorological tower in winter. As shown in Figure 4-6, the difference between the calculated results and measured data reduces from 20% to nearly 1% in February when using the wind data with the north flow filtered out. During the warm

season in the month of August and September, since the observed site experiences minimal north winds, estimates from the original wind data present less than 10% difference compared to the actual power generation. Low wind power is estimated in September due to the small sample size and the generally low wind speed.

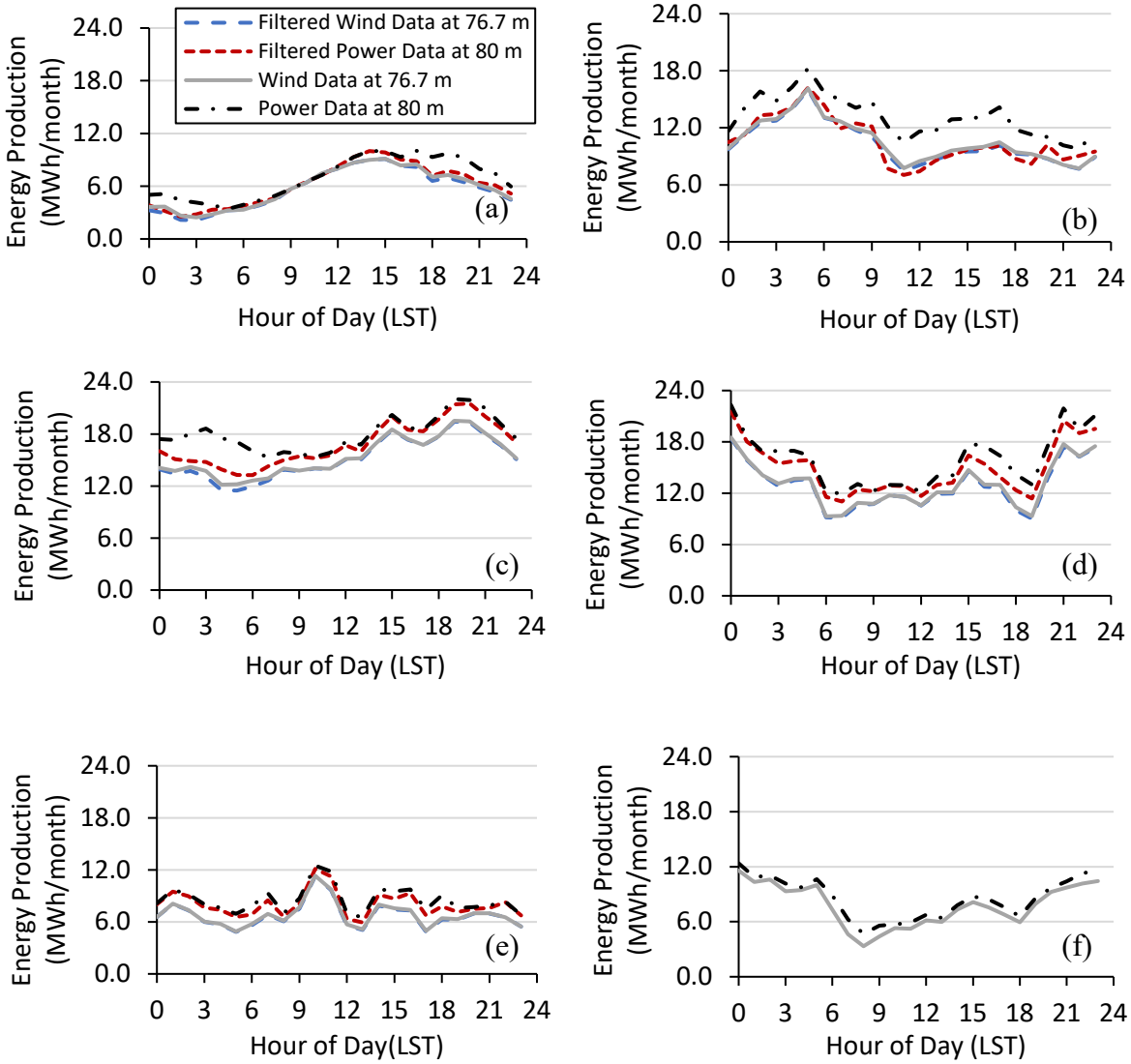

Figure 4-6. Potential energy production at the hub height compared with the actual power generation for all considered months: (a) January, (b) February, (c) March, (d) April, (e) May, (f) August, and (g) September

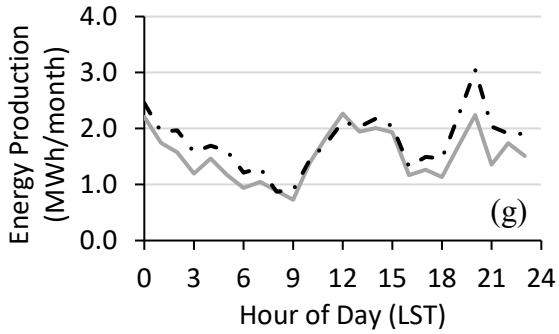

Figure 4-6. (continued)

It is noted that few estimates of hourly energy production deviate from the measurements at several isolated periods in April, as shown in Figure 4-7(a). The largest difference between the power calculation and measured power data occurs between the hour of 384 and 480 when the climate records from the nearby Minnesota-St. Paul airport monitoring station shows a high frequency of snow and raining events took place in this area. Low temperature with such weather condition might cause icing event on the blades and measuring sensors, resulting in disagreement with the actual power data. In general, calculated results from the AEP model (dark grey dotted line) agree well with the power measurements (black solid line) when the shading effect is considered, indicating that the AEP model is a reliable tool to estimate the wind energy production. Therefore, this model is then implemented into the wind data at greater heights to quantify the power potential and financial benefit for tall towers.

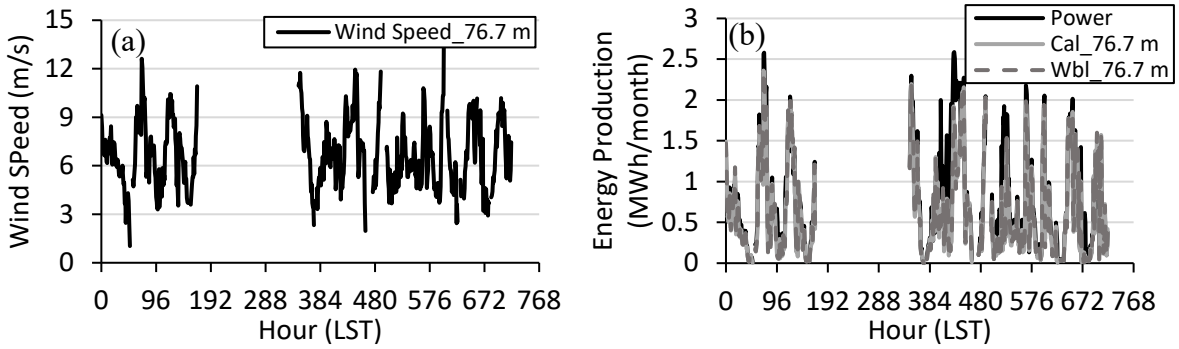

Figure 4-7. (a) Hourly average wind speed and (b) Estimates of wind energy production

4.4.2. Change in the Wind Power Revenue with Increased Hub Height

To establish the relationship between the power price and tower height, a series of energy prices obtained from the Midcontinent Independent System Operator (MISO) historical market report, together with the hourly-averaged Locational Marginal Price (LMP) from the MISO system and the Minnesota hub in 2013 are presented in Figure 4-8 (MISO, 2017). The use of LMP data from the Real-Time energy market is because it reflects the actual cost difference of meeting the local load from different power sellers (MISO, 2013). The time series of power price from the MISO system is calculated by averaging the prices from all associated hubs, which is used to demonstrate that prices from the two sources are similar and thus using the MISO LMP is considerable for sites not near the monitoring hubs. Estimation of energy production at higher heights are also carried out for the year 2013 by applying the validated AEP model to the wind data at other heights. For comparison, Figure 4-8 includes hourly averages of power measurement for the same period, illustrating that estimated energy production at all desired heights fall in a similar pattern as the actual power generation, while the values for a 126 m wind tower show more enhanced power production for the energy market. Due to the shading effects during the cold months, a reduced wind energy production is predicted at 102 m compared to the observations at the hub height. However, for the warm months when the dominant wind speeds from south, the hourly production for taller towers is always greater than the tower at the standard height, indicating a higher potential to increase the economic benefits.

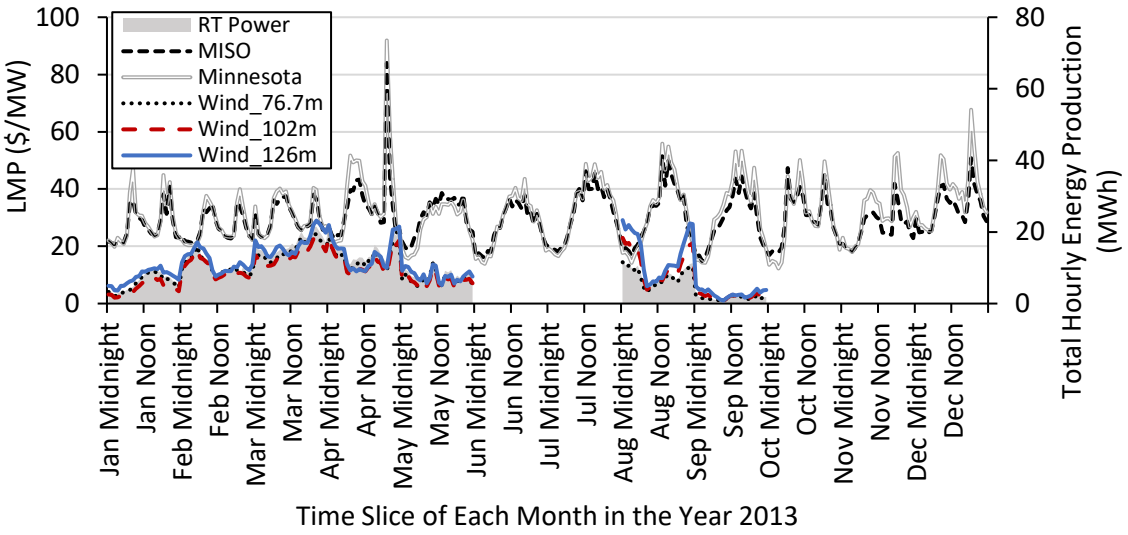

Figure 4-8. Prediction of energy production at 76.7 m (black round-dotted line), 102 m (red dashed line), and 126 m (blue solid line) as well as real-time (RT) power generation (grey area); and historical LMP in the MISO (black dotted line) and Minnesota hub (grey solid line) Real-Time market in the year 2013

Based on the total hourly energy production calculations and LMP archives from MISO market, the change in total hourly payments to generators powering from a taller tower over an 80-m tower can be determined by multiplying the added energy production for each hour with the corresponding LMP. The monthly variation is produced in Figure 4-9. Wind power is assumed to have no influence on the market price to simplify the cost estimate (Krohn, Morthorst, & Awerbuch, 2009). In Figure 4-9, a substantial increase in payments to generators is presented for a 126 m wind tower for all considered months except April caused by unexpected weather conditions. The monthly variation shows that the additional payment gained from taller towers usually increases and reaches its first peak near sunrise when the local load steps up in the morning. Payment changes decrease a few hours after and then rise up again until reaching their second peaks near sunset when an intense demand request in the market. When the market demand falls near midnight, a low payment change is observed accordingly. The estimated peak values are smaller in cold months since the strong wind

speed from north is not included in the energy production calculation. The pattern of total hourly changes in payment to generators indicates that with building tall towers, wind farm developers would make more profits during periods of high demand.

Hourly averaged profits are reduced at the hub height of 102 m in the warm months while values become negative in periods associated with noticeable wind speed deficits as indicated earlier. To eliminate the influence of shading effects on the energy production and profit estimates, a fraction of the original wind measurements, which excludes measurements when north winds occur in the selected site, is implemented in this practice. However, limited data are available from the field, thus the energy production assessment in the next section focuses on implementing numerical wind data that are directly simulated from the Weather Research and Forecasting model.

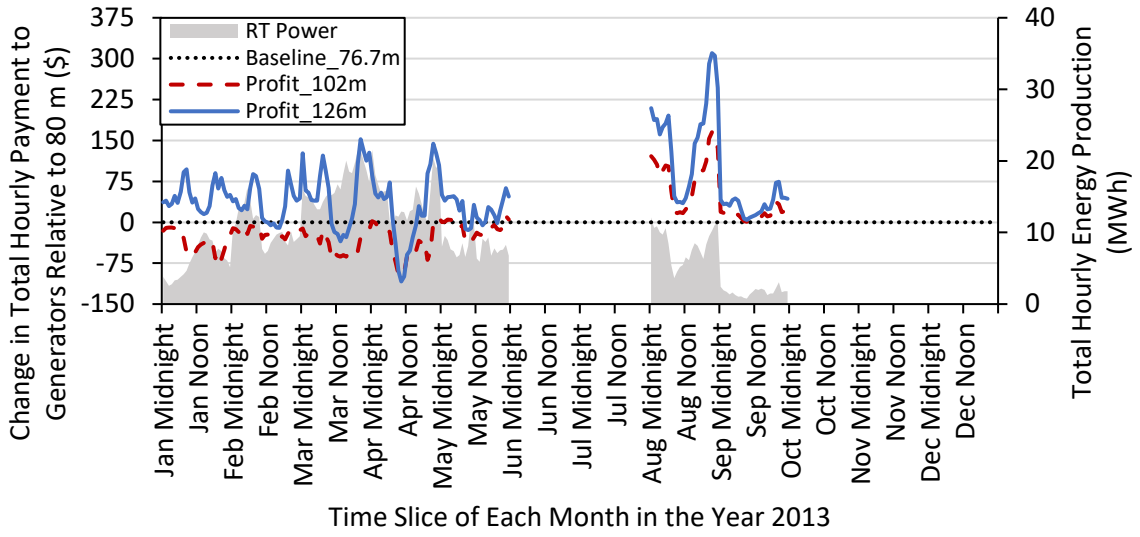

Figure 4-9. Estimated revenue for a wind tower at 102 m (red dashed line) and 126 m (blue solid line) compared to a 76.7-m tower (black round-dotted line). Measured power generation (grey area) in the year 2013 included for comparison

4.4.3. Wind Energy Production Change with Hub Height in Wind-Rich Areas

Since the simulated wind data from WIND Toolkit are not affected by the shading effects and the data repository provides sets of wind data up to 200 m that are not covered by most meteorological towers in the field, the following section focuses on evaluating the wind data in wind energy production and potential revenues for taller towers.

The 7-year wind data for all elevations are first evaluated for a site 2 miles north to the Rosemount wind station (labeled as MN 102942), which is used as a comparison with the actual measurements. Wind speeds at Rosemount are analyzed for their monthly and hourly variations, as shown in Figure 4-10. In addition to the results for heights of typical utility-scale turbines, wind speed variations from 200 m is also added in this comparison to illustrate the upper boundary of wind speed, which can be used to determine the wind power maxima for a 200-m tall tower. Monthly averaged wind speeds are commonly greater in the cold months for all elevations while speeds show the least value during the warm months (June through August). Diurnal wind speeds are produced for different heights and a similar diurnal cycle is explicitly displayed for the chosen heights in Figure 4-10. It presents that the strongest wind occur during nighttime and wind speed slightly decreases near sunrise and remain at a low magnitude until sunset. This pattern of wind speed is found to be consistent with observations from the wind station and sites in the central U.S (Krohn, Morthorst, & Awerbuch, 2017).

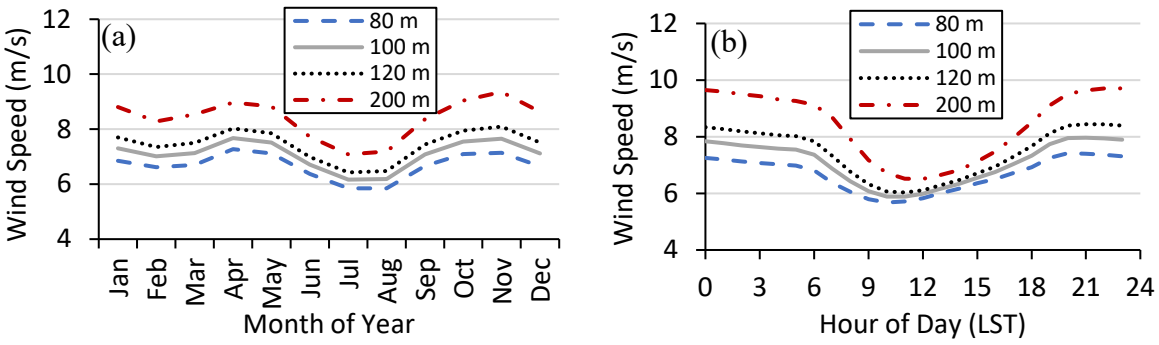

Figure 4-10. 7-year annual (a) and diurnal (b) variations in wind speed derived from hourly WIND Toolkit data in site MN 102942

Given the turbine configurations for the 2.3 MW and 3.2 MW turbine, the accumulated energy production in a year for a larger turbine unexpectedly exceeds the amount produced from the smaller turbine for any observed years at site MN 102942, as illustrated in Figure 4-11. As the height increases, the AEP result grows steadily for each observed year, indicating a 10% and 12% increase for a 20 m increment from an 80-m tower when 2.3 MW and 3.2 MW turbine are considered, respectively. The unrealized substantial increase in wind energy potential obtained from tall towers offers a promising energy supply, but also provides a positive impact on the LCOE reduction for developing tall towers in the wind-rich region.

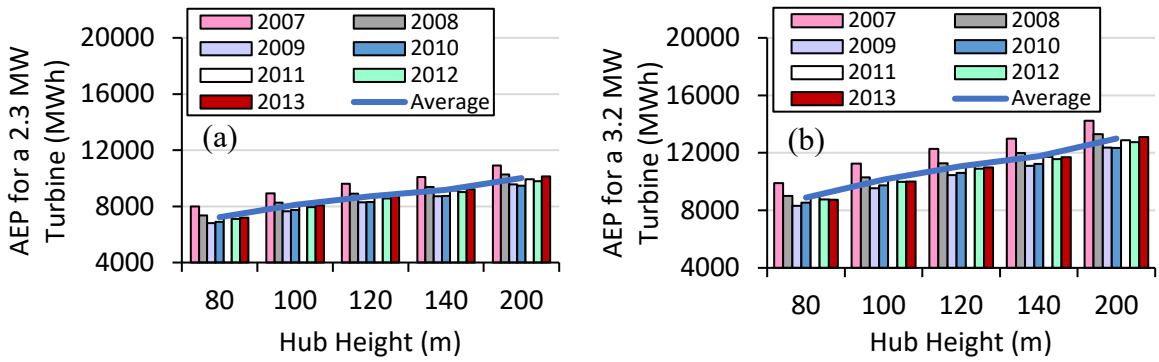

Figure 4-11. Annual averages of AEP estimate for a 2.3 MW (a) and 3.2 MW (b) wind turbine in site MN 102942

To obtain the energy production increment for tall towers in the wind-rich region, similar excercise for estimating AEP is performed for other chosen sites in the state of Iowa, Minnesota, and Texas, and annual capacity factors calculated for towers of different heights are generated in Figure 4-12. It shows a consistent upward increasing trend of capacity factor as for site MN 102942 noted in Figure 4-12. For sites in the wind-rich region, the annual averaged capacity factor for 7 years WIND Toolkit data is estimated between 41% and 50% for a 2.3 MW turbine with a hub height of 100 m, and between 37% and 46% for a 3.2 MW turbine with the same height. This is found to be a slightly higher than that shown in the WIND Toolkit regional capacity factors, which can be explained by turbine size difference since a rated power of 2.0 MW was assumed for each turbine in the analysis of power validation for WIND Toolkit data (King, Clifton, & Hodge, 2014). When comparing to the capacity factor for early measurements from Iowa, the WIND Toolkit values show good agreements for all the five sites (Cai et al., in review).

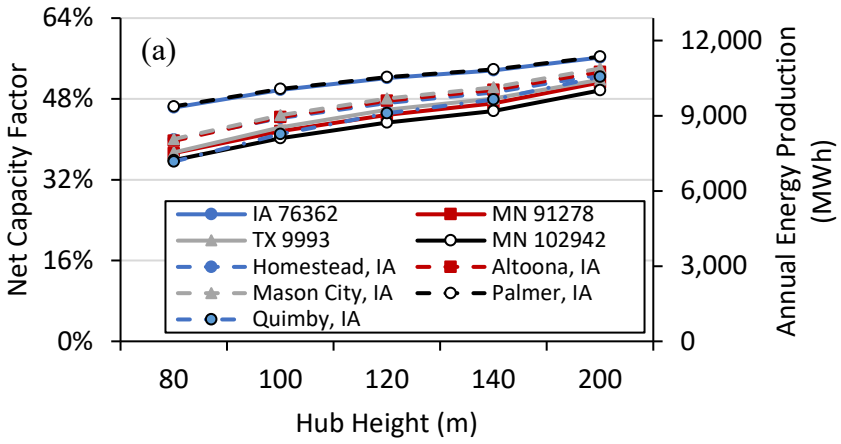

Figure 4-12. Summary of AEP and capacity factor predictions for different tower heights when building a 2.3 MW (a) and 3.2 MW (b) turbine in the wind-rich area

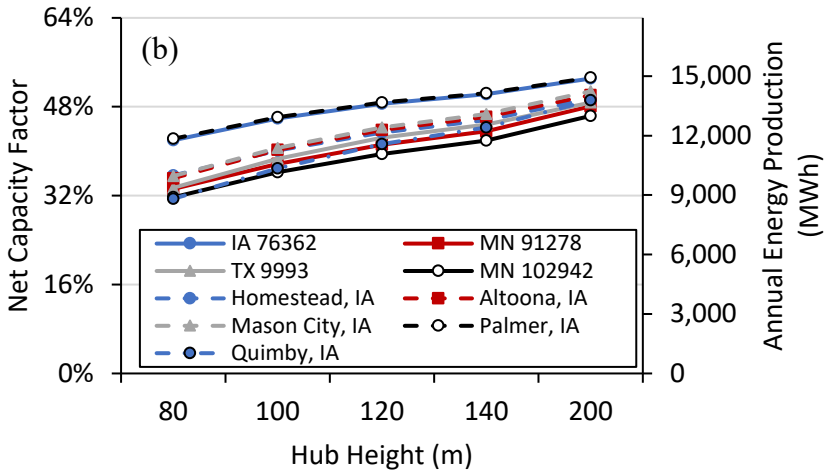

Figure 4-12. (continued)

In Figure 4-13, the relative percentage change of capacity factor derived from the energy production estimates is plotted as a function of hub height for all chosen sites in the wind-rich area. The percentage change are calculated by using the capacity factor at 80 m as a baseline. Results from 100-m data show an approximately 9% and 11% higher when the turbine height increases for a 20 m for a 2.3 MW and 3.2 MW turbine, respectively. The comparison of capacity factors reveals that Quimby shows the highest energy production increment, while the lowest increment is found in Homestead. In addition, larger capacity factor growth is obtained from sites in Minnesota and Texas than that from Iowa, which can be caused by the wind speed modeled by the WIND Toolkit. The apparent growth of capacity factor achieved by increasing hub heights makes tall towers attractive for these areas.

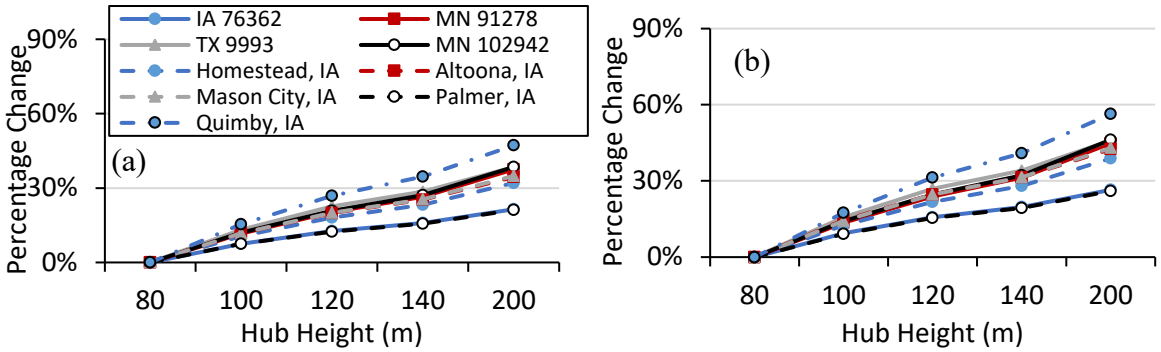

Figure 4-13. Estimated percent change of AEP for different tower heights when building a 2.3 MW (a) and 3.2 MW (b) turbine in the wind-rich area

4.4.4. Levelized Cost of Energy Estimates

Based on the estimated wind energy potentials at elevated hub heights, it is seen that tall towers have the ability to support turbines at larger capacity, provide a clear improvement in the AEP and capacity factor. These improvements are encouraging to lower the levelized cost of energy as the increased energy production benefited from tall towers and large turbine sizes can help offset the incremental expenditure required for additional tower height and blade length.

To estimate the economic benefits of tall towers coupled with large turbines, NREL modeled wind power performance for four assumed turbine configurations with the capacity ranging from 2.5 MW to 4.5 MW, as detailed in Table 4-3 (Lantz et al., 2019). The resultant AEP and capacity factor of these considered wind turbines were then calculated for hub heights of 80 m, 110 m, 140 m, and 160 m, and finally the corresponding LCOEs were summarized for each turbine configuration at different height levels based on previous cost models reported by NREL. However, these cost estimates were constrained by the energy production modeling techniques. In this section, actual wind observations from Iowa, Minnesota, and Texas are rather used in predicting the energy productions and potential cost benefits among various turbines configurations.

Table 4-3. Turbine parameters in the LCOE estimates

	Unit	Today's turbine (Today)	Business as usual turbine (BAU_3.3)	Low specific power turbine I (SP_3.25)	Low specific power turbine II (SP_4.5)
Capacity	MW	2.32	3.3	3.25	4.5
Rotor diameter	m	113	156	166	194
Specific power	W/m^2	231.3	172.7	150.2	152.2

To achieve a 10% decrease in LCOE for today's 80-m turbines, the installed capital cost is first calculated for each turbine size at higher elevations based on NREL estimates of energy production and the results are shown in columns in Figure 4-14. Note that the NREL cost analysis is delivered for hub heights at 80 m, 110 m, 140 m, and 160 m, this capital cost analysis uses the consistent cost assumptions and height values for the following estimates. Solid columns present the resultant installed capital cost and the light-colored columns, which are on top of the solid columns, indicate the change of installed capital cost need to be reduced from the original estimates to meet for the LCOE decline. In general, the installed capital cost rises with the hub height increases for all turbine sizes, and consequently, leading to an increasing demand of the cost reduction in order to lower LCOE. Today's turbine shows the highest demand in the capital cost reduction for each turbine size at different hub heights, indicating that it could face the most challenges to save the capital expenditures. Low specific-power turbine at the capacity of 4.5 MW demonstrates the lowest requirement of cost reduction, followed by BAU turbine and Low SP turbine at 3.25 MW. This difference is primarily due to the annual energy production estimated from these different turbine types, which can be demonstrated by the capacity factor in Figure 4-15.

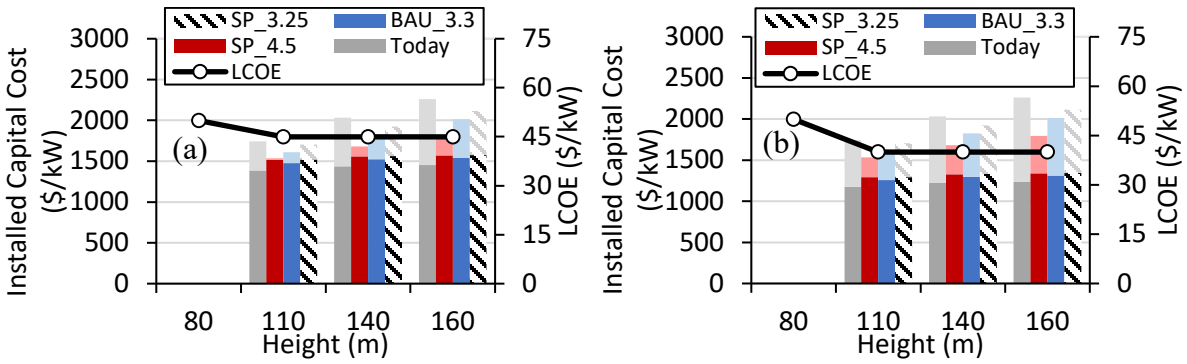

Figure 4-14. Change of installed capital cost for a) 10% and b) 20% reduction in LCOE

Figure 4-15 shows the modified capacity factors in columns reflecting the actual wind observations for the chosen site, MN 102942. Additionally, based on the lower installed capital costs from the previous analysis, the LCOEs, shown in lines, are recalculated and compared with the presumed reduction lines of 10% and 20% for this site. It is clear that the recalculated LCOEs decrease as the hub height increases and reduce to lower values than the initial assumptions for all considered heights. The decline of a 10% assumed LCOE reduction deepens a maximum drop of 28% from 80 m to 110 m and becomes more gradual to 6% from 140 m to 160 m for the two low SP turbines. It suggests that these two low SP turbines are beneficial to be supported by towers taller than 80 m, and more cost effective to be built at 110 m than other heights. Furthermore, as these two low SP turbines can maximize their power capacities at lower wind speeds than Today's and BAU turbines, they generate higher capacity factors and lower LCOEs. Today's and BAU turbines are predicted to lower the LCOE by 20% at 110 m, and additional decreases of 4% are expected when the hub height increases from 140 m to 160 m.

Similarly, using the same modified capacity factors, the assumed 20% LCOE reduction of the two low SP turbines increases to a maximum value of 35% from 80 m to 110 m and changes to 16% from 140 m to 160 m, while the other two turbines show LCOE savings of 30% and 14% for the two hub height intervals, respectively. It suggests that BAU and low SP turbines can create promising commercial interests at 110 m and higher for this site, but the Today's turbine would be expected to be built at 80 m to mitigate the challenges of lowering the installed capital cost at higher hub heights although it has been seen LCOE savings.

To evaluate the impact of hub height on the LCOE savings for the wind rich regions, wind data from the aforementioned sites from IA, MN, and TX are analyzed to estimate the LCOE reduction percentage for each hub height interval from 80 m to 160 m. The quartiles and range of the percentages for presumed 10% and 20% LCOE decrease are summarized in Figure 4-16. Boxes show the 25%, 50%, and 75% quartiles of the LCOE reduction percentages, and error bars show the minimum and maximum values for each hub height interval. It shows that with the hub height increases in the chosen sites, the LCOE reduction percentages of all turbines peak at the height interval between 80 m and 110 m, and consistently decrease to the lowest at the height interval between 140 m to 160 m. This suggests that for the wind rich regions, scaling up the hub height is expected to lower the LCOE and the most cost-effective hub height falls in the range of 80 to 110 m, which aligns with the current market practices. Furthermore, two low SP turbines show higher LCOE savings with the hub height increases, followed by the BAU turbine with the higher specific power, and the Today's turbines demonstrate the lowest LCOE savings. Although more wind observations are needed to determine the optimal hub height for individual wind farms, this analysis helps evaluate the cost benefits for higher hub heights.

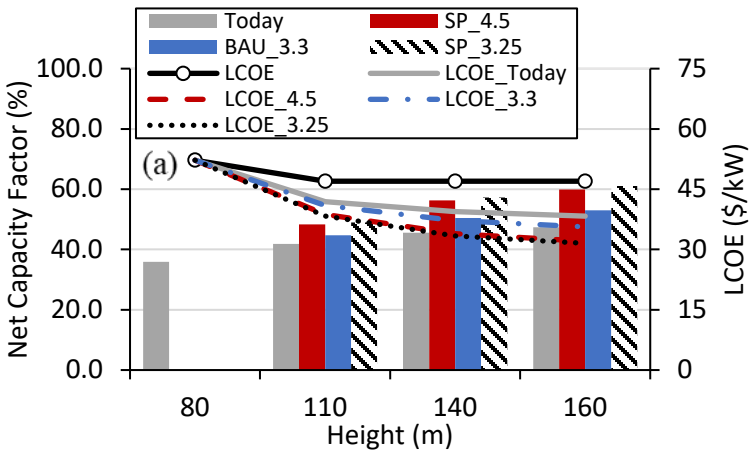

Figure 4-15. Capacity factor increase with hub height and the projected change of LCOE compared to presumed a) 10% and b) 20% reduction for the site MN 102942

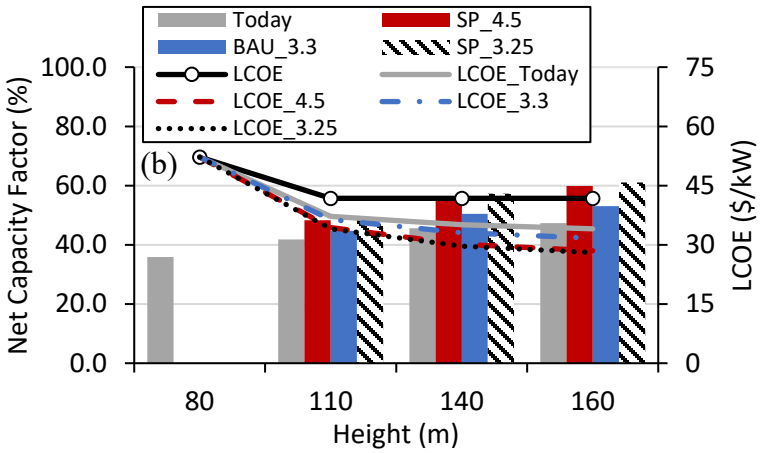

Figure 4-15. (continued)

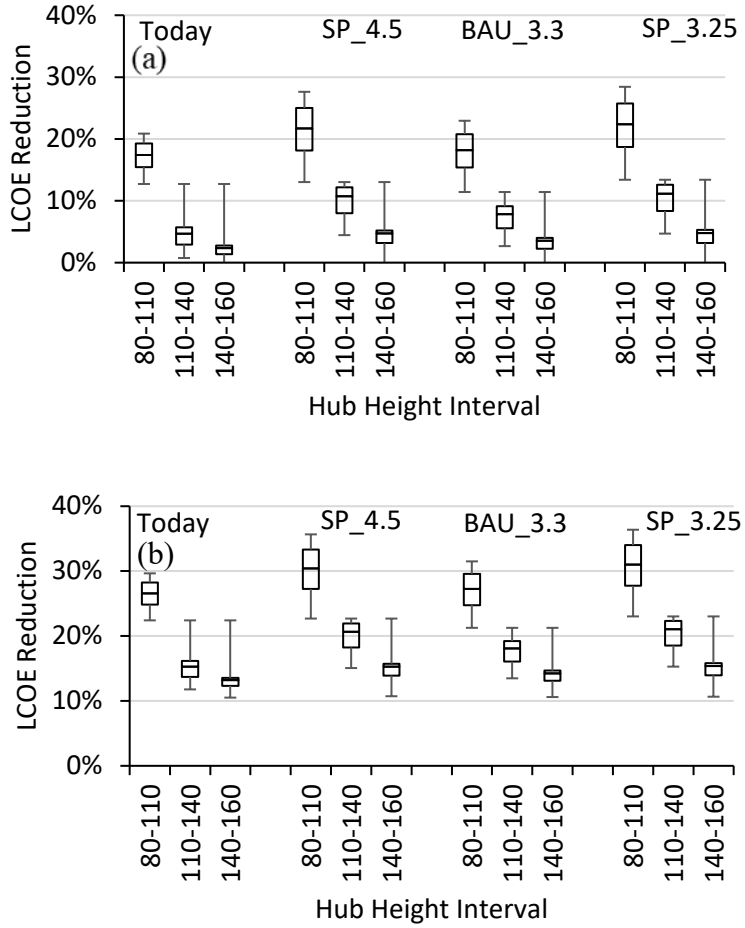

Figure 4-16. Recalculated LCOE reduction between hub heights for presumed a) 10% and b) 20% LCOE savings for the chosen sites in IA, MN, and TX

4.5. Conclusion

Although wind farms in the European and Latin American countries have been actively built and operated with a hub height taller than 100 m, the cost benefits of tall tower installations in the U.S. wind-rich regions have not been clearly quantified over the tubular steel towers at the standard hub height of 80 m, which prevents enabling large penetration of tall towers in the wind industry. Therefore, estimation of energy production and cost benefits from increasing hub heights are essential to understand the opportunities of tall tower applications and this paper uses actual wind measurements and reliable cost models to determine the potential advantages of tall towers in the wind rich regions. Real-time power generation data and wind resource observations from a wind station in Minnesota are first used to examine the reliability of the early-proposed AEP model by making an hour-to-hour comparison. Hourly AEP variations are then combined with the hourly power price to estimate the economic performance for elevated hub heights. Using the validated model, potential AEP and capacity factor are calculated for a set of modeled wind data from the NREL Techno-Economic WIND Toolkit for hub heights up to 200 m. The subsequent LCOE estimates are quantified for four different turbines at hub heights from 80 m to 160 m, suggesting the optimal hub heights for each turbine in the wind rich regions. The following conclusions can be drawn from this study:

- Given that in cold months such as February, north wind is the dominant wind in Rosemount, MN, the resultant AEP values calculated from the measured wind data tend to underestimate the wind energy potential. However, the bias in the wind energy prediction reduces to 1% if leaving out the data associated with the north wind.

- For warm months when the primary wind comes from south and shading effects have minimal influence on the measurements, the calculated AEPs are in good agreements with observations at the turbine height, providing a strong case for the AEP model as a satisfactory model to assess the wind energy production for turbines at different heights. Therefore, assessment of the potential wind energy production is certainly achievable by applying the early-tested AEP model in the chosen area.
- Potential revenues under the increased tower heights scenario increase substantially when a high demand in the market. Declined revenues are obtained for periods of low demand such as midnight. This monthly pattern is constructed based on assuming the influence of wind power on the market price is not accounted.
- To extend the investigation to the wind-rich regions, WIND Toolkit data up to 200 m are also used to estimate the energy production potentials for the two chosen turbines and the obtained results show that with a 20-m increase in hub height, AEP increase of 9% to11% can be achieved, illustrating a similar pattern compared with early findings for other sites in this area
- Wind turbines with lower specific power can save more LCOE with the hub height increases compared to turbines with higher specific power. LCOE estimates show the highest reduction percentage in the hub height interval of 80-110 m, while the percentages decreases gradually with the hub height increases, suggesting that the optimal hub height falls in the range of 80-110 m for turbines in the wind rich regions.

4.6. Acknowledgements

The authors are grateful to the Iowa Energy Center for providing the wind resource from Iowa and Eolos Wind Research Station for providing yearlong wind measurements and power data from Minnesota. Thanks are also extended to the Chinese Scholarship Council for supporting the first author to complete the study. The assistance from Caroline Draxl to acquire WIND Toolkit data from NREL is greatly appreciated. Authors value the input from all of the anonymous reviewers.

4.7. References

American Wind Energy Association. (2017). *U.S. Wind Industry Annual Market Report Year Ending 2016*. American Wind Energy Association: Washington, D.C., USA.

Barthelmie, R. J., Pryor, S. C., Frandsen, S. T., Hansen, K. S., Schepers, J. G., Rados, K., et al. (2010). Quantifying the Impact of Wind Turbine Wakes on Power Output at Offshore Wind Farms. *J. Atmos. Oceanic Technol*. 27: 1302–1317. doi:10.1175/2010JT ECHA1398.1

Cai, B., Vo, P., Sritharan, S., and Takle, E. J. (2019). An Evaluation of Wind Energy Production Elevated Hub Heights. Submitted for review.

Concrete Plant International. (2016). Implementing Precast Concrete Technology in Wind Energy Power Plant Construction. 1: 142-144. https://www.cpi-worldwide.com/us/journals/ arti kel/43851/implementing-precast-concrete-technology-in-wind-energy-power-plant-co Accessed December 7, 2017.

Cotrell, J., Stehly, T., Johnson, J., Roberts, J. O., Parker, Z., Scott, G., et al. (2014). *Analysis of Transportation and Logistics Challenges Affecting the Deployment of Larger Wind Turbines: Summary of Results*. NREL/TP-5000-61063. National Renewable Energy Laboratory, Golden, CO, USA.

Engström, S., Lyrner, T., Hassanzadeh, M., Stalin, T., and Johansson, J. (2010). *Tall Towers for Wind Turbines, Report from Vindforsk Project V-342 Höga Torn För Vindkraftverk Elforsk Rapport* 10:48.

Hodge, B. M. (2016). *Final Report on the Creation of the Wind Integration National Dataset (WIND) Toolkit and API: October 1, 2013 - September 30, 2015*. Report subcontract No. SR-5D00-66189. National Renewable Energy Laboratory, Golden, CO, USA. doi: 10.2172/1247462

Jimeno, J. (2012). *Concrete Towers for Multi-Megawatt Turbines.* Wind System Magazine. 2: 40-45. http://www.windsystemsmag.com/wp-content/uploads/pdfs/Articles/2012_February/0212_Inneo.pdf Accessed December 7, 2017.

King, J., Clifton, A., and Hodge, B. M. (2014). *Validation of Power Output for the WIND Toolkit*. Technical Report NREL/TP-5D00-61714. National Renewable Energy Laboratory: Golden, CO, USA.

Klink, K. (2007). Atmospheric Circulation Effects on Wind Speed Variability at Turbine Height. *J. App. Meteor. Climatol*. 46: 445-456. doi:10.1175/JAM2466.1

Krohn, S., Morthorst, P., and Awerbuch, S. (2009). *The Economics of Wind Energy*. The European Wind Energy Association (EWEA). http://www.ewea.org/fileadmin/files/library/publications/reports/Economics_of_Wind_Energy.pdf Accessed December 7, 2017.

LaNier, M. W. (2005). *LWST Phase I Project Conceptual Design Study: Evaluation of Design and Construction Approaches for Economical Hybrid Steel/Concrete Wind Turbine Towers*. NREL/SR-500-36777. National Renewable Energy Laboratory: Golden, CO, USA.

Lantz, E., Wiser, R., Hand, M., Arapogianni, A., Ceña, A., Simonot, E., et al. (2012). *IEA Wind Task 26: The Past and Future Cost of Wind Energy. Work Package 2.* Technical Report NREL/TP-6A20-53510. National Renewable Energy Laboratory: Golden, CO, USA.

Lantz, E., Roberts, O., Nunemaker, J., DeMeo, E., Dykes, K., and Scott, G. (2019). *Increasing Wind Turbine Tower Heights: Opportunities and Challenges*. Technical Report NREL/TP-5000-73629. National Renewable Energy Laboratory: Golden, CO, USA.

Lewin, T., and Sritharan, S. (2010). *Design of 328-ft (100-m) Tall Wind Turbine Towers using UHPC.* Report ERI-ERI-10336. Ames, IA: Iowa State University.

List, R. J. (1968). *Smithsonian Meteorological Tables*. Sixth Revised Edition. Smithsonian Institute Press: Washington D.C., USA.

Midcontinent Independent System Operator (MISO). (2016). *Archived Real-Time Pricing*. https://www.misoenergy.org/markets-and-operations/#nt= Accessed December 7, 2017.

Midcontinent Independent System Operator (MISO). (2016). *MISO 2013 Annual Market Assessment Report: Information Delivery and Market Analysis*. https://www.misoenergy.org/Library/Repository/Report/Annual%20Market%20Report/2013%20Annual%20Market%20Assessment%20Report.pdf Accessed December 7, 2017.

Moné, C., Smith, A., Maples, B., and Hand, M. (2015). *2013 Cost of Wind Energy Review*. Technical report NREL/TP-5000-63267. National Renewable Energy Laboratory Golden, CO, USA.

National Oceanic & Atmospheric Administration (NOAA). (2017). Local Climatological Data. https://www.ncdc.noaa.gov/cdo-web/datatools/lcd Accessed November 3, 2017.

Press from JUWI AG. (2016). JUWI Constructs Yet Largest Wind Farm in North Rhine-Westphalia. http://www.juwi.com/news/artikel/artikelansicht/juwi-constructs-yet-largest-windfar m-in-north-rhine-westphalia/ Accessed December 7, 2017.

Siemens Market-Specific Solutions. (n.d.). Brochures: Siemens Wind Turbine SWT-2.3-108. https://www.siemens.com/content/dam/internet/siemens-com/global/market-specific-solutions/wind/brochures/product-brochure-swt-2-3-108.pdf. Accessed July 18, 2017.

Sritharan, S. (2015). Wind Turbine Towers: Precast Concrete Hexcrete May Help Increase Renewable Energy Capacity with Taller Hub Heights. *PCI Journal.* 60 (6): 33-38.

Sritharan, S. (2017). *Hexcrete Tower for Harvesting Wind Energy at Taller Hub Heights – Budget Period 2.* Final Report, DOE-ISU-06737-1. Iowa State University: Ames, IA. doi: 10.2172/13 61022.

Stone, N. (2017). *Eolos Educational Data Set: An Overview*. University of Minnesota St. Anthony Falls Laboratory. http://eolos.umn.edu/sites/g/files/pua1541/f/general/eolos_educational_dat a_set.pdf Accessed December 7, 2017.

Sun & Wind Energy. (2012). High Towers, High Flyers. 2: 114- 119. https://www.aeeolica.org/u ploads/documents/2479-sun-and-wind-energy-high-flyers.pdf Accessed December 7, 2017.

Takle, E. S., Brown, J. M., and Davis, W. M. (1978). Characteristics of Wind and Wind Energy in Iowa. *Iowa State Journal of Research*. 52: 313-339.

U.S. Department of Energy, Office of Energy Efficiency and Renewable Energy. (2014). *WINDExchange: Wind Potential Capacity*. U.S. Department of Energy: Washington, D.C., USA

U.S. Department of Energy, Office of Energy Efficiency and Renewable Energy. (2015). *Enabling Wind Power Nationwide.* U.S. Department of Energy: Washington, D.C. https://www. energy.gov/sites/prod/files/2015/05/f22/Enabling-Wind-Power-Nationwide_18MAY2015 _FINAL.pdf Accessed December 7, 2017.

U.S. Department of Energy. (2015). *Wind Vision: A New Era for Wind Power in The United States.* DOE/GO-102015-4557. U.S. Department of Energy, Office of Energy Efficiency and Renewable Energy: Washington, D.C., USA.

U.S. Department of Energy. (2017). U.S. Installed and Potential Wind Power Capacity and Generation. https://windexchange.energy.gov/maps-data/321 Accessed December 7, 2017.

Walton, R. A., Takle, E. S., and Gallus, Jr. W. A. (2014). Characteristics of 50–200-m Winds and Temperatures Derived from An Iowa Tall-Tower Network. *J. App. Meteor. Climatol*. 53: 2387-2393. doi: 10.1175/JAMC-D-13-0340.1

Wichser, C., and Klink, K. (2008). Low Wind Speed Turbines and Wind Power Potential in Minnesota, USA. *Renewable Energy*. 33: 1749-1758. doi:10.1016/j.renene.2007.11.006

Wind-Turbine-Models.com. (n.d.). Siemens SWT-3.2-113 power curve. https://en.wind-turbine-models.com/turbines/966-siemens-swt-3.2-113#datasheet. Accessed July 18, 2017.

Wiser, R,, Jenni, K., Seel, J., Baker, E., Hand, M., Lantz, E., et al. (2016). Expert Elicitation Survey on Future Wind Energy Costs. *Nature Energy*. 1(10): 16135. doi: 10.1038/nenergy.2016.135

CHAPTER 5. LAND - BASED WIND POWER POTENTIAL IN THE U.S. SOUTHEASTERN REGION

A paper to be submitted to Energies or a comparable wind-engineering journal

Bin Cai[1], Sri Sritharan[1], and Eugene S. Takle[2]

[1] *Department of Civil, Construction, and Environmental Engineering, Iowa State University, Ames, IA 50011, USA*

[2] *Department of Geological and Atmospheric Science, Iowa State University, Ames, IA 50011, USA*

5.1. Abstract

The Southeastern states have merely produced wind energy due to the lack of viable wind resource for conventional turbines at the height of 80 m although the U.S. Department of Energy suggested that towers taller than 80 m provide wind energy expansion into areas that was historically considered the least wind energy potential. To realize the opportunity of wind energy development in Southeast, this paper applies actual wind measurements up to 200 m above ground in chosen sites in South Carolina and Tennessee to an early-validated model to predict the annual energy production (AEP) and capacity factor at different heights. Results show that wind energy increases more than 30% if the tower scaling up to 120 m, creating a 30% to 50% increase in the financial gain compared to 80-m towers. Simulated wind data up to 200 m developed by the National Renewable Energy Laboratory (NREL) are then evaluated by comparing the wind characteristics and AEP results with those obtained from the field measurements. Results demonstrate that NREL data overestimate the energy production, indicating that obtaining reliable wind data at elevated heights is important in assessing wind potential and determining the optimum tower height.

KEYWORDS

wind energy; tall towers; field measurements; annual energy production; financial benefits

5.2. Introduction

The U.S. production of electricity from wind has been tripled in the last decade with the development of wind power, mainly on the increased turbine size and tower height. At nearly 90 Gigawatts (GW), wind installations represented approximately 6.3% of the total electricity in the nation by the end of year 2017 and was expected to continue growing to achieve 20% by 2030 and 35% by 2030 (American Wind Energy Association (AWEA), 2020; U.S. Department of Energy (DOE), 2015, 2018). Different characteristics of wind resources across different geographical regions have led to wide variations in wind installations across the United States.

In the southeast states, few utility-scale wind projects have been developed. South Carolina, for instance, has no wind farm developments even though expansive wind-related manufacturers can provide a full supply chain support for wind farm development and operational service for wind projects in this area (Southeastern Wind Coalition (SEWC), n.d.). This is mainly due to the adequate production and relatively low cost of generating electricity from traditional energy sources such as natural gas, coal, and nuclear energy. However, a contributing factor is the absence of wind resources at the height of 80 m, which is the conventional height for the current wind tower technology (Hunter, Griffith, & Beek, 2014). Past studies of wind penetration presented that only one wind farm has been launched in each state of North Carolina and Tennessee, and the majority of the wind energy consumed in the Southeast is imported from nearby wind-rich areas in the Plains such as the Midwest and Texas, which have class 4 and 5 wind speed at 80 m (AWEA, n.d.). However, importing wind power from the Plains to the Southeastern states largely depends on the capacity of the transmission system, and broadening transmission over such a distance involves a very high investment. Therefore, increasing wind energy import to this region may

not be cost effective compared to developing new wind farms in the long term (SEWC, 2014, n.d.).

It is known that for a typical vertical wind speed profile, taller wind turbines can take advantage of faster and more reliable wind speeds and consequently increase the time for generating wind power. Early studies mapped wind speeds at different heights from 30 m to 100 m for the states in the Southeast, showing that the annual average wind speed along the Atlantic Coast increases from less than 5 m/s to nearly 7 m/s, which is sufficient to support commercial wind turbines (DOE, n.d.; AWS Truewind LLC, n.d.). This indicates that taller towers would significantly increase wind power availability in this region. Current research on estimating wind power resources reveals that increasing the turbine height from 80 m to 110 m increases the land area where wind energy could be economically developed, potentially offering significant opportunities for growth in onshore wind energy production. Furthermore, with continued advancement in wind turbine technology, the potential viable land area supporting at least 35 percent capacity factor at 140 m would expand more than four times in the Southeast, as shown in the Figure 5-1. Estimated land areas for wind energy deployment in the Southeast when using available technology (SEWC 2014). This would triple the potential onshore wind resource in this region (DOE, n.d.).

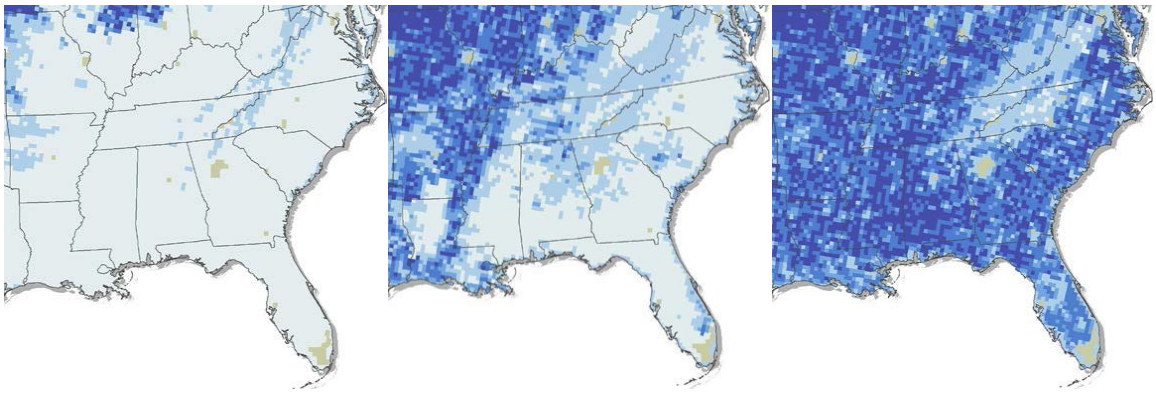

a) 80 m Height with Previous Technology b) 110 m Height with Current Technology c) 140 m Height with Future Technology

Figure 5-1. Estimated land areas for wind energy deployment in the Southeast when using available technology

To achieve taller wind towers to support increased-size wind turbines, there are a number of new techniques, which are known as hybrid and full concrete tower option, available in the current wind industry. These new tower concepts both use concrete tower sections from small prefabricated-modular components that mitigates the transportation challenges from the conventional tower technology. Emerging technologies (e.g., Hexcrete (Sritharan, 2017), Inneo Torres tower technology (Aubery, 2012), Advanced Tower System (Dywidag-systems.com, 2010)) provide opportunities to build utility-scale turbines with hub height as high as 140 m. To evaluate the economics of taller towers, it is necessary to measure and analyze wind data at these heights for estimation in annual energy production (AEP).

To reliably estimate the wind energy potential for tall towers in the Southeast, this paper first analyzes wind measurements up to 200 m from three sites in South Carolina and Tennessee and determines the variations of wind characteristics and power-law exponents with time and height. The statistics of wind characteristics and power laws are then applied to a previously validated model of AEP to evaluate the wind power production at elevated

heights for these chosen sites. Furthermore, these field observations available at high elevations allow for validation of the numerical model used to generate the National Renewable Energy Laboratory (NREL) Gridded Atmospheric Wind Integration National Dataset (WIND) Toolkit data (Draxl et al., 2015; Hodge, 2016). Through a comparison of the power production estimates calculated from the modelled WIND Toolkit dataset and the actual measurements, this paper lastly assesses the performance of the simulated data repository in predicting wind energy production in the U.S. Southeastern region.

5.3. Wind Data Description

5.3.1. Measurements in South Carolina and Tennessee

Wind measurements of more than one-year duration were obtained from the LIDAR (Light Detection and Ranging) and SODAR (Sound Detection and Ranging) instruments in the states of South Carolina and Tennessee. The SODAR data were collected at Conway and Waties Island, located in the broad and flat Atlantic Coastal Plain of South Carolina. Locations of the two wind stations as shown in Figure 5-2. Wind flow obtained from these two SODAR stations are characterized by wind speed and direction every 20 m from 40 m to 200 m and an additional level at 50 m above ground, as well as their corresponding data quality as indicated by the percent of measured data in each time step. Data from the SODAR instruments including ambient temperature, barometric pressure, and relative humidity at surface at each time step, which can be used to character air moisture and density. Wind data from Conway were measured for 3 years beginning May 23, 2012 (Local Standard Time, LST) while the wind station in Waties Island started transmitting data in August 2015. A four-year wind data from June 2012 to June 2016 from Conway and a yearlong wind dataset starting from August 2015 from Waties Island were retrieved from the data collecting system

and used in the power calculation. The field data were reported at the 10-min interval for both sites.

Data from Palmer, Tennessee included wind speed and direction were collected by cup anemometers and wind vanes at the height of 10 m, 30 m, 50 m, and 60 m, while pressure and relative humidity data were collected at 2 m and temperature at 2 m and 60 m. A commercial SODAR device was also placed on the site to capture wind flow at ten different heights, which are 40, 50, 60, 80, 100, 120, 140, 160, 180, and 200 m. Turbulence intensity was calculated by dividing the standard deviation of wind speeds to the mean wind speed of each time interval. Wind data are presented as 10-min average values starting February 2012. Tower data provide more than 3-year continuous observations from February 1, 2012 to May 23, 2015, while the SODAR data span the period from February 1, 2012 to May 23, 2014.

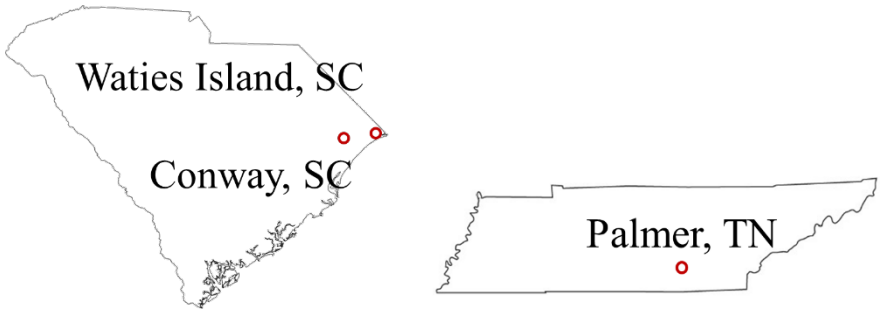

Figure 5-2. Wind monitoring stations in South Carolina (left) and Tennessee (right) indicated as red circles

5.3.2. NREL Data

Modeled wind data provide an alternative to measured data in regions where local observations are not available. Data from the NREL Gridded Atmospheric WIND Toolkit (WTK) were created by using the Weather Research and Forecasting (WRF) model for an extensive grid, covering the continental U.S. for the period 2007 through 2013 (Draxl et al.,

2015; Hodge, 2016). The simulated data have a resolution of one hour for heights of 10, 40, 60, 80, 100, 120, 140, 160, and 200 m. Air temperature at the same nine heights as well as at the surface level, air pressure at 100 m, 200 m, and the ground surface, as well as relative humidity and precipitation rate at the ground surface are also available in the dataset. The WTK data are compared with observed wind conditions to assess the validity of using the Toolkit data at other locations in the region where observed data are not available.

5.4. Analysis and Results

5.3.1. Quality Control for the Field Data

SODAR collected data were filtered to remove low-quality and missing data. In this paper, the filtering criteria of Walls (2009) are applied and specified as: 1) wind speed quality factor must be > 90%; 2) the absolute value of the vertical wind measurement must not exceed 1.5 m/s to remove suspected high-precipitation periods; and 3) the quality factor of turbulence intensity must be > 90%. All SODAR and tower data were compared with near-ground climate data obtained from National Oceanic and Atmospheric Administration (NOAA) for controlling the data quality as discussed in this following analysis.

Wind speeds at 40 m above ground at Conway are first compared with NOAA data from the nearby Horry County Airport for the period June 2013 to May 2016 (Figure 5-3a) (National Center for Environmental Information (NOAA) at Conway, 2018). Conway data show consistent diurnal and seasonal trends with the surface-level measurements from the NOAA station at the Horry County Airport and the wind speed values are relatively higher than the observations obtained from the airport station. A similar comparison is made between the measured wind data from the 40-m SODAR instrument at Waties Island and the NOAA meteorological tower near North Myrtle Beach Grand Strand Airport (Figure 5-3b) (NOAA at North Myrtle Beach, 2018). In this comparison, the airport wind data are chosen

from the same period as the SODAR measurements and the difference in wind speed over 24 h is minimal (<3m/s) at the surface level in the observation period. Barometric pressure and temperature diurnal patterns are also confirmed with the measurements from the NOAA station. For the field site in Palmer, TN, the nearest NOAA station – Winchester Municipal Airport - located less than 50 miles west to Palmer, is used for assessing the quality of wind data from SODAR and tower instruments at the surface level (NOAA at Winchester, 2018). The period from February 2013 – May 2015 is used for the comparison. Figure 5-3c illustrates the diurnal and seasonal cycles of wind speed differences between 40-m SODAR and NOAA measurements and Figure 5-3d demonstrates the differences between 10-m tower data and NOAA measurements. Seasonal variations of wind speed from the inland sites at Conway and Palmer show that summer (June, July, August, JJA) winds have the minimal wind speed difference. SODAR and tower data are a maximum of 3 m/s higher than the nearby airport observations during the day (0600-1800 LST) with a less wind speed increment (0-2 m/s) at night (1800-0600 LST). The seasonal variations of wind speed differences at Waties Island show that larger wind speed differences occur in spring (March, April, May, MAM) and summer than those in fall (September, October, November, SON) and winter (December, January, February, DJF) due to the seasonal sea-land breeze and the maximum wind speed difference is found to be 3 m/s in summer. Diurnal variations exhibit different trends in Waties Island compared to other sites, showing that SODAR data have small wind speed difference (0-1 m/s) with the airport observations in the morning (0400-1200 LST) while SODAR data are commonly 1-3 m/s higher for the rest of the day (1200-0400 LST). This is partly due to high wind speeds occurring during the day and low wind speeds at night for near-the-ground measurements close to the ocean. To sum up, the wind

speed difference between SODAR/tower measurements and NOAA data at nearby airports is less than 3 m/s, suggesting that SODAR measurements are reliable to be used in the following assessment of wind energy production for different heights.

To further evaluate the data quality measured by SODAR instruments, wind speeds at 40 and 60 m are used to compare to those obtained at 30 and 60 m from the meteorological tower in a randomly chosen period, as shown in Figure 5-4. The comparison demonstrates that the SODAR wind speed and direction tend to be very similar to the corresponding tower observations, indicating that the SODAR-collected data are reliable to use in the following wind energy estimate.

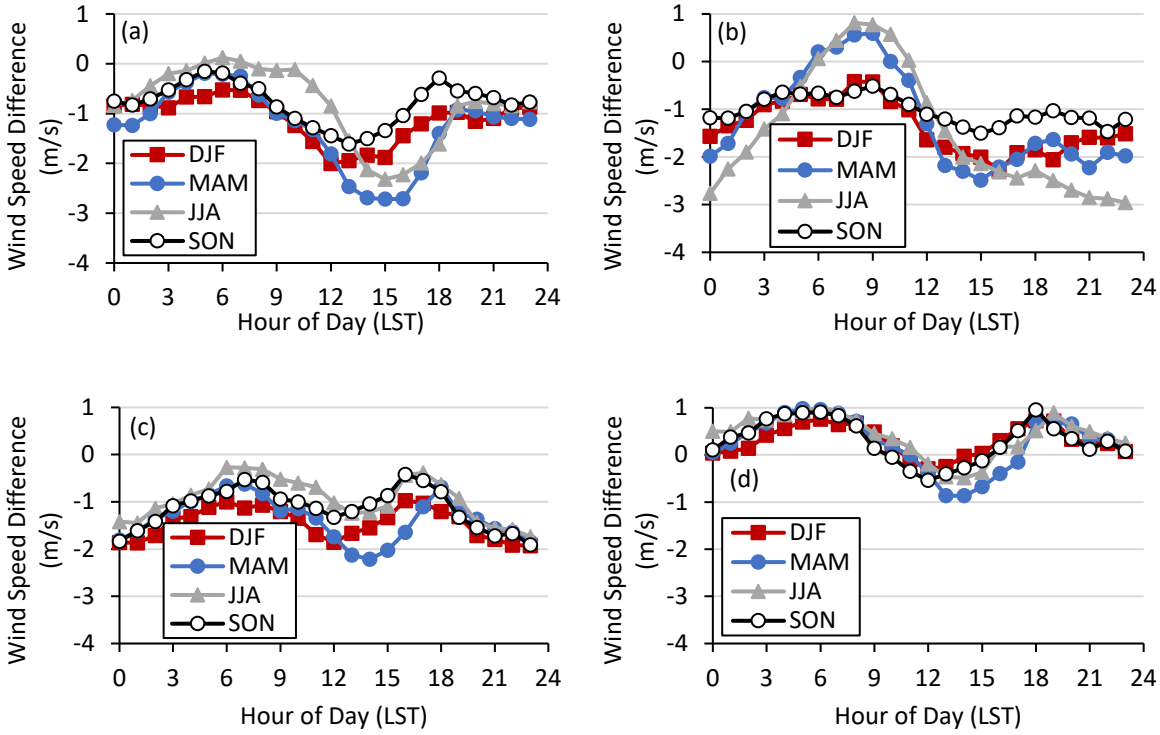

Figure 5-3. Diurnal variations of wind speed difference between tower and NOAA measurements at the surface level in (a) Conway, SC, (b) Waties Island, SC, and (c,d) Palmer, TN

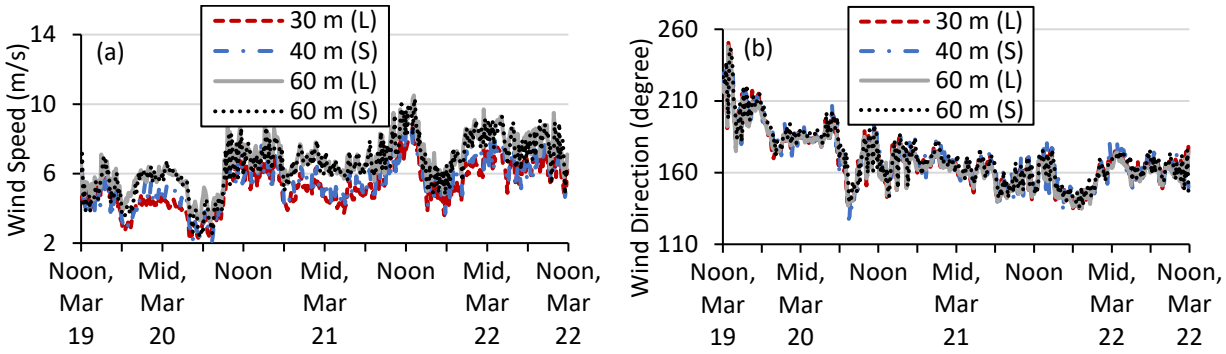

Figure 5-4. Wind speed (a) and direction (b) comparison between SODAR (S) and tower (L) measurements at different heights in Palmer, TN from 19 to 22 March 2012.

Two commercial available utility-scale wind turbines, Siemens SWT 2.3-108 with 2.3 MW rating power and 108-m rotor diameter, and Siemens SWT 3.2-113 featuring at 3.2 MW rating power and 113-m rotor diameter, were used for the power analysis (Studylib, n.d.; Wind-turbine-model.com, n.d.). The power curves for these machines, together with the adjusted air density calculated from virtual temperature, barometric pressure, and air moisture mixing ration, were used for the power estimate (List, 1951). A reduction factor of 2% accounting for the turbine availability between the cut-in and cut-out wind speeds and a 15% loss to account for array losses are adopted from the NREL historical AEP analyses and then utilized to determine the net wind energy potential for desired hub heights (Moné et al., 2017). Energy production estimates are presented in net values in the following analysis if specifically stated.

5.3.2. Annual Energy Production in the Southeastern Sites

Key parameters for determining regional wind energy potentials are wind speeds, dominate wind directions, and the corresponding wind shear and wind veer within the top and bottom tips of the blades. Wind shear describes the variation of wind speed with height and wind veer defines the wind direction change with height. To explore the characteristics

of these parameters, Waties Island are first examined for the diurnal and seasonal cycles of wind speed at different heights that are commonly considered for commercial wind turbines (Figure 5-5). In all chosen sites, summer wind speeds exhibit the least power, which is consistent with the seasonal variations of wind speed found in the wind-rich regions (Walton, Takle, & Gallus, 2014; Cai et al., in review). Additionally, wind speeds at high elevations during the day (0600-1800, LST) are generally lower than the nighttime (1800 – 0600, LST) wind speeds, while winds below 50 m show the opposite diurnal behavior. Wind speeds generally increase with the height for the Southeastern sites in Figure 5-5. Wind directions in the spring and summer months exhibit larger diurnal variations than those in fall and winter, which is likely caused by the sea breeze from the ocean towards land due to the greater temperature differences between the ocean and nearby land in these two warm seasons (Zhong, Leone, & Takle, 1991; Zhong & Takle, 1993; Buckley & Kurzeja, 1997). Waties Island is close to the Atlantic Ocean, so wind speeds from this site are typically higher than the other sites (Figure 5-6). In spring and summer, southwest is the prevailing wind direction while northeast winds dominate the wind flow during cold seasons. This is also aligned with early records for climatology study and weather forecasting in the Southeast area (Zhong, Leone, & Takle, 1991; Buckley & Kurzeja, 1997).

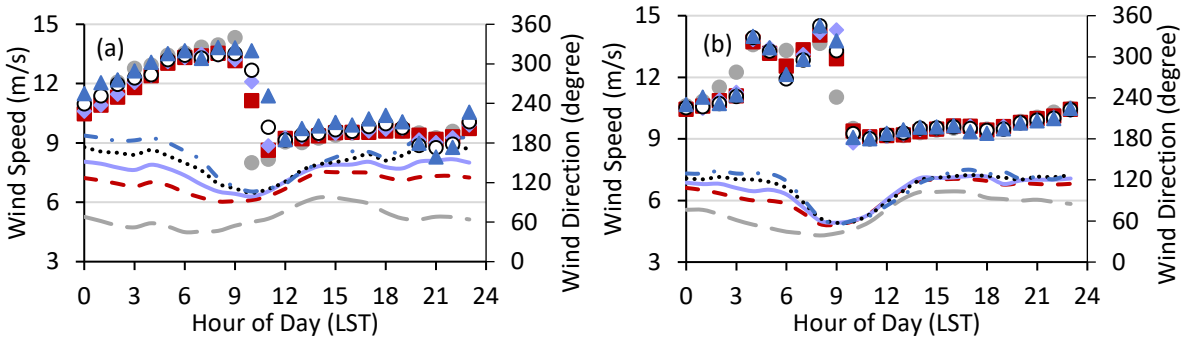

Figure 5-5. Diurnal cycles of wind speed (lines) and direction (dots in corresponding colors) at different heights for each season in Waties Island - (a) spring, (b) summer, (c) fall, and (d) winte

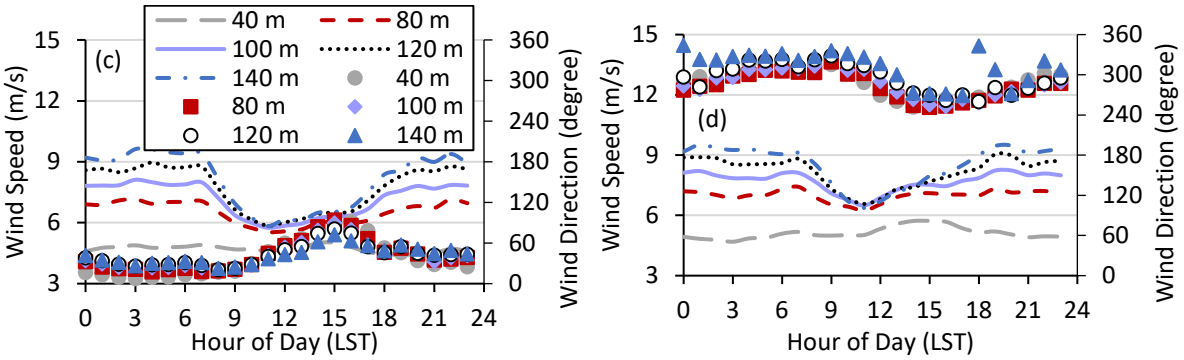

Figure 5-5. (continued)

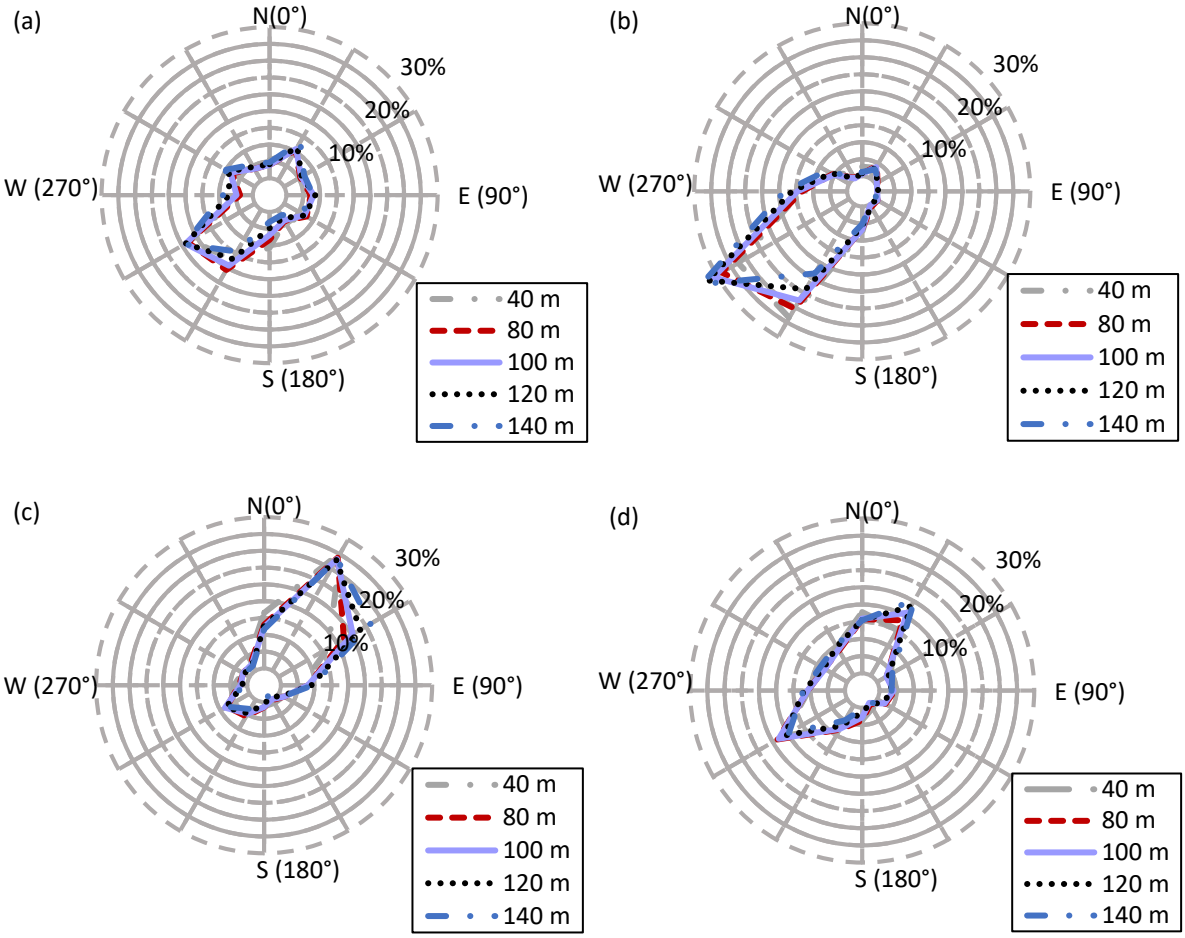

Figure 5-6. Wind roses for seasonal wind speed and direction at different heights in Waties Island - (a) spring, (b) summer, (c) fall, and (d) winter

To characterize the relationship between wind speed and height, wind shear is frequently used in the wind energy industry and commonly calculated as

$$\frac{U_2}{U_1} = \left(\frac{Z_2}{Z_1}\right)^{\alpha} \qquad (5\text{-}1)$$

where U_1, U_2 are wind speeds at height Z_1 and Z_2, respectively, and the power-law exponent α is theoretically defined as 1/7 in studies for generic sites. However, since wind speeds at the top and bottom tips of the blades are available for all the chosen sites, this factor is calculated by using measured wind speed data within the rotor layer (40 m - 140 m) to cover the most region of the sweeping area and then compared with the commonly assumed constant value. As shown in Figure 5-7, seasonal variations of diurnal wind shear demonstrate high values up to 0.5 – 0.6 during the nighttime and lower wind shears closely to the 1/7 value exhibit during the day. Summer time always shows the least wind shear while a comparable wind shear occur for the other seasons. The diurnal and seasonal variations indicate that using a constant value of wind shear to describe the changing pattern is insufficient and thus the actual wind shear pattern is applied in the following energy production calculation.

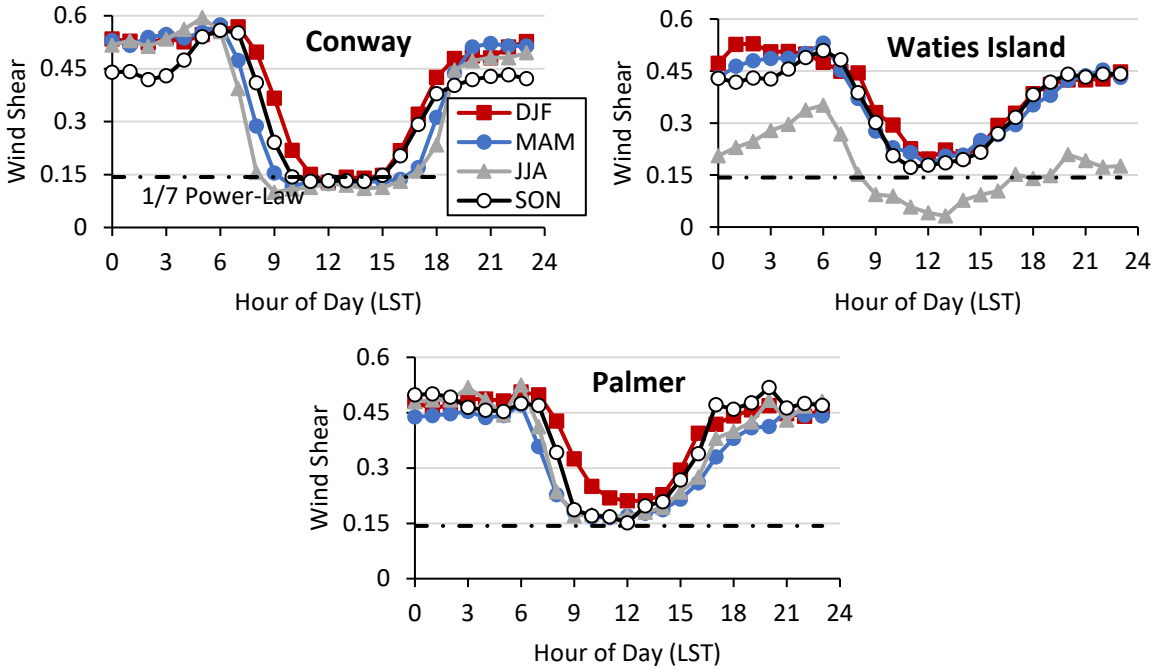

Figure 5-7. Diurnal and seasonal variations of wind shear in the U.S. Southeast sites

Annual Energy Production is typically used to quantify the wind energy produced by a chosen turbine or a wind farm from a selected site in one year. Based on the variations of wind speeds and wind shear and the performance of two different turbines, the wind energy production for a single turbine is assessed for heights from 80 m to 140 m for each chosen location. Figure 5-8 plots the variation of total monthly energy production with time in the observed period, indicating that the potential wind power varies with season. High AEPs commonly occur in the winter and fall seasons when fast wind speeds provide sufficient energy production, but in summer and spring, the Southeast region experiences relatively low wind speeds barely reach cut-in speeds. Since Waties Island is close to the ocean, wind speeds are recorded higher than the other two sites, thus leading to a higher estimated energy production over each month.

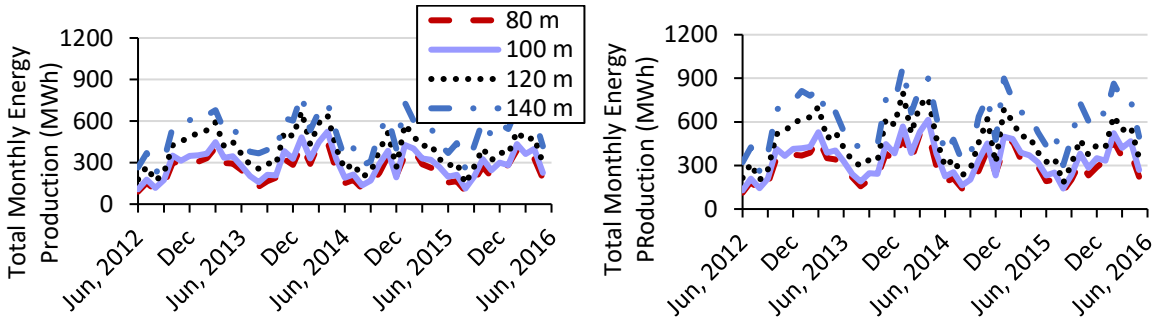

(a) 2.3 MW turbine in Conway, SC (b) 3.2 MW turbine in Conway, SC

Figure 5-8. Estimates of total monthly energy production for the two turbine models in South Carolina (a, b, c, d) and Tennessee (e, f)

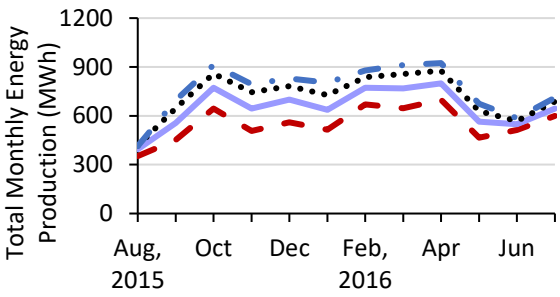

(c) 2.3 MW turbine in Waties Island, SC

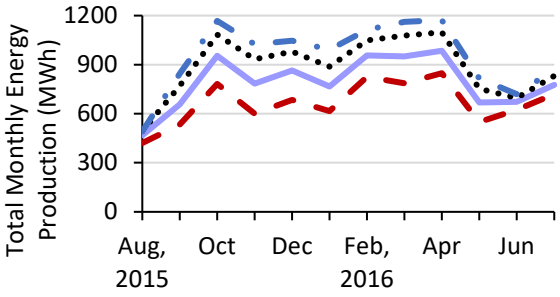

(d) 3.2 MW turbine in Waties Island, SC

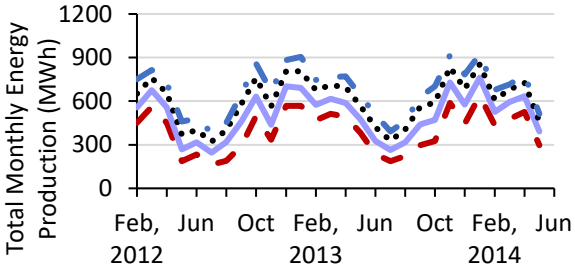

(e) 2.3 MW turbine in Palmer, TN

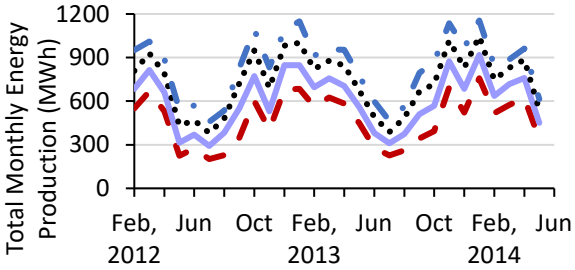

(f) 3.2 MW turbine in Palmer, TN

Figure 5-8. (continued)

Figure 5-9 summarizes the accumulative energy production over a year for the two chosen turbine configurations at the height of 80 m, 100 m, 120 m, and 140 m in the Southeast sites to illustrate the increasing trend of the wind energy production with height. Towers at and taller than 120 m show an apparently higher wind energy potential than those lower than 100 m, suggesting that wind power extracted from turbines at least 120 m exhibits a strong potential to increase the wind integration in this region. Additionally, capacity factors are estimated more than 30% for towers at least 120 m in all sites, only the values from Conway are between 20% and 30%, which is affected by the slightly low wind speed.

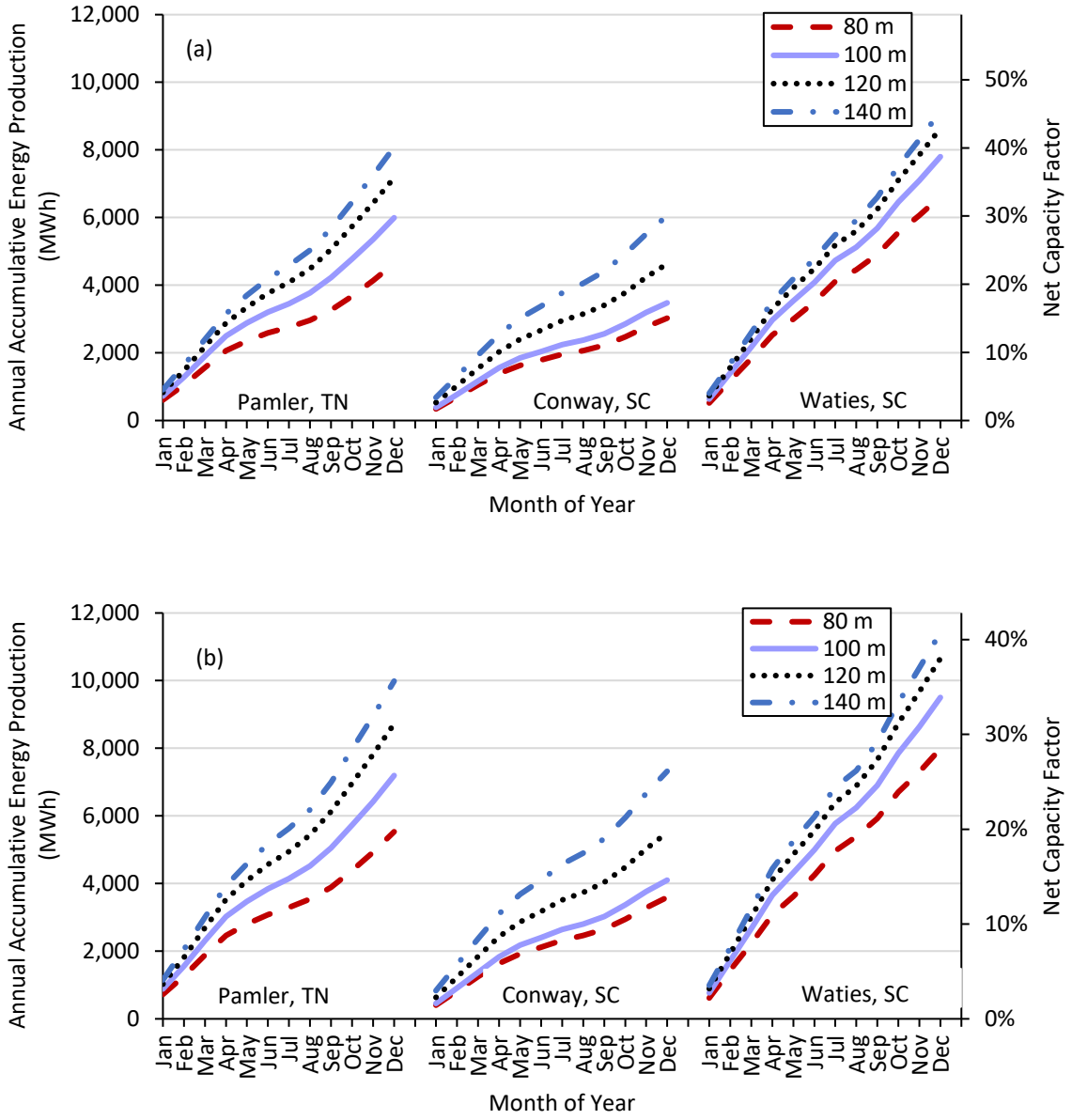

Figure 5-9. Annual accumulative energy production and the corresponding capacity factor for (a) 2.3 MW turbines and (b) 3.2 MW wind turbines installed in the Southeast region

To estimate the effect of hub height on the AEP increment, a comparison of AEP estimate is made among different hub heights for wind turbines in the Southeast region, shown in Figure 5-10. For the high wind speed site at Waties Island, a 30% or more increase in AEP is projected if the hub height increases from 80 m to 120 m, while AEP is estimated

to rise more than 50% for a same height increase for Conway and Palmer. Therefore, the AEP estimation is not only influenced by hub height, but also depends on the site location and its corresponding wind condition.

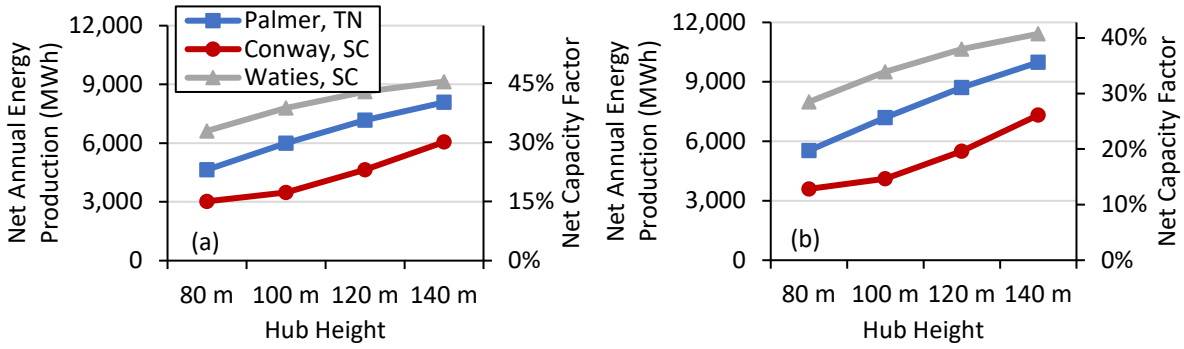

Figure 5-10. Net Annual Energy Production and capacity factor growth with hub height for (a) 2.3 MW and (b) 3.2 MW wind turbines installed in the Southeast region

Since taller towers can accommodate larger turbines with longer blades, this paper also investigates the potential wind power additions for larger turbines with different rating power at higher elevations. Seven commercial turbine models are considered from manufacturers such as General Electric (GE), Vestas, and Siemens & Gamesa, to represent the utility-scale turbines in the United States. These models are GE 2.5 -100, GE 2.5-120, V90-2.0, V110-2.0, V112-3.3, and the two aforementioned Siemens turbines. Figure 5-11 summarizes AEP estimates and the corresponding capacity factors for all of the chosen turbines for heights between 80 m and 200 m at 20 m interval. Using longer blades, AEP and capacity factor are consistently higher than results from turbines with shorter blades although the maximum power output is the same. The increasing AEP and capacity factor attribute to the higher rated speed and lower cut-in speed offered by scaled-up machine and blades. In addition, AEP from larger turbines with higher rating power are also higher than results from smaller turbines with the similar length of blades. The high-energy production is largely

impacted by the lower rated speed developed from the large machine. This trend also implies that integrating taller towers with longer blades in wind farms will generate higher energy production and it is significant to determine the optimum tower height for different turbine types.

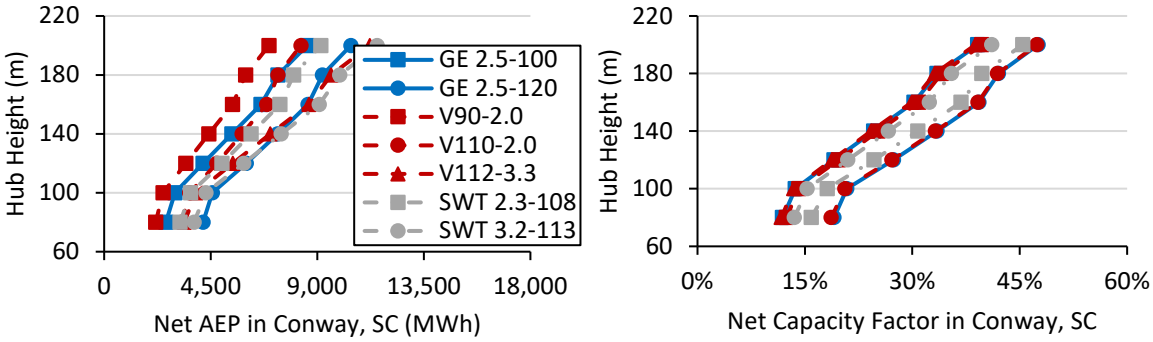

Figure 5-11. Estimates of (a) Annual Energy Production and (b) capacity factor for all chosen turbine models installed in Conway, SC

5.3.3. Financial Gain from Deploying Tall Wind Turbines

Understanding the increasing trend in wind energy production from taller towers is an important booster to expand wind energy deployment in the Southeast region. However, without promising economic benefits of building tall towers, wind industry cannot challenge other generation sources in this region in the long term. Based on the previous analysis in wind energy production, this section quantifies the economic aspects of the tall towers and estimate the financial gain of the wind farm developers would earn potentially on an annual basis if putting tall towers in the farm. Using representative energy rate from a local utility company and the estimated AEP results, the annual accumulated payments are calculated for turbines from the three sites in the Southeast and shown in Figure 5-12. Similar to the inclined trend obtained from the accumulative energy production, the annual accumulated payment for wind towers taller than 120 m exhibits a substantial increase compared to the

economic benefits from 100-m wind towers. The potential gain from upscaling tower height to 120 m varies from $ 160,000 to nearly $ 380,000, revealing a strong annual financial gain of 30% - 50% higher than that from 80-m towers. Moreover, the increasing benefits are expected to continue growing for wind towers taller than 120 m.

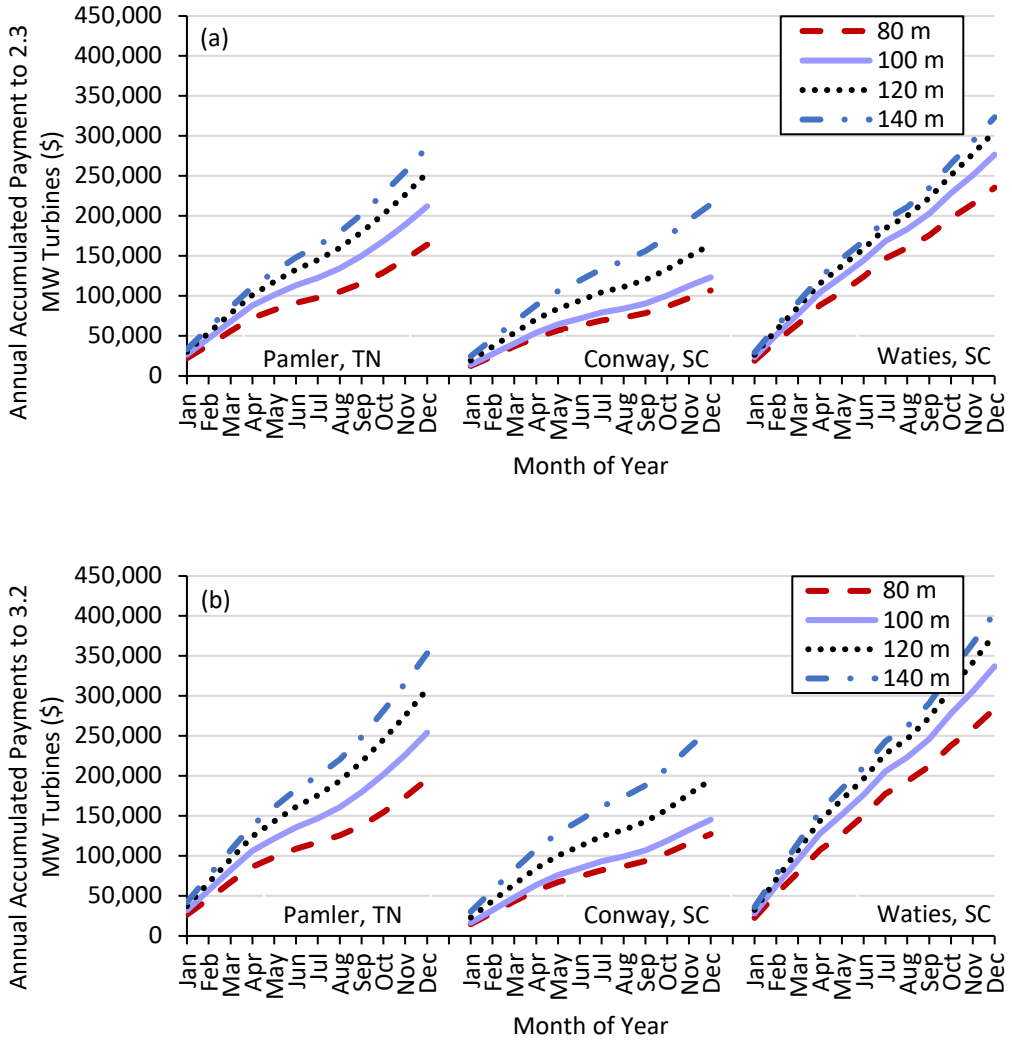

Figure 5-12. Annual accumulative financial gain for powering from (a) 2.3 MW and (b) 3.2 MW turbines in the Southeast region

The difference in annual accumulated payments from towers taller than 80 m and the reference (80-m) level is illustrated in Figure 5-13. It shows that deploying tall towers

positively influences the financial budget for wind farms in the Southeast region. The enhanced wind energy potential contributes to the continuing increase in the accumulative payment change for all of the considered Southeast sites. For sites near the shore, payment differences predicted for wind towers taller than 120 m show nearly a quarter to a third of the total payment. Moreover, these differences estimated for 120 m towers in the interior sites, is expected to be between 30% and 50% of the total annual payment for 80 m towers, and the 140-m benefit reaches at an average of 70% of the total annual payment at 80 m.

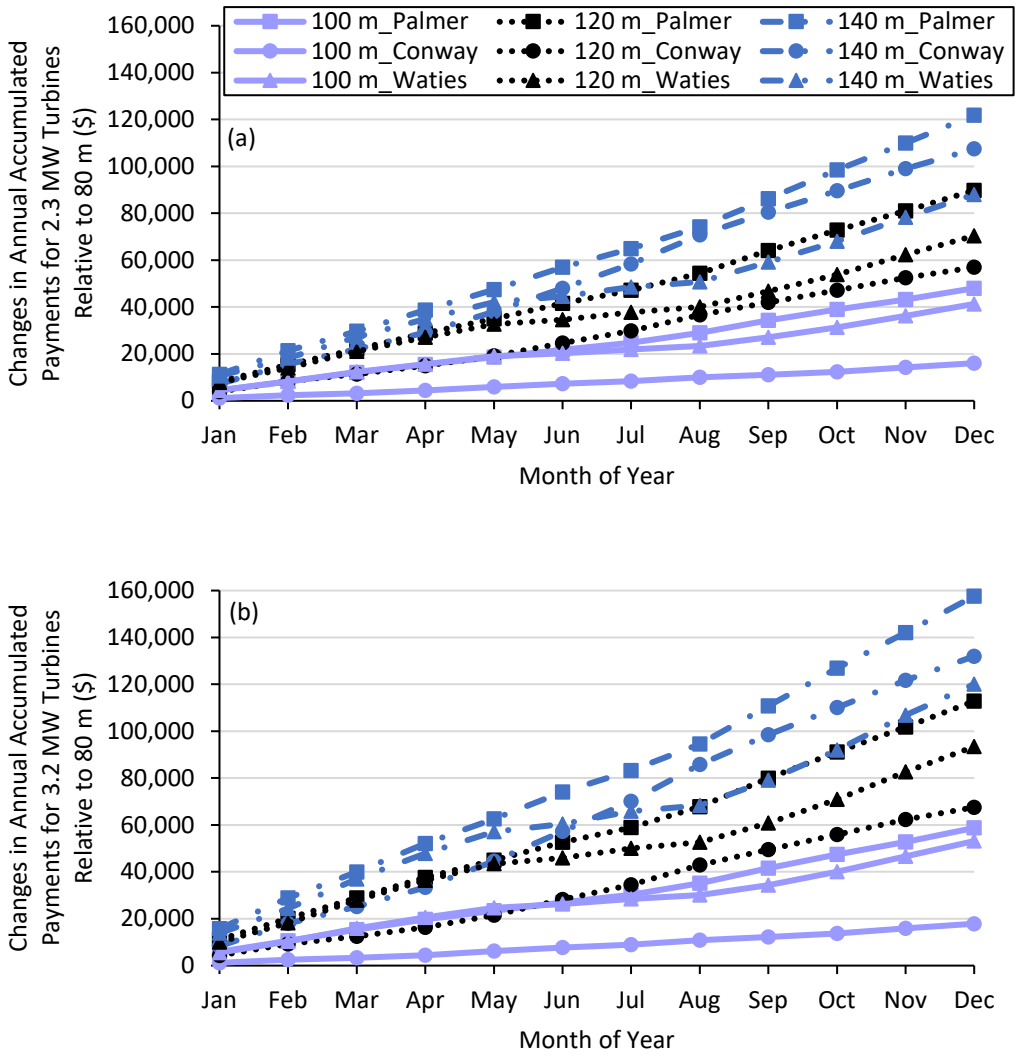

Figure 5-13. Cumulative payment change for (a) 2.3 MW and (b) 3.2 MW turbines at 100 m, 120 m, and 140 m relative to 80 m

5.3.4. Estimates from the Gridded Atmospheric WIND Toolkit for the Southeast Region

The Gridded Atmospheric WIND Toolkit dataset offers model-generated meteorological data that are publicly accessible by a Web interface. By providing the coordinates of the three potential wind farm locations, this interface locates the nearest grid point in the dataset, and the terrain features for the actual field and the simulated grid point are similar because of the proximity. Therefore, the uncertainty from not incorporating local topography is considered minimal in the energy production estimate. To assess the accuracy of the simulated wind data from the Gridded Atmospheric WIND Toolkit, the diurnal variations of wind speed (labeled as lines) and direction (labeled as markers) are obtained for the three sites selected from the dataset, as shown in Figure 5-14. Wind speeds at Waties Island are comparable to the actual measurements (Figure 5-5), while higher values from the WIND Toolkit are found at the other two sites, indicating that the energy production will be reflected higher at Conway and Palmer if using the Toolkit dataset in the estimation. Additionally, a smaller wind speed gradient between different heights is presented in the Toolkit dataset, which generates a steady growth in energy production with the tower height increases. However, the approximately unvarying energy production increment is not consistent with the findings obtained from actual measurements, as shown in Figure 5-9 and Figure 5-10. In the comparison of wind direction, a nearly constant diurnal cycle of wind direction is derived from the Toolkit dataset, which inaccurately characterizes the sea breeze for sites close to the shore. The inconsistency of diurnal cycles of wind speed and direction between the two data sources reveals that it is inadequately to use only Toolkit dataset to analyze wind characteristics and predict wind energy and therefore obtaining field measurements is of vital importance in estimating power production at high elevations.

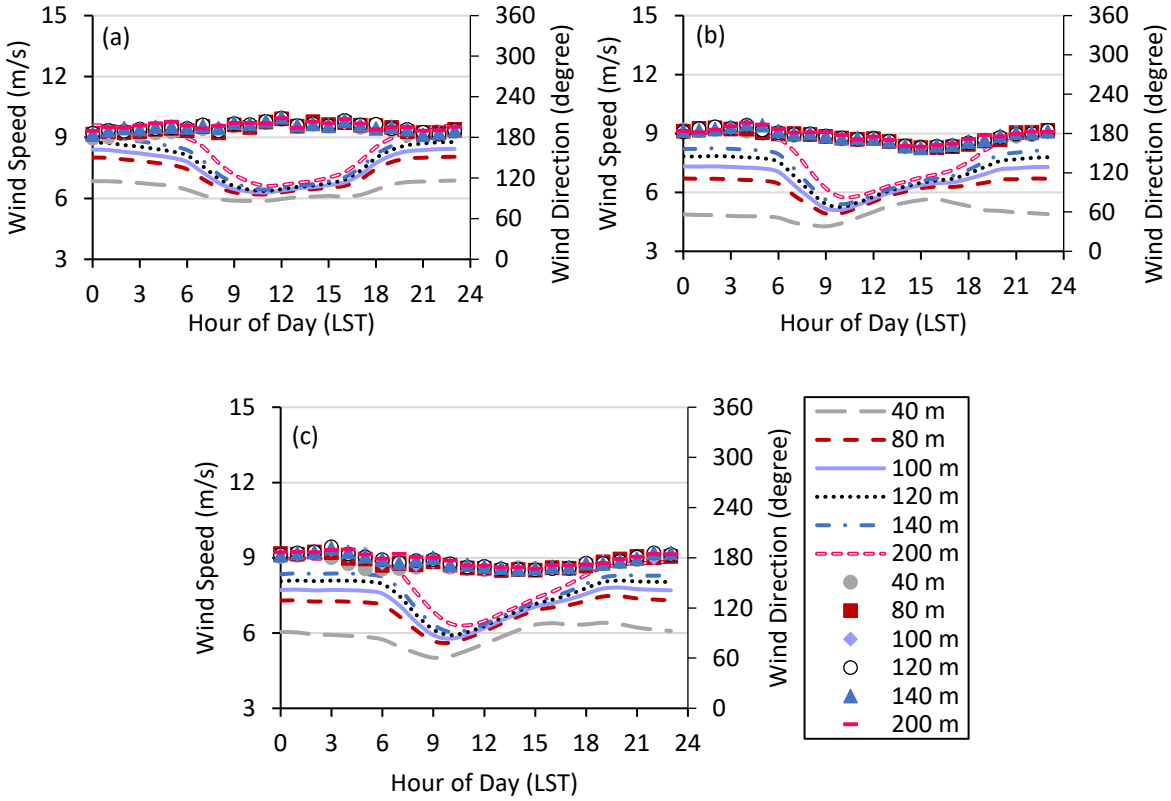

Figure 5-14. Diurnal variations of wind speed (lines) and direction (dots) for the whole data period in (a) Palmer, (b) Conway, and (c) Waties Island

Based on the simulated wind speed and direction as well as the modeled climate condition, Figure 5-15 exhibits the assessment of energy potential at different heights by applying the WIND Toolkit dataset in the previous AEP model. Compared with the results obtained from the actual measurements in Figure 5-10, the estimated AEP and capacity factor produced from the simulated wind data show a similar inclining tendency with the increase in hub height. However, the values of AEP and capacity factor from the WIND Toolkit at Palmer and Conway are more than 60% higher than the observations at 80 m, but the differences between the two data sources reduce significantly as the hub height increases in both two locations, reaching approximately 10% at the height of 140 m. For the site in Waties Island, AEP and capacity factor estimates from WIND Toolkit are within 10%

difference compared to the observations and demonstrate a similar pattern in AEP increment with hub height. However, the WIND Toolkit data show a lower percent increase in AEP as well as capacity factor in Waties Island (Figure 5-16) if using the estimate at 80 m as a reference. This gentle increase pattern can also be predicted by the small increment in wind speed with the increasing hub heights.

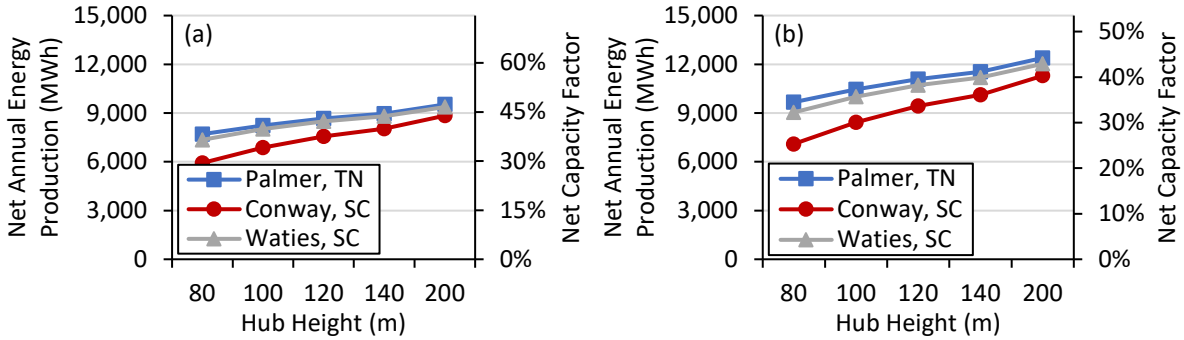

Figure 5-15. Estimates of annual energy production and capacity factor for (a) 2.3 MW and (b) 3.2 MW turbines at different hub heights

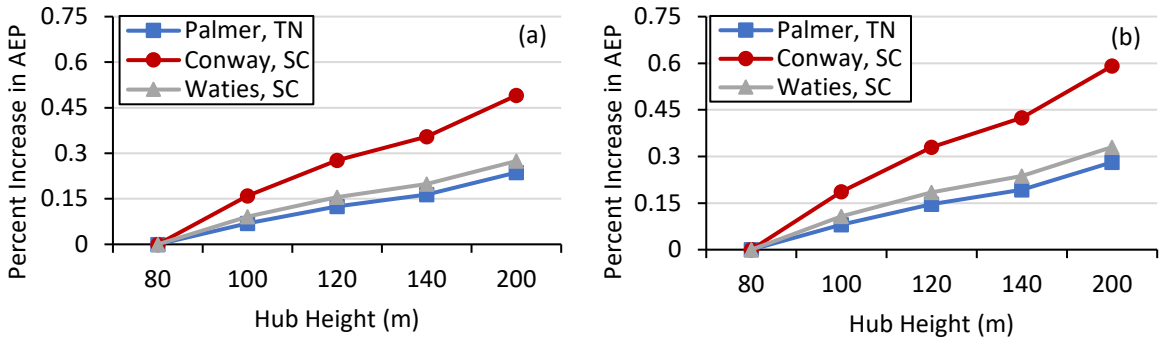

Figure 5-16. Percent increase in AEP for turbines rated at (a) 2.3 MW and (b) 3.2 MW at different hub heights using estimates at 80 m as references

Moreover, a close-up comparison of monthly total energy production is conducted between the two data sources and Figure 5-17 shows the results estimated for the two chosen turbine models at desired hub heights. A linearized trend line labeled as dotted line is found to fit all monthly energy production estimates in each plot and with a line slope larger than one, showing that the WIND Toolkit generally gave higher estimates of wind energy

production than the on-site measurements. The higher estimates of the monthly total energy production is quite different from the findings in the wind-rich regions, where the WIND Toolkit data commonly yield conservative energy production. A filled area, presented in pink in each plot, indicates the range between a standard deviation added to or reduced from the trend line. The standard deviation is calculated for each analysis case and the resulting range well presents the distribution of the estimates. The distributed energy production estimates imply that the modeling accuracy is dependent on site location. Dependence on variance of wind speed and direction, and climate condition indicates that using the meteorological measurements from the actual sites is of importance in evaluating wind power, especially at higher elevations.

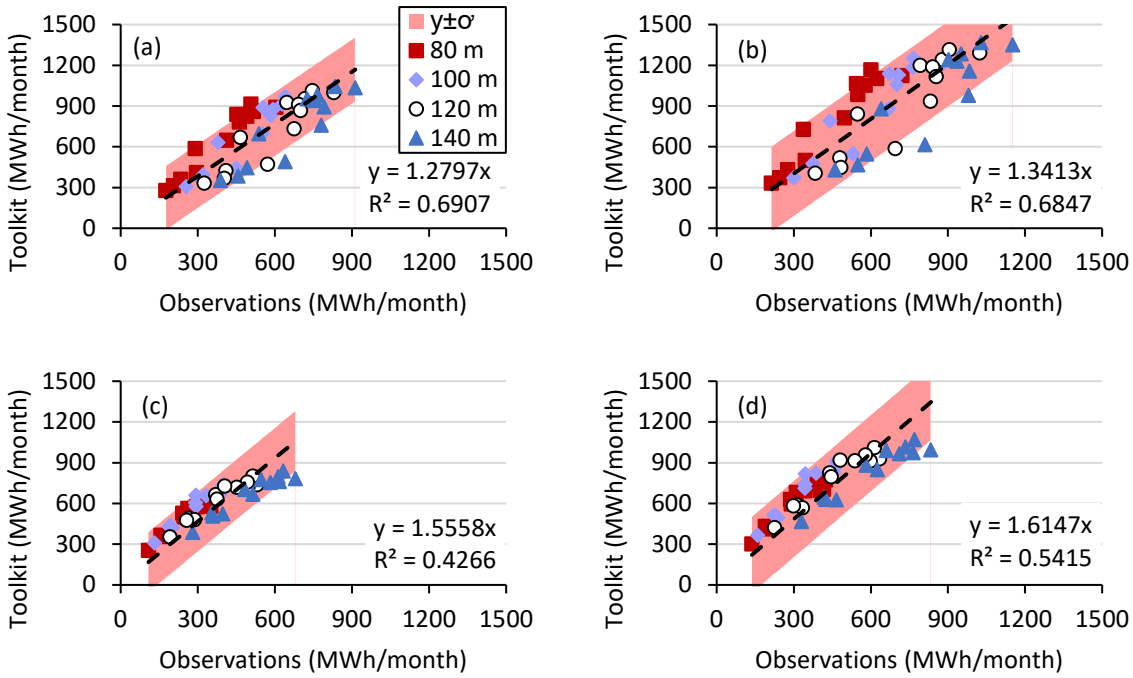

Figure 5-17. Monthly energy production estimated for Toolkit data and wind observations in the three Southeast sites – Palmer (a, b), Conway (c, d), and Waties Island (e,f) – for 2.3 MW (a, c, e) and 3.2 MW turbines (b, d, f) at different hub heights

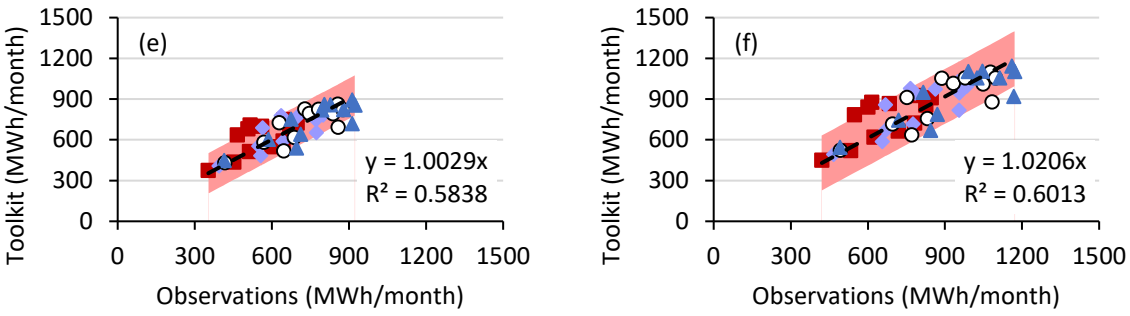

Figure 5-17. (continued)

5.5. Conclusion

Although limited wind energy applications are available in the Southeast region, there is a significant growth in energy production and economic benefits of using the available tall tower technologies such as the Hexcrete Tower to supply wind power generation. To improve the understanding of the wind energy potential in the Southeast region and assist the DOE predictions of the wind power penetration with tower height, this paper utilizes reliable wind measurements from the states in Southeast to determine the energy production over time and the influences of the increased wind power on economic benefits. Measured wind data obtained from the three locations in the Southeast were first used to evaluate wind characteristics, which provides the actual variations of wind speed, wind direction and the power-law exponent with the function of time and hub height. Based on these analyses for all of the three sites, AEP and capacity factor were calculated for potential higher hub heights regarding the two chosen turbine models. Additionally, the economic benefits of taller towers in all three sites were estimated from the energy production increment and the represented energy rates provided by a local utility company. Wind energy assessment was further completed for the NREL simulated dataset from the Gridded Atmospheric WIND Toolkit for the chosen sites in Southeast. The following conclusions can be drawn from this study:

- Diurnal and seasonal variations of wind speed for the three sites exhibited that higher wind speed changes occur at night while smaller changes during the day with increased hub height. Variations of wind direction showed a minimal change with hub height.
- Wind shear calculated from the on-site wind speeds between 40 m and 140 m for all seasons showed similar diurnal cycles compared with those obtained from the wind-rich regions. Results demonstrated that low wind shear occurs during the day and rises after sunset but remains at nearly 0.5 until sunrise of the next day. This strong wind shear during the nighttime is much higher than the theoretical value of 1/7, indicating that obtaining the actual wind measurements at high elevations is essential to evaluate the wind condition and energy production.
- AEP results and the corresponding capacity factors showed significant increase with the hub height increases from 80 m to 120 m, and their values were estimated up to be 50% more than the 80-m towers. The anticipated increment in energy production were coupled with up to 50% additional financial benefits per year compared to the yearly financial gain from 80-m towers for the chosen turbine models. The stronger increase for 120 m tower indicates that using actual wind measurements to predict AEP and capacity factor is important to determine the optimal tower height for a chosen site. Moreover, the inclining trend of financial values from powering wind at elevated heights further improves that wind energy would not only diverse the generation sources but also have positive economic impacts on electricity supply in the Southeast.

- Simulated datasets from the Gridded Atmospheric WIND Toolkit inadequately characterized the sea-land-breeze circulation for the site close to the ocean although showed similar variations of wind speed. Regarding the other two sites, they demonstrated slightly higher values of wind speed than the observations, which created 10% - 60% additional energy production in calculating the AEP and capacity factor. However, smaller changes of wind speed were observed with hub height from the simulated data, and thus generated smaller increments of wind energy production with hub height when compared to the measurements.
- A linear relationship of the monthly energy production was found between the WIND Toolkit data and the observations, which suggests that monthly energy production estimates from the simulated data can fall in the range of the calculated values from the fitted line plus or minus the standard deviation of each analysis case.

5.6. Acknowledgements

The first author is sponsored by the Chinese Scholarship Council for conducting this research. Support for this research was also provided by NSF grant 1701278, NSF ISU Wind-Energy Science, Engineering and Policy IGERT grant (1069283) and USDA-NIFA Hatch Project IOWA4414. Authors are grateful for the Coastal Carolina University and Pattern Energy for providing wind data sources.

5.7. References

American Wind Energy Association (AWEA). (2018). *U.S. Wind Industry Annual Market Report: Year Ending 2017*. American Wind Energy Association: Washington, D.C.

American Wind Energy Association (AWEA). (2018). U.S. Wind Energy State Facts. https://www.awea.org/resources/statefactsheets.aspx?itemnumber=890&navItemNumber=5067 Accessed April 8, 2018.

Aubrey, C. (2012, September). Towers: Concrete Challenges Steel. *Wind Directions*: Brussels, Belgium. pp. 48–50.

AWS Truewind LLC. (2018). Wind Resource of South Carolian: Mean Annual Wind Speed of South Carolina at 100 meters. http://usasolarwind.com/USA Wind Maps/South Carolina/SC_spd100m.pdf Accessed April 8, 2018.

Buckley, R. L., and Kurzeja, R. J. (1997). An Observational and Numerical Study of the Nocturnal Sea Breeze. Part I: Structure and Circulation. *J. Appl. Meteorol. 36*, 1577–1598. doi:10.1175/1520-0450(1997)036<1577:AOANSO>2.0.CO;2

Cai, B., Vo, P., Sritharan, S., and Takle, E. S. An Evaluation of Wind Energy Production at Elevated Hub Heights. (in process).

Draxl, C., Clifton, A., Hodge, B. M., and McCaa, J. (2015). The Wind Integration National Dataset (WIND) Toolkit. *Appl. Energy*, *151*, 355–366. doi:10.1016/j.apenergy.2015.03.121

Dywidag-systems.com. (2010). Prefabricated DYWIDAG Tendons Secure Innovative ATS Hybrid Wind Tower. https://www.dsiunderground.at/en/projects/project-details /article/innovative-ats-hybrid-wind-tower-germany.html Accessed May 15, 2018.

Hodge, B. M. (2016). *Final Report on the Creation of the Wind Integration National Dataset (WIND) Toolkit and API: October 1, 2013 - September 30, 2015*. NREL/SR-5D00-66189. National Renewable Energy Laboratory: Golden, CO, USA.

Hunter, L., Griffith, J., and Beek, T. (2014). *Renewable Energy in the 50 States: Southeastern Region*. American Council On Renewable Energy (ACORE): Washington, D.C., USA.

List, R. J. (1951). *Smithsonian Miscellaneous Collections: Smithsonian Meteorological Tables*. Sixth Revi., Vol. 114. Smithsonian Institution Press: Washington, D.C., USA.

Moné, C., Hand, M., Bolinger, M., Rand, J., Heimiller, D., and Ho, J. (2017). *2015 Cost of Wind Energy Review.* NREL/TP-6A20-66861. National Renewable Energy Laboratory: Golden, CO, USA.

National Center for Environmental Information (NOAA). (n.d.). Local Climatological Data for Station at Conway Horry County Airport, South Carolina. https://www.ncdc.noaa.gov/cdo-web/datasets/LCD/stations/WBAN:00204/detail Accessed April 8, 2018.

National Center for Environmental Information (NOAA).(n.d.). Local Climatological Data for Station at North Myrtle Beach Grand Strand Airport, South Carolina. https://www.ncdc.noaa.gov/cdo-web/datasets/LCD/stations/WBAN:93718/ detail Accessed April 8, 2018.

National Center for Environmental Information (NOAA). (n.d.). Local Climatological Data for Station at Winchester Municipal Airport, Tennessee. https://www.ncdc.noaa.gov/ cdo-web/datasets/LCD/stations/WBAN:00344/detail Accessed April 8, 2018.

Southeastern Wind Coalition (SEWC). (2014). Southeastern Wind Energy Resource Center *Southeast Wind Energy Fact Sheet*. U.S. Department of Energy (DOE): Washington, D.C., USA.

Southeastern Wind Coalition (SEWC). (n.d.). Wind Industry Supply Chain Database & Map. http://www.sewind.org/map/find-companies Accessed April 8, 2018.

Southeastern Wind Coalition (SEWC). (n.d.). Wind Import Fact Sheet. http://www.sewind.org/images/fact_sheets/Wind_Import_Fact_Sheet_edited.pdf Accessed May 15, 2018.

Sritharan, S. (2015). *Hexcrete Tower for Harvesting Wind Energy at Taller Hub Heights - Budget Period 2*. Final Report, DOE-ISU-06737-1. Iowa State University: Ames, Iowa. doi: 10.2172/13 61022.

Studylib. (n.d.). The New Productivity Benchwork: Siemens Wind Turbine SWT-2.3-108. https://www.siemens.com/content/dam/internet/siemens-com/global/market-specific-solutions/wind/brochures/product-brochure-swt-2-3-108.pdf Accessed July 18, 2017.

U.S. Department of Energy (DOE). (2014). WINDExchange: National Renewable Energy Laboratory South Carolina Annual Average Wind Speed at 30 m. https://windexchange.energy.gov/maps-data/231 Accessed April 8, 2018.

U.S. Department of Energy (DOE). (2014). WINDExchange: Wind Potential Capacity. https://windexchange.energy.gov/maps-data?category=potential Accessed June 21, 2017.

U.S. Department of Energy (DOE). (2015). *Wind Vision: A New Era for Wind Power in the United States*. Washington, D.C., USA.

U.S. Department of Energy (DOE). (2018). *Wind Vision Detailed Roadmap Actions 2017 Update*. Washington, D.C., USA.

Walls, L. (2009).*Guidelines for Triton Data Analysis and Comparison to Nearby Met Tower Measurements*. Second Wind System Inc.

Walton, R. A., Takle, E. S., and Gallus, W. A. (2014). Characteristics of 50-200-m Winds and Temperatures Derived from an Iowa Tall-Tower Network. *J. Appl. Meteorol. Climatol. 53*, 2387–2393. doi:10.1175/JAMC-D-13-0340.1

Wind-turbine-models.com. (n.d.). Siemens SWT-3.2-113 Power Curve. https://en.wind-turbine-models.com/turbines/966-siemens-swt-3.2-113#datasheet Accessed July 18, 2017.

Zhong, S., Leone, J. M., and Takle, E. S. (1991). Interaction of the Sea Breeze with A River Breeze in an Area of Complex Coastal Heating. *Boundary-Layer Meteorol. 56*, 101–139. doi:10.1007/BF00119964

Zhong, S., and Takle, E. S. (1993). The Effects of Large-Scale Winds on the Sea-Land-Breeze Circulations in an Area of Complex Coastal Heating. *J. Appl. Meteorol. States*, *32*, 1181–1195. doi:10.1175/1520-0450(1993)032<1181:teolsw>2.0.co;2

CHAPTER 6. AN EXPERIMENTAL EVALUATION OF FATIGUE PERFORMANCE OF HEXCRETE WIND TOWER COMPONENTS AND CONNECTIONS

A paper to be submitted to the ASCE Structural Journal

Bin Cai and Sri Sritharan

Department of Civil, Construction, and Environmental Engineering, Iowa State University, Ames, IA 50011, USA

6.1. Abstract

The increasing wind energy potential with taller tower heights enlightens the interest of developing innovative tower technologies to mitigate transportation challenges and reduce the cost from tubular steel towers. Hexcrete Tower, one of the novel concrete solutions assembled from prefabricated Ultra-High Performance Concrete (UHPC) and High Strength Concrete (HSC) segments, provides an economic design for towers up to 140 m. However, limited reliable data are available for evaluating the fatigue performance of the Hexcrete tower since early experiments on UHPC and HSC were centered on the bridge engineering application which is commonly designed for 1 million load cycles due to the equipment constraints and economic concern. To fill this knowledge gap, an in-plane test was carried out to investigate the fatigue behavior of the concrete tower connections and components involving 2 million operational load cycles and 200,000 extreme load cycles. The test specimen was designed as a column-panel-column unit to represent one segment of a six-sided tower section in a full Hexcrete Tower. In comparison of different loading conditions, the principal strain and maximum displacements at peak loads were taken into account with the increased load cycles. Test results showed that the performance of the test specimen has been excellent and no fatigue damage to tower components and connections has been observed throughout the test.

KEYWORDS

tall wind tower; Hexcrete Tower; fatigue performance; UHPC

6.2. Introduction

With continued technology development, wind industry realizes that taller towers with larger turbines will certainly confirm the attractiveness of wind energy as an economic renewable resource compared to other renewables because of the potential to increase wind energy production and lower the levelized cost of energy (LCOE). However, the dominate tower technology is based on steel towers, which show transportation limits to accommodate for taller wind towers and longer blades. To overcome transportation constrains, Hexcrete Tower technology was developed for taller towers using prefabricated columns and panels that are easily shipped by standard trucks and/or trails and assembled at the field. Two types of concrete –Ultra-High Performance Concrete (UHPC) and High Strength Concrete (HSC) - were utilized to construct hexagonal-shaped columns and rectangle panels, which were tested to be with high strength and durability compared to normal concrete. Tower configurations designed for different hub heights and turbine models are detailed in an early-completed report (Sritharan, 2015). Although UHPC and HSC have been used in bridge engineering for various applications, the fatigue resistance of a wind tower made from these two materials has not been fully evaluated because of limited experiment data for long-period testing (Keierleber et al., 2008; Aaleti et al., 2014).

Experimental studies of UHPC have concentrated on characterizing tensile fatigue strength and thus determining the endurance limit for UHPC specimens. Early static tests conducted for realizing the UHPC tensile strength found that the stress-strain responses can be categorized as elastic, strain-hardening, and strain-softening domains similar to HSC and normal concrete (Lappa, 2007; Switek, 2011; Makita & Brühwiler, 2012). Paschalis et al.

(2016) investigated a modified stress-strain response model of five stages under constant displacement rate with increasing loading amplitudes by using the cyclic tensile loading, compressive loading, and both (Yankelevsky & Reinhardt, 1987, 1989). Based on the fatigue load-displacement responses, the endurance limit was estimated as the maximum stress level for occurring no fatigue failure at a certain number of load cycles in specific domains (Sima, Roca, & Molins, 2008). It was observed that UHPC exhibited enhanced performance under cyclic loading compared to conventional concrete and HSC (Waagaard & Veritas, 1977). Moreover, experimental results presented that tensile strength gains 23%, if the steel fiber volume increases from 1% to 2%, while an only 4% increase in the maximum tensile strength was observed if an additional 1% increase in the fiber volume (Paschalis, 2016). This influenced tensile strength of UHPC indicated that the distribution and orientation of the steel fiber has a significant impact on the fatigue life of the UHPC specimens.

In addition to material characterization, UHPC structural elements have also been examined for fatigue behavior under numerous cycles of service load. Displacement and strain measurements at the center of a UHPC filled joint used for connecting bridge decks showed no significant increase at peak loads with increased cycles and the mid-span displacement at the UHPC slabs used in the waffle deck system remained constant over the test. Minimal changed strain and displacement measurements indicate that the joint type and waffle deck system are sufficient to resistant fatigue loading (Aaleta et al., 2011). Reinforced UHPC beams tested by Makita and Brühwiler (2014) under specified loading conditions demonstrated high fatigue resistances and estimated the fatigue limit of the reinforced UHPC beam was nearly 50% of its ultimate static strength at 10 million cycles. The fatigue limit of reinforced UHPC was confirmed to be effected by the stress in rebar, in other words, the

smaller stress transferred to the rebar, the longer fatigue life of the specimen would expect (Hervig, 2008). One of the fatigue tests conducted for the UHPC and HSC elements on wind turbine towers was completed at Iowa State University along with tests on the tower connections. This experimental analysis demonstrated that using post-tensioned strands for tower connection is efficient to transfer tensile stresses and no visible cracks observed during testing.

Although it was confirmed that the fatigue resistance of UHPC structural members in a wind tower relies on the casting procedure and design configuration, a comprehensive fatigue test on connections of a segmental concrete wind tower has not been performed so far and the relationship between the stress ratio S and number of load cycles N has not been well investigated for UHPC and HSC members in the Hexcrete Tower application. To evaluate the fatigue performance of the Hexcrete Tower connections and tower components, this study conducted 2.2 million of loading cycles on a designed column-panel-column specimen that consists of four hexagonal-shaped columns and two straight panels connected with post-tensioning strands. Both UHPC and HSC members were used and instrumented to monitor stress and strain in each component and relative displacement at the column-to-panel, column-to-column, and column-to-foundation connections in the test specimen. The objectives of this study is to (a) describe the fatigue behavior of different types of tower connections under long period of loading cycles, (b) determine the fatigue strength of different concrete materials used in the designed wind tower, and (c) collect fatigue test data from the isolated Hecrete Tower section to establish an initial database of UHPC and HSC fatigue data for Hexcrete Tower.

6.3. Experimental Tests

The test specimen was developed based on the isolated column-panel-column section from the 120-m Hexcrete tower and combined two different concrete materials in order to test different tower components under cyclic loads (see Figure 6-1). The test load was designed to develop the representative stresses within concrete members and connection interfaces as expected in the full tower. To evaluate the fatigue behavior of different connections in the full tower, the test specimen was designed to use two sets of two full-scale UHPC and HSC columns and two sets of one UHPC and HSC panels. All components precast from a nearby concrete plant along with a cast-in-place foundation block in the laboratory were assembled in the Structural Engineering Laboratory at Iowa State University. The test plan and setup are described in the following sections.

6.3.1. Test Plan

To test different tower connections, the test specimen was also designed as a two-story section: the top section includes two UHPC columns and one UHPC panel while the bottom section includes two HSC columns and one HSC panel. Therefore, the test specimen contains three different types of connections: UHPC column to UHPC panel, HSC column to HSC panel, and HSC column to foundation block. Each side of columns was connected by two sets of eight 0.6-in strand tendons and thus four sets of tendons were developed within columns. In each story, two sets of four 0.6-in high strength strands were horizontally post-tensioned from one side of the left column and anchored to the outer surface of the right column. Two steel block were placed on top of the UHPC columns and linked by a steel beam to equally transfer loads from the loading frame. Constrained to the height limit of the loading frame in the laboratory, the total height of the test specimen was designed to be 4.4 m, including foundation block and two stories of column-panel-column section. To select

the size for columns and panels, two types of columns were constructed in the same size to accommodate the same formwork. The thickness of the two panels were designed to match the stresses within the panels from the top section of the full tower. UHPC panel was designed to have the minimum thickness of 3 in since no additional reinforcements were embedded, while two reinforced layers were added to the HSC panel, contributing to a total of 6-in thickness.

6.3.2. Test Setup and Instrumentation

A test unit, representing the top portion of the full Hexcrete Tower was designed and constructed in order to carry out the fatigue testing. The test unit consists of a foundation block, tower specimen, and top block. The dimensions of the test unit are shown in Figure 6-1. HSC columns were first erected and placed on top of the foundation block with a clearance of 37 1/4 in between the inside surfaces of the two columns. The precast 3-foot wide HSC panel was then placed between the columns, leaving a 5/8 in gap on each side for epoxy filling. UHPC portion was assembled on the top of HSC portion after the epoxy was consolidated. A 1-in thick non-shrink grout was filled within the core area underneath of each column and the gap between the top and bottom panels was 2 in to ensure no contact between the two panels. Two steel blocks were set on top of each UHPC column respectively and connected to the test specimen by vertical post-tensioned tendons. A steel beam was placed between the two blocks to equally transfer the cyclic loads to the two columns. Post-tensioning of the panels was started once the HSC portion was completed and repeated after the upper UHPC portion in place. Each tendon group was stressed to 180 ksi in four stages to achieve a total force of 625 kip in each column. Four stages were applied that required each strand be gradually stressed by 25%, 50%, 75%, and 100% of the total load. Horizontally,

each tendon in the panels was stressed to 165 ksi in a similar manner, reaching a total force of 143 kips after offsetting the seating losses.

The specimen was periodically monitored for assessing the strain and displacement during the fatigue testing. Different types of sensors used in this test are: (a) linear variable differential transducers (LVDT) applied at the interface between columns and panels and the outside surface of column-to-column connections to measure the relative displacement (see Figure 6-2a); (b) strain gauges placed diagonally on the surface of the panels to measure the strain variations on the concrete (Figure 6-2a); (c) string potentiometers placed approximately every 3 ft along the height of test specimen to gauge the in-plane as well as out-of-plane displacements (Figure 6-2b). All of the sensors recorded every 0.1 s by two data acquisition systems.

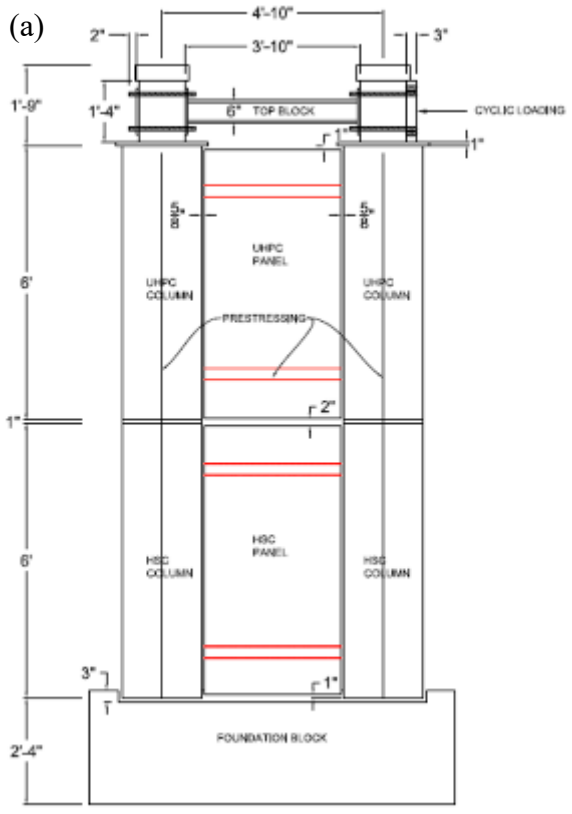

Figure 6-1. Test specimen and loading frame: (a) Elevation view; (b) Schematic of Laboratory test setup; (c) Test configuration (1 in =25.4 mm)

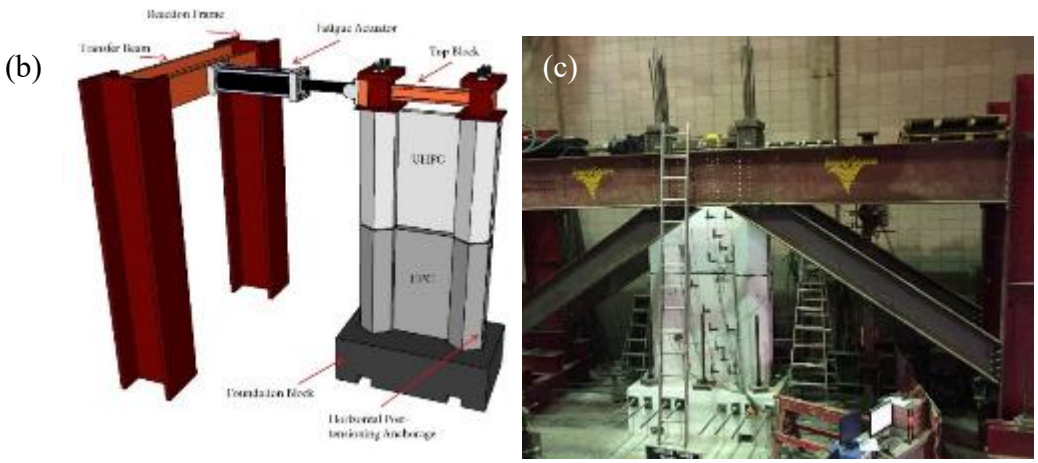

Figure 6-1. (continued)

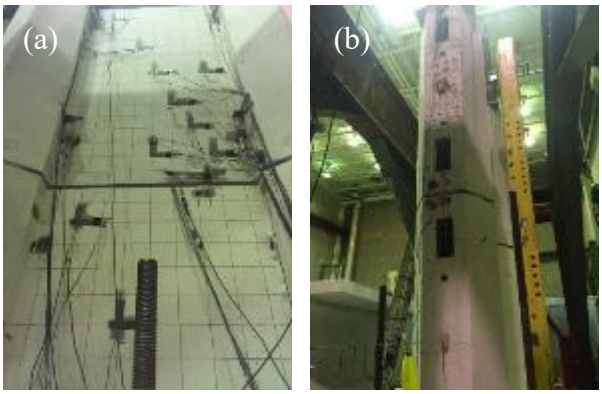

Figure 6-2. Location of (a) strain gauges and (b) displacement transducers on the test unit

6.4. Loading scheme

Two different levels of in-plane load were applied at one side of the test specimen by a hydraulic actuator. The two load conditions were calculated to match the stresses at the top section of a 120-m (393.7 ft) tall Hexcrete tower under the service and extreme loadings. During the service loading condition, the test specimen was subjected to 2,000,000 load cycles of ± 444.8 KN (100 kips) at a constant frequency of 0.8 Hz in a sinusoidal manner, as shown in Figure 6-3. After reaching major test milestones (i.e., 800,000 cycles, 1,500,000 cycles, 2,000,000 cycles), static loads were applied to the specimen at the same maximum magnitude of the cyclic loading to evaluate the status of the test specimen and connections.

After completion of 2 million cycles of the service load, the condition of the test specimen was inspected and the amount of horizontal tendons was considered to reduce. One horizontal strand was removed from each group while the remaining three strands maintained the location and spacing in the test specimen. This resulted in a total tendon force of 477.9 KN (107.4 kips) at each prestressing location. Once the quantity of the horizontal tendons were reduce, additional 200,000 cycles of ± 556 KN (125 kips) were applied at a lower frequency of 0.6 Hz to accommodate the capacity of the facility and reaction frame. Static tests were also carried out at the conclusion of the fatigue test to investigate the test components and connections. The loading frequency of this test was chosen based on the rotational frequency of the turbine (1P) and blade passing frequency (3P). 1P frequency is determined by the constant rotation influence from the group 3 blades on the tower structure while 3P is resulted from the passing frequency generated from the turbine blades. The widely-used design of wind towers has a frequency between 1P and 3P to avoid the excitation frequencies from the wind turbulence loading, rotational frequency, and blade passing frequency. (Arany L., 2016) Therefore, the loading frequency was determined to be approximately at 3P and meanwhile satisfy the operating requirement in the structural laboratory. Throughout the paper, negative load values represent the specimen was pulled towards the actuator generating positive in-plane displacements, while positive loads indicate the specimen was pushed away from the actuator resulting in negative in-plane displacements.

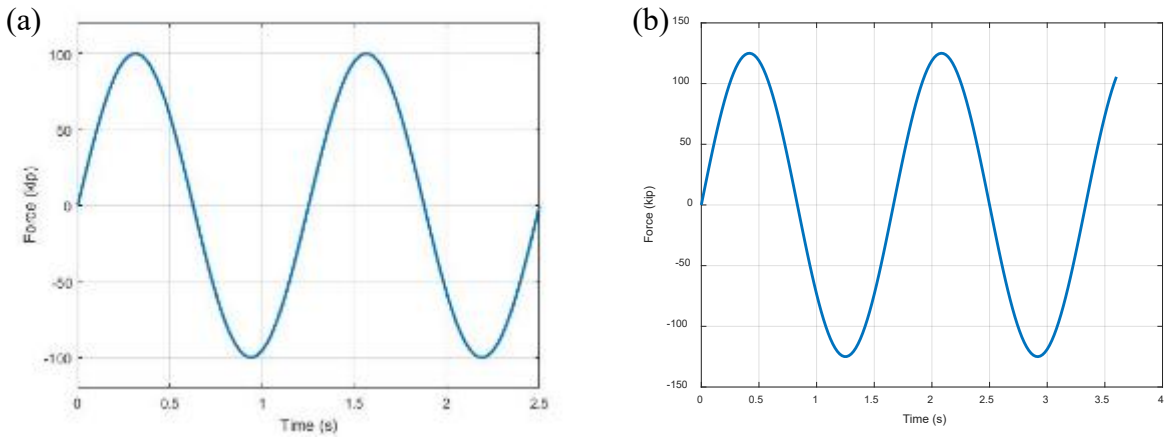

Figure 6-3. Sinusoidal fatigue force history during a) operational and b) extreme load testing (1 kip = 4.45 KN)

6.5. Test Results

The observations and results of the test specimen under two different loading conditions are presented below. The overall response of the connections was examined, followed by a detailed observation on the displacement of the test specimen and strain responses of the concrete panels.

6.5.1. Test observations

All of the three types of connection were inspected periodically, a few cracks was developed at the upper corner of the interface between columns and panel, as shown in Figure 6-4a and Figure 6-4b. Two LVDTs mounted at the top of the UHPC panel recorded a small relative displacement of ± 0.1016 mm (0.004 in) between the columns and the panel in the loading direction, suggesting that the test unit was moving in unison and the columns and panel were still fully contact. Although these cracks created gaps within the interface separating the column and the panel, the gap was localized in the uppermost region of the panel and only opened up in tension and had little impact on the total response.

In the middle of the interface near the gap between the UHPC portion and HSC portion, observations showed no cracking at the service load level. In this region, the bond

strength of the columns and epoxy is 12.9 KN (2,900 psi), which is able to sustain load through increasing relative transverse displacement. The maximum relative displacement of ± 0.0508 mm (0.002 in) was observed at the peak load of the service level from the LVDTs near the gap between two panels. The minimal deformation at the middle of the connection interface indicates the capacity of the interface was still sufficient.

Grout interfaces between the UHPC and HSC columns were examined after the completion of the 2,200,000 cycles of loads, showing no cracks within the grout pad (see Figure 6-4c and Figure 6-4d). This suggests that a full contact between the columns were valid throughout the entire fatigue test and the upper and bottom portions of the test specimen were moving together under the cyclic loads. Measurements near the gap between the upper and bottom columns illustrated a maximum of 0.0254 mm (0.001 in) for the relative vertical displacement and a maximum of 0.0508 mm (0.002 in) for the relative angular displacement. The uplift displacement at the outface of columns was measured to be at most 0.0762 mm (0.003 in) when the test specimen was loaded to the service load of 444.8 KN (100 kips).

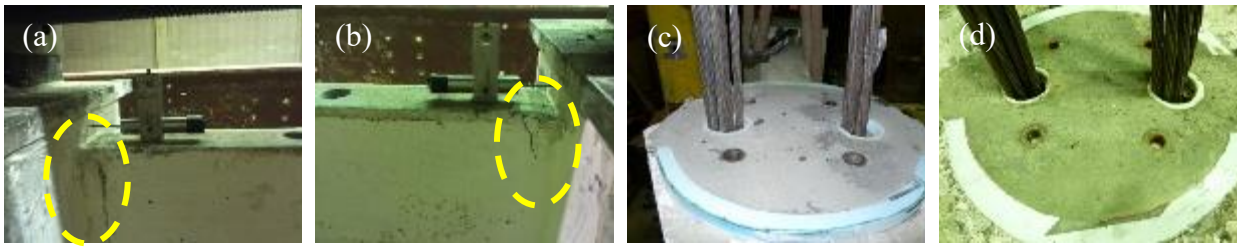

Figure 6-4. Damage observation at the (a) upper left and (b) upper right corner of the interface between UHPC columns and panel, and grout pads (c) between columns and (d) between column and foundation

6.5.2. In-Plane Displacement Responses

In-plane displacements of the test specimen were evaluated during the static testing before the cyclic loading started (S0), after the testing cycles completed 800,000 (labeled as

S0.8), 1 million (labeled as S1), 1.5 million (labeled as S1.5), and 2 million (labeled as S2) cycles. The static load increased every 111.25 KN (25 kips) from 0 to the same maximum load as the service load and return back to 0 to finish one cycle. The corresponding force-displacement relationship was obtained and plotted in Figure 6-5. The maximum positive displacement varied between 2.4613 mm (0.0969 in) and 2.5959 mm (0.1022 in) with a range of 0.127 mm (0.0050 in), which was below the sensitivity of the LVDTs (0.381 mm = 0.0150 in). The observed displacement increased approximately linear with the increase of the applied load, indicating that the test specimen maintained elastically throughout the service load testing and did not show significant permanent displacement. In addition, the out-of-plane displacement was also monitored and the string pot reading showed a maximum displacement of ± 0.127 mm (0.005 in) at the peak loads after the testing finished 2 million cycles of loading.

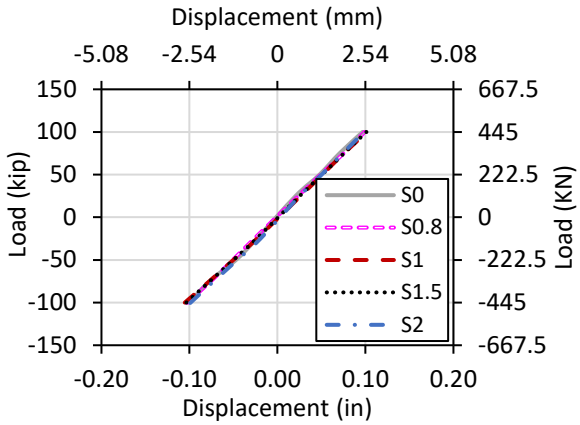

Figure 6-5. Force-Displacement relation of the test specimen obtained from quasi-static tests

To assess the in-plane displacement with the increase in height, displacements at every 914.4 mm (36 in) were obtained at peak load of ± 444.8 KN (100 kips) and compared with respective to the measurement height, as shown in Figure 6-6. The drift ratio, which describes the ratio of maximum displacement to the total height of the chosen test unit, was

measured to be 0.064% at the lower half and 0.074% at the upper half specimen in the negative loading direction but positive displacement values. In the positive loading direction, comparable drift ratios for two stories were 0.065% and 0.072%, respectively. Specifically, displacements along the height of the test specimen under the peak loads of ± 444.8 KN (100 kips) were summarized in Table 6-1. In-plane displacement at peak loads of ± 444.8 KN (100 kips) (1 in = 25.4 mm). It shows that the maximum displacement grew 1.8% in the positive loading direction, i.e., when the specimen was pushed from the actuator, and decreased 1.2% in the negative loading direction at the conclusion of 2 million cycles of fatigue testing. Compared to S1, the smaller displacements obtained from S2 were effected by the strengthening event after S1. Detailed statement of the test events were described in the following discussion.

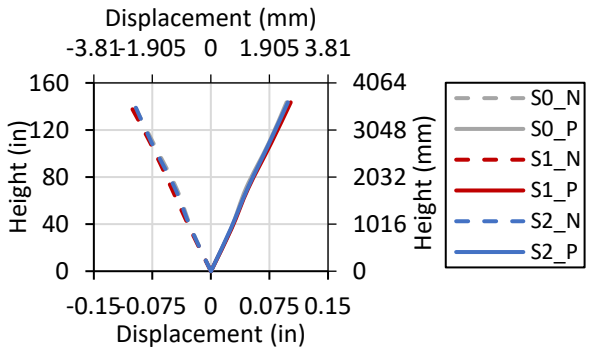

Figure 6-6. In-plane displacement at peak loads obtained from quasi-static tests

Table 6-1. In-plane displacement at peak loads of ± 444.8 KN (100 kips) (1 in = 25.4 mm)

Height (in)	S0 (in)	S1 (in)	Increment over S0	S2 (in)	Increment over S0
36	0.0257	0.0263	2.3%	0.0254	-1.2%
	-0.0250	-0.0268	7.2%	-0.0256	2.4%
72	0.0450	0.0478	6.2%	0.0470	4.4%
	-0.0443	-0.0505	14.0%	-0.0461	4.1%
108	0.0742	0.0772	4.0%	0.0748	0.8%
	-0.0739	-0.0776	5.0%	-0.0759	2.7%

Table 6-1. (continued)

Height (in)	S0 (in)	S1 (in)	Increment over S0	S2 (in)	Increment over S0
144	0.0969	0.1022	5.5%	0.0986	1.8%
	-0.1003	-0.1053	5.0%	-0.0991	-1.2%

After 2 million cycles of service loading, additional 200,000 load cycles at peak loads of ± 556.25 KN (125 kips) continued to apply on the test specimen and the displacement at the top of the test specimen was also obtained at end of the test. In Figure 6-7, force-displacement relationship remained nearly linear at the end of the service load testing (S2) as well as the extreme load testing (S2.2). This linearized relation demonstrated that the test specimen maintain elastically at the conclusion of the fatigue testing. Compared with the S2 curve, the slopes of the load-displacement responses at the end of S2.2 were similar in Figure 6-7, showing the overall stiffness of the test specimen changing from 162875.26 KN/m (929.67 kip/in) to 174207.00 KN/m (994.35 kip/in) at the peak loads. These values were within 3.4% of the average stiffness of 168541.12 KN/m (962.01 kip/in), which is minimal and indicates that the test specimen did not experience any significant damage after subjected to 200,000 cycles at extreme loading condition.

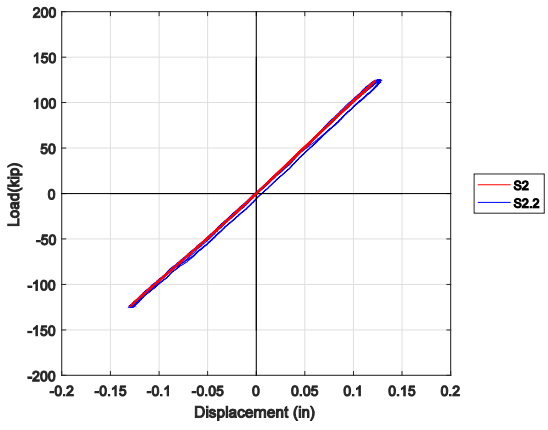

Figure 6-7. Force-displacement responses at the end of service (S2) and extreme (S2.2) loading conditions

After the evaluation of displacement responses from the static tests, peak deflections at top of the test specimen were recorded in both positive and negative directions during the 2.2 million cycles of loading, and the results are plotted as a function of number of cycles in Figure 6-8. To eliminate the impact of the environmental factors on the gauge readings, a small force of ± 22.25 KN (5 kips) was chosen as a reference load in each direction and the resultant peak responses from the test specimen were presented as relative values based on the responses under the small reference load. During the fatigue test, numerous adjustments were applied to the test equipment because of the fatigue damage on the loading frame or steel components. Major events during the entire test were described in Table 6-2. Major test events throughout the test and considered for further discussion on the fatigue responses.

The relative displacements at ± 22.25 KN (95 kips) in Figure 6-8 illustrated a clear increase over the operational load testing. The increase in both the positive and negative directions were at maximum of approximately 7% from 4.4196 mm (0.1740 in) to 4.7244 mm (0.1860 in) towards the end of the service load testing. This means that a similar displacement increment was observed in each loading direction, and the fatigue effects were similar in both directions. Moreover, these variations were comparable to the increase in top deflection at peak load of 5.5% recorded during the service load static test. By considering the small change of the difference between peak deflections measured at the top of the test specimen, the test specimen experiences 7% fatigue degradation over 2 million cycles of operational load. When the test specimen was loaded for additional 200,000 cycles of extreme load, the relative displacement was plotted following the curve at operational load. As shown in Figure 6-8, when the test load was 25% higher and the relative load was 27% higher, the maximum top deflection was recorded at 2.9972 mm (0.1180 in), while a slightly

higher reading of 3.1242 mm (0.1230 in) was shown for minimum top deflection. This change leads to a 27% increase of displacement in the positive loading direction and a 32% increase in the negative loading direction, which were comparable to the load magnitude change.

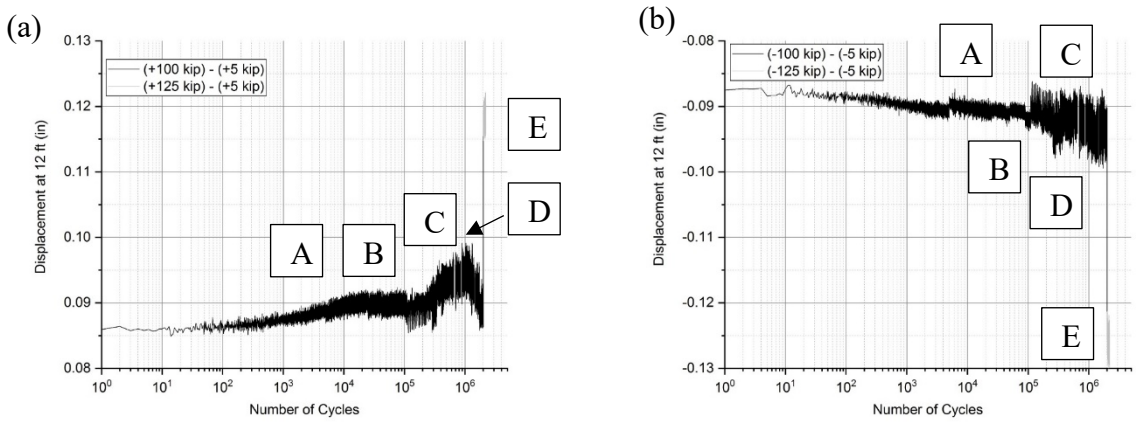

Figure 6-8. Variation of (a) maximum and (b) minimum relative deflection of the test unit over 2,200,000 cycles

Table 6-2. Major test events throughout the test

Label	Major Test Event
A	Strengthening the reacting frame after 5010 cycles
B	Threaded rods at the back of the actuator fatigue failure after 42,124 cycles
C	Top beam at top of the test specimen broken and additional post-tensioning force applied after 117,308 cycles
D	Strengthening bottom anchorage for all four groups of vertical post-tensioning tendons after 1,345,000 cycles
E	111.25 KN (25 kips) higher forces applied after 2,000,000 cycles

6.5.3. In-Plane Strain Responses within Panels

Eighteen total strain gauges were placed on the concrete surface of the two panels. Since the test specimen was setup in plane and the applied force was in the same plane as the test specimen, using the plane strain readings (i.e., ε_x and ε_y) from the strain gauges at

desired locations can calculate the principal strains (i.e., ε_1 and ε_2) and the principal angel θ_p by applying the two strain components in the following equations:

$$\varepsilon_{1,2} = \frac{\varepsilon_x + \varepsilon_y}{2} \pm \sqrt{\left(\frac{\varepsilon_x - \varepsilon_y}{2}\right)^2 + \left(\frac{\bar{\gamma}_{xy}}{2}\right)^2} \quad (6\text{-}1)$$

$$\bar{\gamma}_{xy} = \frac{\Delta}{H} \quad (6\text{-}2)$$

$$\tan 2\theta_p = \frac{\bar{\gamma}_{xy}}{\varepsilon_x - \varepsilon_y} \quad (6\text{-}3)$$

where,

$\bar{\gamma}_{xy}$ is the average shear strain for each concrete panel due to small deformation;

Δ is the story drift due to shear force;

H is the height for each story.

Given the maximum top deflection under the extreme loading was measured to be small compared to the height of the test specimen, the minimal story drift was obtained, giving a negligible shear strain compared to the in-plane strains. Therefore, the principal strains can be presented by the orthogonally placed strains ε_x and ε_y, and their variations with number of cycles are plotted in Figure 6-9 - Figure 6-11. The principal strain under the peak loads at the upper left corner (B1, T1), center (B3, T3), and bottom right corner (B8, T8) of the UHPC (labeled starting at T) and HSC (labeled starting at B) panels were chosen to determine if the stress degradation occurring in the concrete panels during the testing. Similar to the displacement measurements using the strain measured at ± 22.25 KN (5 kips) as a reference, Figure 6-9a shows the maximum tensile and compressive strains in the X-direction at the B1 under the relative loads over the entire 2.2 million cycles of testing. The maximum tensile strain started at 50×10^{-6} in/in and grew to 58×10^{-6} in/in after stiffening the top block after 117,308 load cycles, and remained at 61×10^{-6} until the end of service

load testing, resulting in a total change of 22% in strain. However, the maximum tensile strain at the peak loads reached 79 × 10^{-6} in/in when the test load increased at the extreme level, demonstrating a nearly 30% increase in the negative loading direction. This increased strain contributes to 3.10 MPa (0.45 ksi) tensile stress within the concrete panel, which is still lower than the 5.93 MPa (0.86 ksi) cracking stress of HSC. The maximum compressive strain in Figure 6-9b shows a similar gradual increase of 5 micro-strain in the X-direction. Observations at the conclusion of the test showed no crack in the HSC panel, indicating that no fatigue damage was experienced in the panel.

For the lower corner, the peak strains of B8 in the X-direction was observed to grow by 25% throughout the operational load testing and an additionally increase of 27% after the test load increased by 25% (see Figure 6-9c and Figure 6-9d). The maximum compressive strain in the X-direction at B8 increased from 47.5 × 10^{-6} in/in to 61 × 10^{-6} in/in, while the maximum tensile strain showed an increase from 41 × 10^{-6} in/in to 52 × 10^{-6} in/in in the same direction when the test specimen was loaded 25% increase. This change contributes to a nearly 27% increase in the peak strain, which equals to the relative load increase.

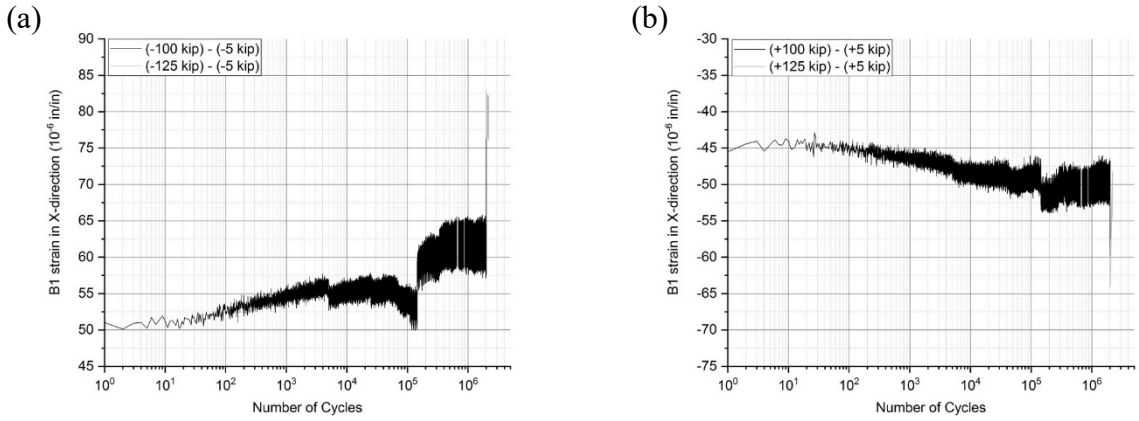

Figure 6-9. The variation of (a, c) the tensile and (b, d) compressive strain in the X-direction at the upper left corner (B1) and the bottom right corner (B8)of the HSC panel during the fatigue test

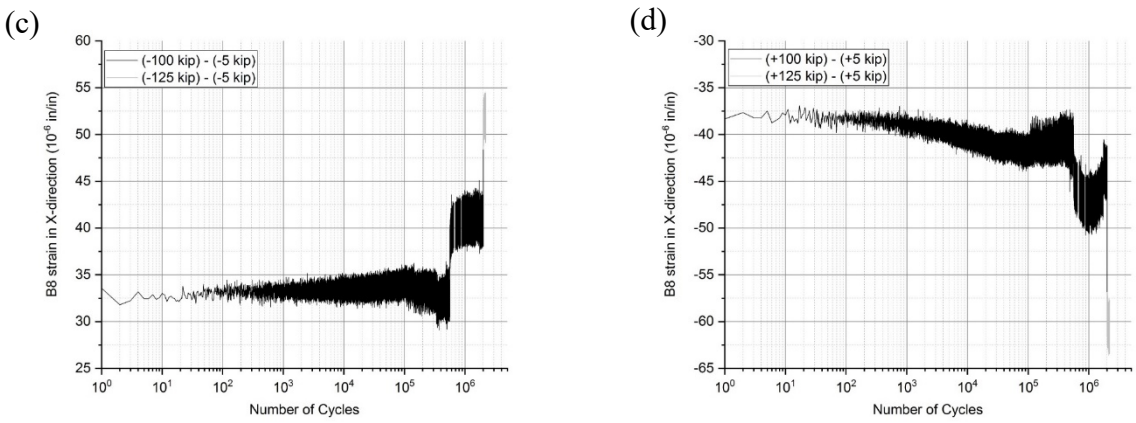

Figure 6-9. (continued)

Similarly, the principal strain of B0 and B3 was examined under tension and compression in the HSC panel and the results are presented in Figure 6-10. Since these two strain gauges were placed at the center of the concrete panel on the front (B3) and back sides (B0), respectively, the strain comparison between these two locations can be used as an indicator for the in-plane testing. In the X-direction, strains between these two locations showed a maximum of 4×10^{-6} in/in difference at the end of test, and the change of the compressive strain under peak loads at both locations was similarly at 3×10^{-6} in/in when the test load applied from ± 446 KN (100 kips) to ± 556.03 KN (125 kips), suggesting that the test specimen has been experienced in-plane loading condition. When examining the strain change in the Y-direction for these two locations, the peak strain maintained at zero for the entire test, reaffirming that the center of the concrete panel experienced stresses only in the X-direction.

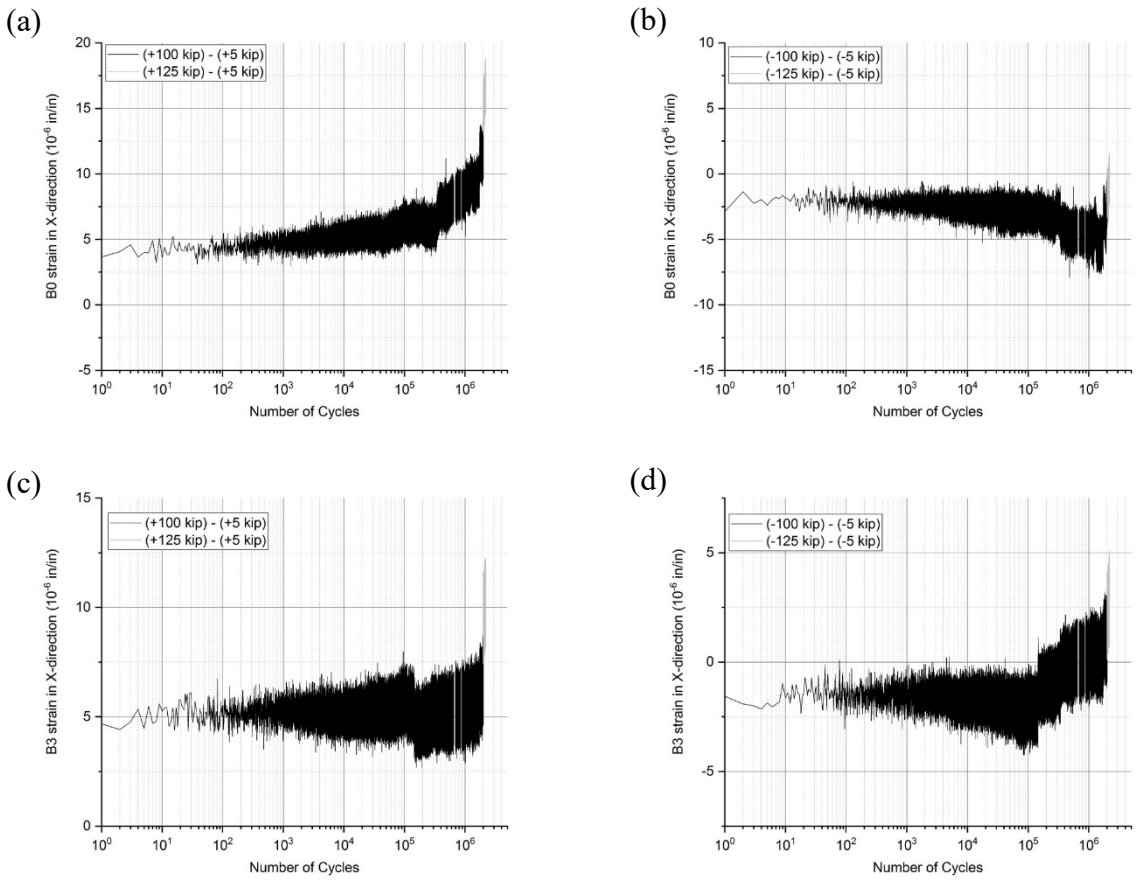

Figure 6-10. The compressive (a, c) and tensile (b, d) strains in the X-direction under peak loads at the front (c, d) and back (a, b) side of the center HSC panel during the fatigue test

For the upper half of the test specimen, concrete strains were also monitored in both X and Y direction and the maximum compressive and tensile strains under the relative peak loads were shown in Figure 6-11. In this figure, strains measured at the upper corner (T1) of the UHPC panel illustrated a clearly increase throughout the fatigue test with an apparent change at the end of 117,308 cycles, which was due to additional post-tensioning stresses applied in the top block and the resultant compressive stresses influenced on the panel stress. The measurements at T1 was affected sensitively by the re-strengthening event, as they were collected at the same height as the uppermost post-tensioning tendon in the UHPC panel. Maximum tensile strains in the negative loading direction at T1 increased nearly 40×10^{-6}

in/in starting from 80 × 10^{-6} in/in, which was below 161 × 10^{-6} in/in, the corresponding strain of the UHPC fracture stress. The tensile strains at T8 were even lower than the measurements at T1, suggesting that there was no fatigue damage during this period. Maximum compressive strain was measured to be minimal compared to the compressive strength of UHPC. After the change at end of 117,308 cycles, the recorded peak strain at T1 and T8 remained nearly constant with some fluctuations. When the external loads increased at the end of 2 million cycles, the peak strains in the X-direction at T1 and T8 were increased by 30% and 33%.

Two strain gauges were also placed at the front (T3) and back (T0) sides on the center of the UHPC panel, respectively to examine if the upper half of the test specimen performed in-plane deformation. Similar to the HSC panel, two gauges did not show significant difference in the peak strains throughout the test, resulting an average of 9 × 10^{-6} in/in at the end of operational loads testing and 13 × 10^{-6} in/in at the conclusion of the entire test. These small deformations indicated that stresses became smaller if closer to the center of the concrete panel.

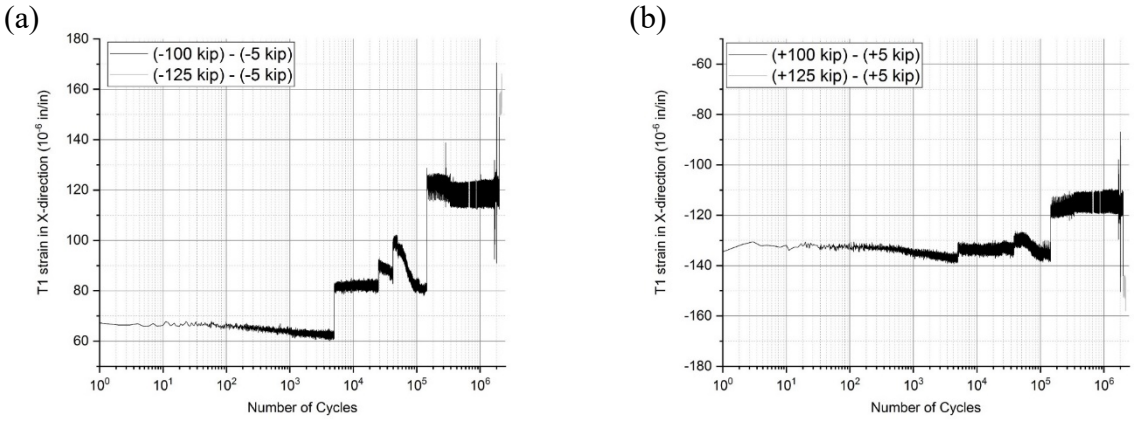

Figure 6-11. The variation of the (a, c) tensile and (b, d) compressive strain in the X-direction at the upper left corner (a, b) and the bottom right corner (c, d) of the UHPC panel during the fatigue test

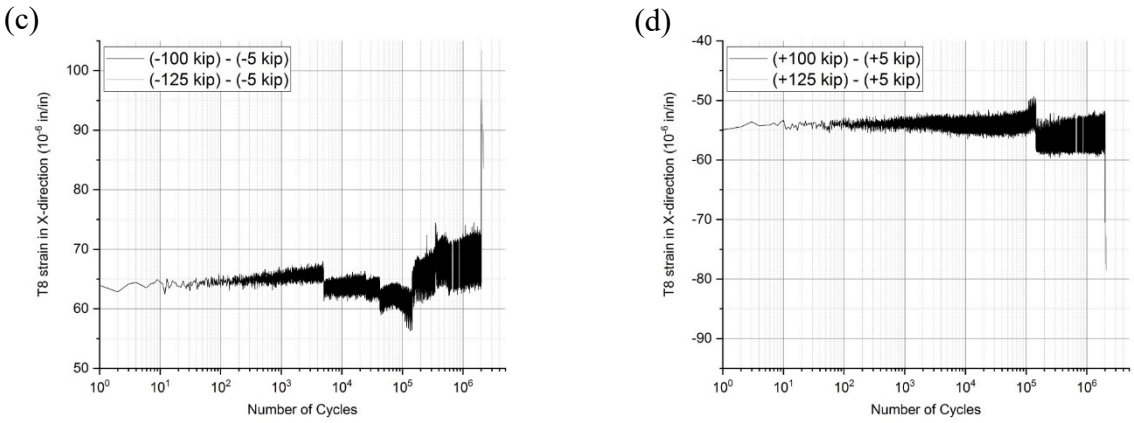

Figure 6-11. (continued)

6.6. Conclusions

A full-scale precast column-panel-column test specimen representing one section of Hexcrete Tower was developed, followed by a successful fatigue laboratory test of the full-scale test specimen consisting of two UHPC columns, two HPC columns, with one UHPC and HPC panel connected with prestressing strands. A subsequent numerical analysis confirmed the desirable performance of the UHPC and HPC panels, as well as the specialized connections. With respect to the objectives of this project, the following conclusions can be drawn.

- Force-displacement relation remained linear until the end of the experiment, confirming elastic response of the test specimen.
- Though some hairline cracks were seen on the back surface of the UHPC panel, they did not experience any further growth during the fatigue testing.
- Small interface cracking occured at the top corners of the UHPC panel due to the test setup used, however, the crack width was negligibly small and it did not widen during testing.

- Experimental qualified principal compressive and principal tensile stresses in the panels confirmed that the fatigue damage on these critical members would be minimal.
- The interface between the column and panel can open up when the load exceeds beyond the extreme loading case used for the project, which should be further investigated and the tower connection could be appropriately redesigned.

6.7. Acknowledgements

The financial support from the U.S. Department of Energy under Award No. DE-EE0006737 and Iowa Energy Centers are greatly appreciated. The authors would like to thank Lafarge North America for providing the UHPC material for the test specimen. Thanks are also extended to Todd Culp and E. J. Bjorling of Coreslab Structures (Omaha) for organizing the fabrication of all the tower components in a timely manner.

6.8. References

Aaleti, S., Honarvar, E., Sritharan, S., Rouse, M., and Wipf, T. J. (2014). Structural Characterization of UHPC Waffle Bridge Deck and Connections. *InTrans Project Reports*. Paper 73.

Aaleti, S., Sritharan, S., Bierwagen D., and Terry J.W. (2011). Experimental Evaluation of Structural Behavior of Precast UHPC Waffle Bridge Deck Panels and Connections. *Transportation Research Board 90th Annual Meeting Compendium of Papers*. Vol. 2251. Washington, D.C.

Herwig, A. (2008). Reinforced Concrete Bridges under Increased Railway Traffic Loads – Fatigue Behavior and Safety Measures. Ph.D. Thesis. École Polytechnique Fédérale De Lausanne. Lausanne, Switzerland.

Keierleber, B., Bierwagen, D., Wipf, T., and Abu-Hawash, A. (2008). Design of Buchanan County, Iowa Bridge using UHPC and Pi-Girder Cross Section. *Proc., Precast/Prestressed Concrete Inst. National Bridge Conf.*, Orlando, FL, Paper 27.

Lappa, E. S. (2007). High Strength Fiber Reinforced Concrete Static and Fatigue Behavior In Bending, Doctoral thesis, Delft University of Technology, Netherlands.

Makita, T. and Brühwiler, E. (2012). Fatigue Behavior Of Bridge Deck Slab Elements Strengthened with Reinforced UHPFRC. *Proceeding of 6th International Conference on Bridge Maintenance, Safety, Management, Resilience and Sustainability.* Italy.

Makita, T. and Brühwiler, E. (2014). Tensile Fatiuge Behavior of Ultra-High Performance Fibre Reinforced Concrete (UHPFRC). *Material Structure,* 47: 475. doi: 10.1617/s11527-013-0073-x

Paschalis, S. A. and Lampropoulos, A. P. (2016). Ultra-High-Performance Fiber-Reinforced Concrete under Cyclic Loading. *ACI Material Journal*. Vol. 13, No. 4, 419-437.

Sima, J. F., Roca, P., and Molins, C. (2008). Cyclic Constitute Model for Concrete. *Engineering Structures*. 30 (3): 695-706.

Sritharan S. (2015). Hexcrete Tower for Harvesting Wind Energy at Taller Hub Heights - Budget Period 2. Ames, Iowa. doi:10.2172/1361022

Switek, A. E., (2011) Time-Dependent Response of Ultra High Performance Fibre Reinforced Concrete (UHPFRC) under Low to High Tensile Stresses, Doctoral thesis No. 4899, École Polytechnique Fédérale de Lausanne (EPFL), Switzerland. doi:10.5075/epfl-thesis-4899

Waagaard, K. and Veritas, D. N. (1977). Fatigue of Offshore Concrete Structures – Design and Experimental Investigations. *Proceedings of the 9th Annual Offshore Technology Conference,* Houston, Texas.

Yankelevsky, D. Z. and Reinhardt, H. W. (1987). Model for Cyclic Compressive Behavior of Concrete. *Journal of Structural Engineering, ASCE*. Vol. 113, No. 2, 228-240.

Yankelevsky, D. Z. and Reinhardt, H. W. (1989). Uniaxial Behavior of Concrete in Cyclic Tension. *Journal of Structural Engineering, ASCE*. Vol. 115, No. 1, 166-182.

CHAPTER 7. CONCLUSION

7.1. Wind Energy Potential at Greater Heights

Hexcrete Tower system provides an innovative technology to build tall wind towers at reduced cost compared to the conventional tubular steel tower. Estimation of wind energy production for tall towers assesses the potential increase of annual energy production obtained from using wind towers taller than 80 m in both wind-rich and low wind-speed regions, which helps validate the possibilities of LCOE benefits from building tall wind towers. Based on the analysis of this study, it was found that

(a) in order to realistically estimate the wind energy production at hub heights, actual variations of wind speed, wind direction at the wind-turbine operating heights were obtained to determine the wind characteristics and power-law exponent. Results showed that wind speed at different heights varies consistently with hour and season, and the resultant power-law exponent changes as a function of time. This indicates that using a 1/7 constant power-law exponent is insufficient to predicte the wind energy production.

(b) by applying the actual wind measurements to the AEP calculation model, the estimated energy production showed a good agreement with the measured power data and historical record in terms of the hourly and seasonal variations and the annual averages. This validated model was then used to evaluate the wind energy potential at higher hub heights for different areas in the United States.

(c) by increasing the hub height from 80 m to 100 m, wind turbines with the same capacity can provide up to 14% additional energy production in the wind-rich regions. This indicated that with stronger wind resources and enhanced energy production, tall towers

provide opportunities to lower the LCOE and the optimal height of wind towers needs to be justified in this region.

(d) in the low wind-speed regions, wind energy production harvested from 120-m tall towers was estimated to be at least 30% higher than that from towers at 80 m. Considering the power price in these areas' market, the higher AEP achievement was expected to contribute 30% - 50% increase of financial gain to the wind farm developers for building 120-m towers in these areas.

(e) simulated wind data obtained from the NREL data repository exhibited slightly lower wind speeds than the actual measurements in the observed wind-rich regions leading to a conservative estimate of AEP, while in the low wind-speed areas, simulated datasets predicted relatively higher energy productions than the observations. This suggested that using actual wind measurements at elevated heights is essential for estimating AEP potentials.

7.2. Fatigue Performance of Hexcrete Tower Connections and Components

A column-panel-column unit was tested to validate the Hexcrete tower design for the fatigue behavior and showed that the tower connections and the system had sufficient capacity under operational and extreme loads for large numbers of cycles. This study can be concluded that

(a) linear force-displacement behavior was observed under the service load condition and remained until the end of the fatigue test, showing that the test unit performed in the elastic stage.

(b) localized hairline cracks were observed in the uppermost corner regions of the UHPC panel but did not develop wider to cause damage on the tower component, and thus had little effects on the total response.

(c) low averaged stresses in compression and tension observed in the panels did not affect the overall performance of the test unit when it is subjected to the fatigue load.